Magneto–electric properties of magnetic field sensors fabricated using AlGaN/GaN heterostructures for harsh environments

June, 2014

DOCTOR OF ENGINEERING

Abdelkader Abderrahmane

TOYOHASHI UNIVERSITY OF TECHNOLIOGY

ABSTRACT

Hall effect sensors are ubiquitous, being used in the electronics industry for monitoring rotation in optical memory disks, banknote authentication in vending machines, and for sensing currents in cables. Other notable applications of micro Hall sensors include scanning Hall probe microscopy (SHPM) and medical diagnostics based on the detection of magnetic tags attached to target molecules. Now, while Hall sensors are widely used at cryogenic and ambient temperatures, there are still niche demands for Hall sensors that are stable at elevated temperatures of about 400°C for applications such as the determination of the Curie temperatures of ferromagnetic materials. More recent demands include the sensing of currents in electric cars, where the ambient is well above room temperature. Hall sensors are also promising for space applications such as in electronics systems for space exploration vehicles, where size and power consumption are important, and monitoring magnetic fields in charged particle accelerators. Recently there have been reports on indium antimonide (InSb) based Hall sensor devices as candidates to replace magnetic sensors used in thermonuclear power stations. In such extreme environments Hall sensors must withstand high temperatures and particles and/or electromagnetic irradiation.

Conventional Hall sensors fabricated using silicon (Si), indium arsenide (InAs) or indium antimonide are stable up to temperatures of about 125°C, and above this temperature, the sensors are inoperable due to the onset of intrinsic conduction and physical degradation of the semiconducting materials. Silicon carbide (SiC) could potentially be used for fabricating Hall sensors operating at high temperature because of its large band gap, high electron saturation velocity, and excellent thermal stability at high temperatures. However, the need for precise control of dopants and the large

thickness of the conducting layers of SiC severely limits its sensitivity and stability at high temperatures. The gallium nitride (GaN) and its related compound aluminum gallium nitride (AlGaN) have wide band gap, high thermal and chemical stabilities. The gallium nitride has low intrinsic electron concentration, which is several orders of magnitude lower with respect to that of Si or gallium arsenide (GaAs), and comparable with that of SiC, enabling the increase of the maximum operation temperature. Moreover, gallium nitride has high threshold displacement energy making this material tolerant against particles irradiation; therefore, Hall sensors based on the GaN are suitable for magnetic field sensing for high temperature and high-energy particles irradiation application fields.

In addition, formation of the two–dimensional electron gas at the interface between the AlGaN and GaN gives rise to high electron density in a thin active region of thickness of few nanometers and to high electron mobility, making the AlGaN/GaN heterostructures appropriate for Hall sensor devices. The fabrication and the characterization at high temperature and high proton irradiation of Hall sensors based on the AlGaN/GaN heterostructures were described and compared with the conventional Hall sensors based on AlGaAs/GaAs and AlInSb/InAsSb/AlInSb heterostructures. Electrical characterizations of the micro–Hall sensors based on AlGaN/GaN heterostructures at high temperature and high–energy proton irradiation showed that micro–Hall sensors based on AlGaN/GaN heterostructures are stable from cryogenic temperature to a temperature of 400°C and expected to show stability up to about 700°C, and are tolerant to high–energy proton irradiation up to proton dose of 10^{14} protons/cm^2. Proton irradiation on the AlGaN/GaN heterostructures based micro-Hall sensors induce defects and crystal quality damage, however, the possibility of recovering of the crystal

quality and defect removing by annealing was confirmed by electrical and optical characterizations.

The micro-Hall sensors reported in this study were not protected by any form of packaging. The maximum proton fluence at which the AlGaN/GaN heterostructures based micro-Hall sensors are stable at is equivalent to thousands of years of the sensor application lifetime at the low-earth orbit (LEO). However, the protection of the micro–Hall sensors by a ferromagnetic materials can in the same time enhances the sensor sensitivity and detectivity and reduces or stops the effect of proton irradiation, therefore, increases the micro–Hall sensors lifetime in harsh environments.

The AlGaN/GaN heterostructures and the AlInSb/InAsSb/AlInSb quantum wells based micro–Hall sensors are good candidates to replace the magnetic sensors used in the outer space application in term of size, power consumption, and proton irradiation hardness.

I would like to express my highest and heartfelt gratitude to God for his guidance and blessings during all the times,

I would dedicate this work to:

My father,

My sisters,

My wife Malak, and to my unborn child,

To my mother and brother, God bless them.

ACKNOWLEDGEMENTS

I would like to express my sincere appreciation to Professor Adarsh Sandhu, my thesis advisor, for his willingness to take me in his research group and his valuable support. He introduced me to very interesting research field, and thanks to him, I could discover my passion for magnetic devices. I was extremely fortunate to have him as a mentor and to be able to learn from him not only about the physics but also about many other things, that I know now, are necessary to make a successful carrier as a physicist.

I would like to thank Professor Hiroshi Okada for his closely observing my work and his advising and support during my PhD course.

I am very thankful to the Japanese International Cooperation Agency (JICA) for financing my research and study, and their continued supports during the four years.

I would to thank Professor Tsukasa Takamura, Dr. Pil Ju Ko, Mr. Shota Koide and all Sandhu Lab members for their supports and helps.

SUMMARY

Specifically outlining the work achieved in this PhD thesis, the work is organized into separated chapters.

Chapter 1, we report on a background, purpose of this research, and flow chart of the thesis.

Chapter 2 is an introduction on the different magnetic sensors, and description on the characteristics of the Hall effect sensors.

In Chapter 3, we describe the advantages of the gallium nitride and the formation of the two-dimensional electron gas in the AlGaN/GaN heterostructures. The quantum Hall effect, which is the evidence of the two-dimensional electron gas existence, is described.

In Chapter 4, we introduce the two mains harsh environments: space and nuclear environments. Protons are the dominant particles in the outer space and neutrons in the nuclear environment. We discuss in brief the interaction between the particles and the materials and the fundamental radiation damage mechanisms in semiconductors. Finally, we show harsh environment application fields of the magnetic sensors in general and the Hall sensor in special. We showed the disadvantage of the currently used magnetic sensors and the advantage of replacing these sensors by Hall effect sensors.

In Chapter 5, we studied the AlGaAs/GaAs heterostructures, AlInSb/InAsSb/AlInSb quantum wells and AlGaN/GaN heterostructures based micro–Hall sensors at high temperature. The use of the AlGaAs/GaAs at high temperature magnetic field sensing is limited at a temperature of 250°C; in the other hand, the InAsSb quantum wells are poor when the temperature exceeds 150°C. However, the micro–Hall sensors based AlGaN/GaN are stable in term of magnetic sensitivity from cryogenic up to a

temperature of 400°C and expected to work up to temperature of 700°C. We fabricated a new generation of Hall sensors based on two–dimensional materials such as MoS_2 and $MoSe_2$. We studied the effect of the high–energy and high–flux proton irradiation on the physical properties of the AlGaN/GaN and the AlInSb/InAsSb/AlInSb heterostructures based micro–Hall sensors. AlGaN/GaN heterostructures based micro–Hall sensors show stable magnetic sensitivity up to proton fluence of 10^{14} protons/cm^2 but degradation in the electrical properties. The magnetic sensitivity in the AlInSb/InAsSb/AlInSb heterostructures based micro–Hall sensors irradiated by proton fluence of 10^{14} protons/cm^2 decreases; however, due to their high carrier mobility the AlInSb/InAsSb/AlInSb heterostructures based micro–Hall sensors were operational up to proton fluence of 10^{16} proton/cm^2.

In Chapter 6, the effect of annealing on the AlGaN/GaN heterostructures based micro–Hall sensors was studied. Recovery of the electron mobility and a decrease in the sheet resistance of the annealed micro–Hall sensors, as well as an enhancement in their magnetic sensitivity were reported. Trap removal and an improvement in the crystal quality by removing defects were confirmed through current–voltage measurements and Raman spectroscopy, respectively. Cathodoluminescence measurements were carried out at room temperature before and after annealing and showed improvement in the band edge band emission of the GaN layer. After annealing the AlGaN/GaN heterostructures based micro–Hall sensors irradiated by proton fluence of 10^{15} protons/cm^2 became operational with improvements in its magnetic sensitivity.

Chapter 7 outlines the main discussion and conclusions of the thesis work and future prospect.

Chapter 1

General introduction

1-1 Background

Wide bandgap of GaN shows potential for stable operation at high temperatures [1-3]. Furthermore, GaN and related materials are expected to have a high tolerance for high-energy particle irradiation because of their chemical stability. On the other hand, Weaver et al. reported InAs/AlSb high-electron mobility transistor (HEMT) to be highly radiation-tolerant compared with other GaAs/AlGaAs HEMT and related material systems [4]. Thus, GaN- and InAsSb-related heterostructures are candidate for Hall sensors in harsh environment. To our knowledge, however, no report exists addressing the systematic comparison of operation of AlGaN/GaN and AlInSb/InAsSb/AlAsSb Hall sensors at high temperatures and in harsh radiation environment.

1-2 Objective of this research

In the aim to find the operation limits of Hall sensors in harsh environment, we studied the effect of high temperature, high–energy and high–flux proton irradiation on Hall sensors based on gallium nitride (GaN), and indium antimonide (InSb) heterostructures. Two heterostructures were reported in this study AlGaN/GaN and AlInSb/InAsSb/AlInSb heterostructures. The AlGaN/GaN heterostructure micro–Hall sensors were fabricated by metal organic chemical vapor deposition, and the sheet carrier density and electron mobility at room temperature were 7.36×10^{12}cm^{-2} and 1775 cm^2/Vs, respectively. The AlInSb/InAsSb/AlInSb heterostructures were grown by molecular beam epitaxy on semi–insulating GaAs (100) substrate, the sheet carrier density and electron mobility at room temperature were 3.03×10^{12}cm^{-2} and 39100 cm^2/Vs, respectively.

This research includes experiments on the effect of high–temperatures and high–energy radiation on the physical properties of these materials as well as the magneto–resistive characteristics of micro–Hall sensors fabricated using these materials. Knowledge of the effects of temperature and radiation on these materials is important for applications such as satellites and nuclear power stations where radiation exists and may adversely affect device operation.

1-3 Outline of doctoral thesis

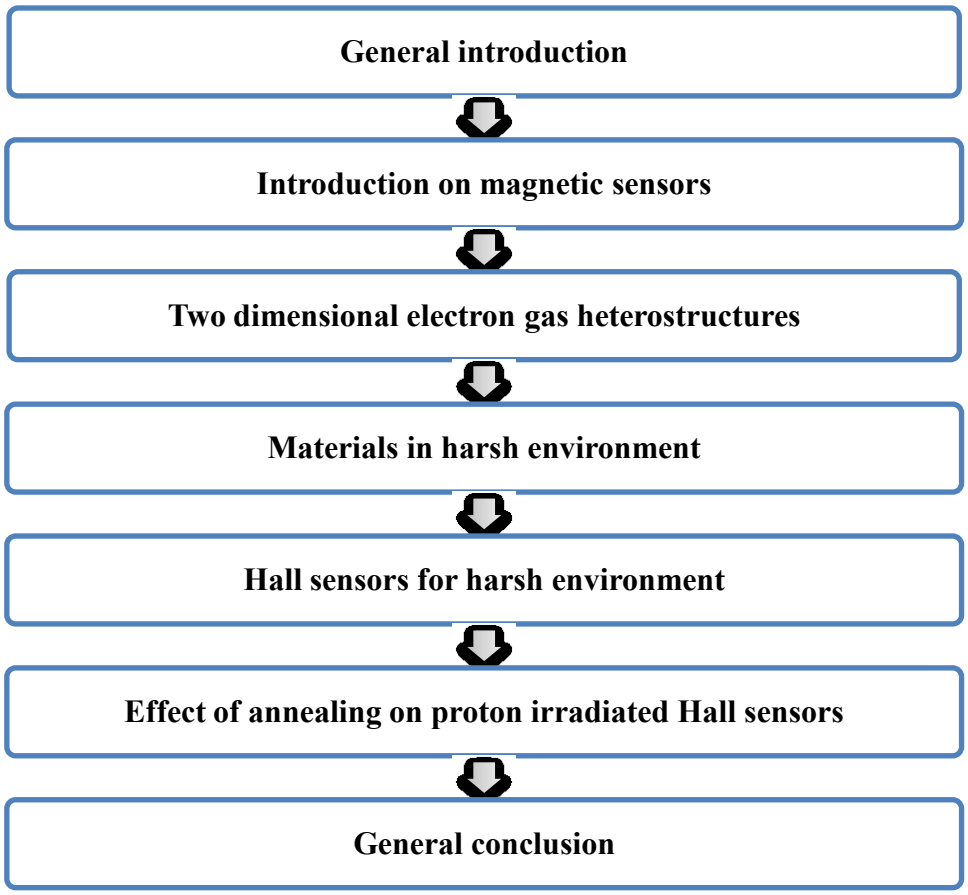

Figure 1 Doctoral thesis flow chart.

1-4 References

[1] H. Lu, P. Sandvik, A. Vertiatchikh, J. Tucker, and A. Elasser; "*High temperature Hall effect sensors based on AlGaN/GaN heterojunctions*"; J. Appl. Phys. **99**, 114510 (2006).

[2] Z. Primadani, H. Osawa, and A. Sandhu; "*High temperature scanning Hall probe microscopy using AlGaN/GaN two dimensional electron gas micro-Hall probes*"; J. Appl. Phys. **101**, 09K105 (2007).

[3] R. Akram, M. Dede, and A. Oral; "*Imaging capability of pseudomorphic high electron mobility transistors, AlGaN/GaN, and Si micro-Hall probes for scanning Hall probe microscopy between 25 and 125 C*"; J. Vac. Sci. Technol. B, **27**, 1006 (2009).

[4] B. D. Weaver, J. B. Boos, N. A. Papanicolaou, B. R. Bennett, D. Park, and R. Bass, "High radiation tolerance of InAs/AlSb high-electronmobility transistors," Appl. Phys. Lett. **87**, 173501 (2005).

Chapter 2

Introduction to magnetic sensors

In this Chapter, we introduce the different magnetic sensors used in industry and their field of application. Next, we focus on the characteristics of the Hall effect sensors, which is the main component of this research, we describe the theoretical parameters which determine their reliability in the standard condition.

2-1 Magnetic sensors

Nowadays, the magnetic sensors occupy a major place in our surroundings. They have lot of applications such as a part of the consumer electronics (magnetic storage, electronic compasses, etc…), in electronic navigation systems (aeronautics, space navigation [1], etc…), in measurement systems and industrial control (position and current detections and measurements, etc…). One of the important applications of the magnetic sensors in the past was detecting the underwater mines during the 2nd world war. New applications, such as handheld electronic compasses and magnetic ink readers, are now possible thanks to the miniaturized sensors.

In fact, integrated technologies not only allow the manufacturing of the sensors with reduced dimensions, but also the integration, on the same ship, the sensor and its measurement interface. This permits significant cost reduction of large–scale production.

Numerous physical principles allow the magnetic field measurement. The main types of sensors and their measuring ranges are shown in Figure 2.1.

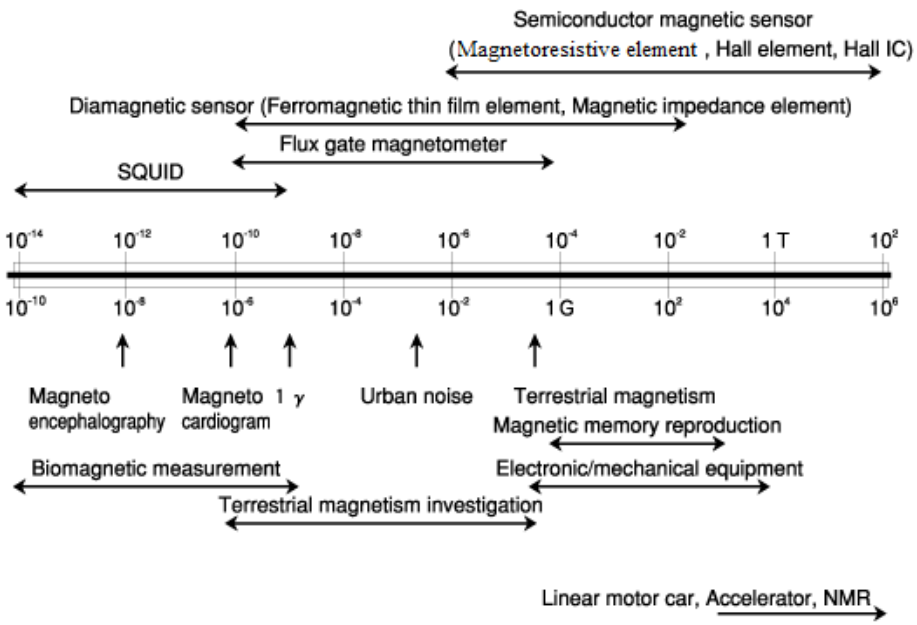

Figure 2.1 Operating ranges and application fields of magnetic sensors.

2-1-1 Superconducting Quantum Interference Device (SQUID)

The SQUID has been developed around 1962, it is the most sensitive low magnetic field sensor with 15 orders of magnetic sensitivity magnitude (from femto–tesla to 9 tesla) [2]. SQUID is used in medical applications such as detecting the human brain neuro-magnetic field. The main disadvantage of such a sensor is the cryogenic temperature of operation.

2-1-2 Search-coil

Search-coil is an induction sensor based on the induction Faraday law. The variation of the magnetic field flux through the coil induces voltage given by $V = -N\, d\Phi/dt$ where N is the turn numbers of the coil. The sensitivity of the search–coil depends on the material used, the area, and the turn numbers of the coil. The main disadvantage of such a sensor is its limitation for static or low frequency magnetic flux.

2-1-3 Magneto–inductive sensor

The magneto–inductive sensor is a solenoid with magnetic material inside. When the current flows inside the solenoid, it generates a magnetic field and induces a voltage. The value of the inductance of the sensor deduced from the voltage induced and the initial current. An external magnetic field H_{ext} changes the value of the induced voltage by the sensed magnetic field; therefore, it changes the magneto-inductance. Thereafter, the value of the external magnetic field deduced from the variation of the magneto–inductance.

2-1-3 Magnetoresistor sensor

The magnetoresistor sensor is based on the variation of the resistance under applying an external magnetic field due to Lorentz force. As a result, the Lorentz force deflects the path of the moving free charge carrier as shown in Figure 2.2.

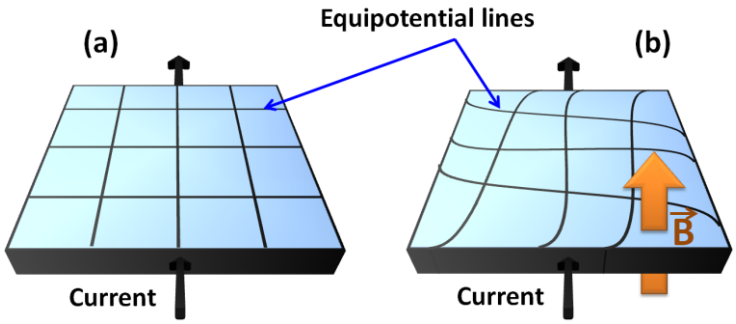

Figure 2.2 Origin of the magnetoresistive effect in semiconductors. (a) equipotential lines in absence of external magnetic field; (b) the same lines after applying a magnetic field [3].

The increase in the path length as shown in Figure 2.2(b) causes a change in the material resistivity. The resistance is given in function of the magnetic field (B) by the equation $R(B) = R_0(\rho_B/\rho_0)(1 + \mu^2 C B^2)$ where R_0 is the resistance of the material in the absence of the magnetic field, ρ_B/ρ_0 is the magnetoresistivity coefficient, μ is the carrier mobility and C is geometrical coefficient given by $C = 1 - 0.54(l/w)$, l is the sample length and

w is the sample width. Semiconductors with high mobility like InSb and InAs are most frequently used as magnetoresistor sensors.

2-1-4 Hall effect sensor

a- The Hall effect

The motion of electrons in a Hall effect sensor, when a magnetic field ($\boldsymbol{B}$) and an electric field ($\boldsymbol{E}$) are applied, is described by the Lorentz equation:

$$m^* \frac{d^2\boldsymbol{r}}{dt^2} + \frac{m^*}{\tau}\frac{d\boldsymbol{r}}{dt} = -e[\boldsymbol{E} - (\boldsymbol{v} \times \boldsymbol{B})] \tag{2.1}$$

where e is the elementray electron charge, m^* is its effective mass and τ^{-1} is its relaxation (scattering) rate. Under steady-state conditions, $d^2\boldsymbol{r}/dt^2 = 0$, equation (2.1) can be written as:

$$\frac{m^*}{\tau}\boldsymbol{v_d} = -e[\boldsymbol{E} - (\boldsymbol{v_d} \times \boldsymbol{B})] \tag{2.2}$$

Where $\boldsymbol{v_d}$ is the electron drift velocity. By multiplying both sides of the equation (2.2) by the electron density N and the electron charge e. Each component of the current density $\boldsymbol{j} = -eN\boldsymbol{v_d}$ can be expressed as follows:

$$j_x = \sigma_0 E_x - \omega_c \tau j_y, \;\; j_y = \sigma_0 E_y + \omega_c \tau j_x, \;\; j_z = \sigma_0 E_z \tag{2.3}$$

Where $\sigma_0 = Ne^2\tau/m^*$ and $\omega_c = eB_z/m^*$ called the cyclotron frequency of the electron in the presence of the magnetic field (B_z). The magnetoconductivity tensor $\boldsymbol{\sigma}(B)$ for the electrons is deduced from equation (2.3) as:

$$\boldsymbol{\sigma} = \frac{\sigma_0}{1+(\omega_c\tau)^2}\begin{pmatrix} 1 & -\omega_c\tau & 0 \\ \omega_c\tau & 1 & 0 \\ 0 & 0 & 1+(\omega_c\tau)^2 \end{pmatrix} \tag{2.4}$$

From equation (2.4) we conclude that the effects of the magnetic field on the charge transport are twofold. First, the conductivity perpendicular to the magnetic field decreased by factor $[1 + (\omega_c\tau)^2]^{-1}$. Second, the magnetic field generates a current transverse to the applied

electric field, resulting in off–diagonal elements in the conductivity tensor. The off–diagonal elements give rise to the Hall effect.

Considering the sample shown in Figure 2.3, where the electric field is applied along the x–axis and the magnetic field along z–axis, electrons drift along the x–axis under the influence of the electric field and experience a force in the y direction according to Lorentz's law. Therefore, a voltage rises in the y direction (V_y) called also as Hall voltage (V_H). This phenomenon is known as the Hall effect discovered by E. H. Hall in 1879 [4].

The charges drift and pile up on the two opposite sample surfaces perpendicular to the y axis, due to the applied magnetic field, creating an electric field $E_y$opposite to the Lorentz force. Under the steady–state condition $j_y = 0$, the induced electric field E_y is deduced from the equations (2.3) as:

$$E_y = -\frac{\omega_c \tau}{\sigma_0} j_x \tag{2.5}$$

The current measured in the x-direction is given by:

$$j_x = \sigma_0 E_x \tag{2.6}$$

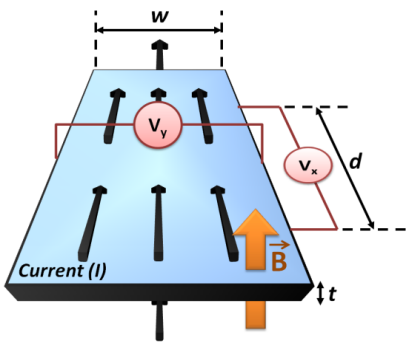

Figure 2.3 Geometry of a Hall effect measurement on a sample of thickness *t* and width *w*.

The electric field in the y-direction is externally controlled by j_x and $\boldsymbol{B}$. Therefore, one defines the Hall coefficient R_H as the ration:

$$R_H = E_y / j_x B_z \tag{2.7}$$

Using equations (2.5) and (2.6) combined with the equation (2.7), we deduce the Hall coefficient as:

$$R_H = -\frac{\omega_c \tau}{\sigma_0 B_z} = -\frac{1}{Ne} \tag{2.8}$$

Where N is the carrier charge density. The sign of R_H depends of the sign of the charge, it is negative when the type of carrier which contribute to the conduction are electrons. In compensated semiconductor samples, where both electrons and holes are present, the two-carrier model [5] gives the Hall coefficient.

b- The Van der Pauw technique

The Van der Pauw technique is used to measure the resistivity or the sheet resistance, this technique was developed by L. J. Van der Pauw in 1958 [6]. The most common wafer–level technique to measure the resistivity ρ is the four-point probe technique illustrated in Figure 2.4(a). For thin-film samples of finite size, ρ is given by

$$\rho = 2\pi s \left(\frac{V_{32}}{I_{14}}\right) CF \tag{2.8}$$

Where CF is a correction factor that takes into account sample size, thickness and shape as well as the orientation of the probes with respect to the sample borders. s is the distance between each two successive probes.

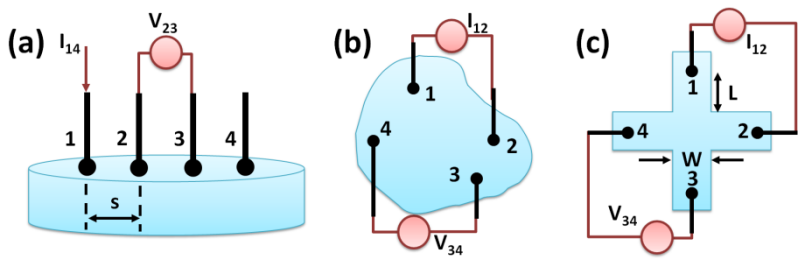

Figure 2.4 The Van der Pauw technique used to measure the resistivity.

For an arbitrary shape sample shown in Figure 2.4(b), van der Pauw developed a method

based on conformal mapping to extract the resistivity of thin films. The resistivity is obtained by solving the equation:

$$exp\left(-\frac{\pi t R_{12,34}}{\rho}\right) + exp\left(-\frac{\pi t R_{23,41}}{\rho}\right) = 1 \tag{2.9}$$

where t denotes the sample thickness. The resistances $R_{12,34}$ and $R_{23,41}$ in equation (2.9) are given by $R_{12,34} = V_{34}/I_{12}$ and $R_{23,41} = V_{41}/I_{23}$. Equation (2.9) can be solved numerically but in symmetrically shaped structures such as the Greek-cross device, shown in Figure 2.4(c), the resistivity ρ is obtained from:

$$\rho = \frac{\pi t R_{12,34}}{\ln(2)} \tag{2.10}$$

By combining the two directions of current I_{12} it is possible to cancel the voltmeter offsets and parasitic thermoelectric voltages. The resistivity is given by:

$$\rho = \frac{\pi t}{\ln(2)} \frac{V_{34,(I_{12})} - V_{34,(-I_{12})}}{2I_{12}} \tag{2.11}$$

The sheet resistance is defined by $R_{sh} = \rho/t$. To obtain a more precise value of the sheet resistance, we use eight measurements of voltage yield the following eight values of resistance:

$$\begin{cases} R_{21,34} = V_{34} / I_{21} \quad , \; R_{12,43} = V_{43} / I_{12} \\ R_{32,41} = V_{41} / I_{32} \quad , \; R_{23,14} = V_{14} / I_{23} \\ R_{43,12} = V_{12} / I_{43} \quad , \; R_{34,21} = V_{21} / I_{34} \\ R_{14,23} = V_{23} / I_{14} \quad , \; R_{41,32} = V_{32} / I_{41} \end{cases} \tag{2.12}$$

We define R_A and R_B as:

$$\begin{cases} R_A = \left(R_{21,34} + R_{12,43} + R_{43,12} + R_{34,21}\right)/4 \\ R_B = \left(R_{32,41} + R_{23,14} + R_{14,23} + R_{41,32}\right)/4 \end{cases} \tag{2.13}$$

R_A and R_B are related to the sheet resistance R_{sh} through the following Van der Pauw equation:

$$exp\left(-\frac{\pi R_A}{R_{sh}}\right) + exp\left(-\frac{\pi R_B}{R_{sh}}\right) = 1 \tag{2.14}$$

The sheet resistance (R_{sh}) can be deduced by solving the last equation numerically, but it can

be estimated from the following equation:

$$R_{sh} \approx \frac{\pi}{\ln(2)}\left(\frac{R_A+R_B}{2}\right) \tag{2.15}$$

c- Magnetic sensitivity and magnetic field resolution of Hall sensors

The sensitivity of the Hall effect device is the most crucial figure of merit of the sensor. The absolute magnetic sensitivity of a Hall sensor is defined as:

$$S_A = |\partial V_H/\partial B|_{I=const} \qquad \text{(Unit in V/T)} \tag{2.16}$$

and the supply-current-related sensitivity is given by [7]:

$$S_I = S_A/I = |\partial V_H/\partial B|/I \approx 1/eN_s \qquad \text{(Unit in VA}^{-1}\text{T}^{-1}\text{)} \tag{2.17}$$

The magnetic resolution depends on the Hall voltage (V_H) and noise level (V_{noise}). Johnson noise is the main noise component [8] defined by:

$$V_{noise} = [4k_B T R_S \Delta f]^{1/2} \tag{2.18}$$

where k_B is the Boltzmann constant, T is the absolute temperature, Δf is the measurement bandwidth and R_S is the series resistance defined by:

$$R_S = \frac{l}{\mu enwd} M \tag{2.19}$$

For cross sample the series resistance is related to the sheet resistance by the relation:

$$R_S = R_{sh}\frac{l}{w} M \tag{2.20}$$

where l and w are respectively the length and the width of the sample. The ratio Hall voltage (V_H) to noise voltage (V_{noise}) is defined by:

$$\frac{V_H}{V_{noise}} = \frac{R_H IB}{[4k_B T R_S \Delta f]^{1/2}} \tag{2.21}$$

The Hall voltage is proportionally depending to the bias current and the external perpendicular magnetic field according to the equation $V_H = R_H IB$, from this equation we deduce the Hall coefficient R_H by linear fitting of the graph $V_H = f(B, I)$.

The minimum detectable magnetic field deduced when the ratio $V_H/V_{noise} = 1$ is given by:

$$B_{min} = \frac{[4k_B T R_S \Delta f]^{1/2}}{R_H I} \tag{2.22}$$

Another parameter that defines the reliability of the Hall sensor is the offset-equivalent magnetic field. When the magnetic field is applied, the calculated voltage is sum of Hall voltage and an undesired parasitic voltage called offset voltage:

$$V_{total} = V_H + V_{offset} \tag{2.23}$$

The offset voltage is proportional to the input voltage and quasi independent on the magnetic field and caused by geometrical and electrical asymmetries of the Hall sensor [9]. The corresponding offset magnetic field is given by the following equation:

$$B_{offset} = \frac{V_{offset}}{S_A} \tag{2.24}$$

d- Offset reduction by spinning current technique

The offset can be canceled by means of calibration as long as the offset is constant. However, during the Hall sensor application, mechanical stresses, temperature variations and aging cause the sensor offset to fluctuate. The recalibration of the sensor is required, which is unwanted during the operating time. The spinning current is a method to cancel or to reduce the offset voltage without the need of the recalibration. This method based on measuring the Hall voltage parallel to the current and to the magnetic field, when the current rotate and change direction by angle of 90° in the clockwise direction, this gives four measurement steps in a cross Hall sensor.

2-2 Conclusion

Different kinds of magnetic sensors were introduced in this chapter. Hall sensors have the advantage of low mass and low power consumption compared with fluxgates, and linearity and the albescence of pronounced hysteresis compared with GMR and AMR sensors.

2-3 References

[1] J. Heremans; *"Solid-state magnetic field sensors and applications"*; Journal of Physics, D: Applied Physics. **26**, 1149 (1993).

[2] Richard Boll and Kenneth J. Overshott; *"Magnetic Sensors, Volume 5, Sensors"*; (John Wiley & Sons. 2008) p.42.

[3] S. Tumanski; *"Thin Film Magnetoresistive Sensors"*; (CRC Press 8 Juin 2001) p.1.

[4] E. H. Hall; *"On a new action of the magnet on electric currents"*; Am. J. Math. **2**, 287 (1879).

[5] M. H. Wieder; *"Transport coefficients of InAs epilayers"*; Appl. Phys. Lett. **25**, 206 (1974).

[6] L. J. Van der Pauw; *"A method of measuring the resistivity and Hall coefficient on lamellae of arbitrary shape"*; Philips technical review, **20(8)**, 220 (1958).

[7] M. Bando, T. Ohashi, M. Dede, R. Akram, A. Oral, S. Y. Park, I. Shibasaki, H. Handa and A. Sandhu; *"High sensitivity and multifunctional micro-Hall sensors fabricated using InAlSb/InAsSb/InAlSb heterostructures"*; J. Appl. Phys. **105**, 07E909 (2009).

[8] K. Takahashi, A. Yoshikawa and A. Sandhu; *"Wide Bandgap Semiconductors: Fundamental properties and modern photonic and electronic devices"*; (Springer 2007) p.300.

[9] Sergey Y. Yurish and Maria Teresa S. R. Gomes; *"Wide Smart sensors and MEMS"*; (Kluwer Academic Publishers) p.243.

Chapter 3

Two-dimensional electron gas heterostructures

In this Chapter, we give an overview on the two-dimensional electron gas (2DEG) formation in AlGaN/GaN heterostructure. We show the Hall sensors based on AlGaN/GaN heterostructures and on others conventional AlGaAs/GaAs heterostructures and AlInSb/InAsSb/AlInSb quantum wells Hall sensors, we introduce new Hall sensor based on two–dimensional $MoSe_2$ flake. The quantum Hall effect, which is the evidence of the two-dimensional electron gas existence, is describe.

3-1 Two-dimensional electron gas formation

Two semiconductors with different band gaps in contact form a heterojunction. There are three types of heterojuctions: straddling gap (type I), staggered gap (type II) and broken gap (type III), as shown in Figure 3.1.

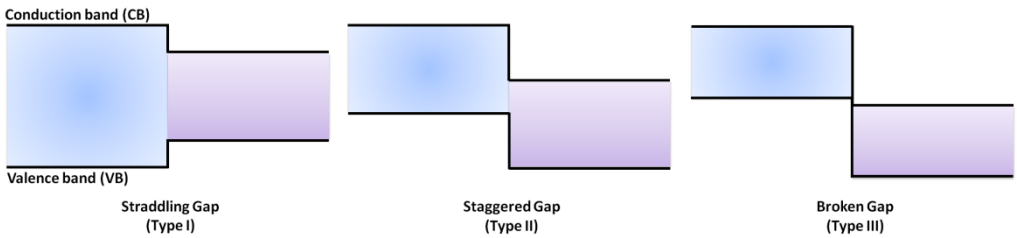

Figure 3.1 Classification of heterojunctions: (a) straddling gap (type I), (b) staggered gap (type II) and (c) broken gap (type III).

When two different semiconductors are in contact, a potential barrier (E_b) appear at the interface. The potential barrier is given by $E_b = e(\chi_1 - \chi_2)$, where χ_1 and χ_2 represent the electron affinities of the semiconductors. The conduction band offset is given by:

$$\Delta E_C = \chi_1 - \chi_2 = \Delta\chi \tag{3.1}$$

The valence band offset is simply given by:

$$\Delta E_V = \Delta E_g - (\chi_1 - \chi_2) \tag{3.2}$$

In the case when the work function and the electron affinity of the semiconductor (1) are higher than those of the semiconductor (2) and at the condition of $\chi_1 - \chi_2 < |\Delta E_g/e|$, electrons diffuse from the semiconductor (2) to the semiconductor (1) and accumulate at the interface. Holes cannot diffuse because of the sign of the barrier ΔE_V. A two–dimensional electron gas (2DEG) is formed in the semiconductor (1) at the interface, as shown in Figure 3.2. The two-dimensional gas formed in the interface is confined in the triangular well (or in the rectangular well in the case of quantum wells).

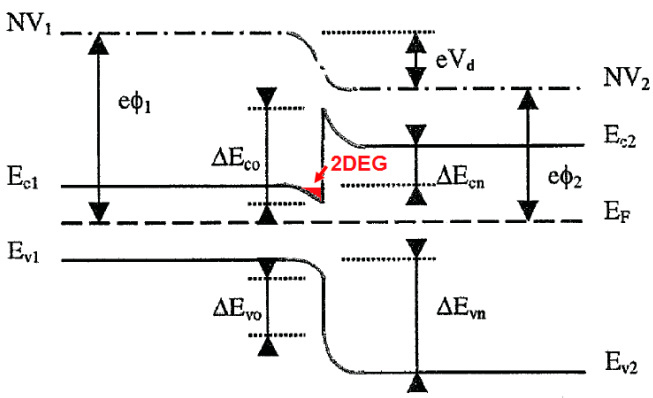

Figure 3.2 Band structures of heterojunction between two different semiconductors with $\phi_2 < \phi_1,\ \chi_2 < \chi_1\ and\ \chi_1 - \chi_2 < |\Delta E_g/e|$.

3-2 2DEG formation in AlGaN/GaN heterostructures

We focus our discussion on the 2DEG formation in AlGaN/GaN heterostructures rather in others 2DEG heterostructures shown in Chapter 5, since AlGaN/GaN heterostructures is our primary interest.

The gallium nitride (GaN), at room temperature and atmospheric pressure, has the wurtzite structure and exhibits hexagonal unit cell with a basis of four atoms, two Nitrogen and two

Gallium atoms. The unit cell of the wurtzite structure is shown in Figure 3.3. It contains six atoms and it is characterized by two lattice constants, $a_0(3.18\ A)$ and $c_0(5.18\ A)$.

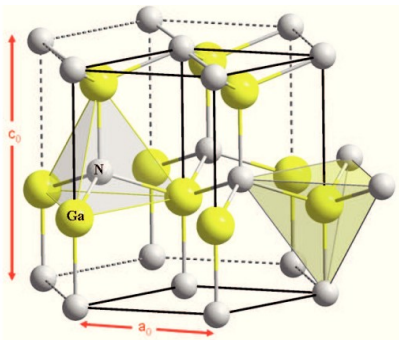

Figure 3.3 The wurtzite unit cell of GaN with lattice constants a_0 and c_0 [1].

Two different orientations of GaN crystals can be distinguished, Ga–face and N–face, depending if the material is grown with Ga or N on top and corresponding to the (0001) and $(000\bar{1})$ crystalline faces, due to the wurtzite structure non–inversion symmetry in the c–axis direction (the [0001] direction).

Each atom in the GaN wurtzite is tetrahedral bonded to four atoms of the other type. There is also an ionic contribution of the bound due to the large difference in electronegativity of Ga and N atoms. Due to its high electronegativity, the nitrogen leads to a strong interaction between the covalent bonds. The ionicity induced by the Coulomb potential of the N atomic nucleus is responsible for the formation of a polarization effect in all the material along the [0001] direction [1]. This effect is called spontaneous polarization P_{SP}.

The GaN is considered an outstanding material for optoelectronics, high power, and high frequency devices. The GaN has wide band-gap (3.39eV), which is responsible for the high critical electric field (3.3 MV/cm), making the GaN of big advantage for high voltage devices fabrication. Another advantage of the GaN and the wide–bandgap semiconductors in general the low intrinsic electron concentration n_i. The value of n_i in GaN at room temperature is of several orders of magnitude lower with respect to that of Si or GaAs, and comparable with

that of SiC, enabling the increase of the maximum operation temperature of the devices made of this material and have reduced leakage currents. The most important advantage of the GaN materials is the possibility to grow on $Al_xGa_{1-x}N$ alloy, forming $Al_xGa_{1-x}N$/GaN heterostructures with a 2DEG at the interface between the $Al_xGa_{1-x}N$ and the GaN. The energy gap and the lattice constant (a) of the $Al_xGa_{1-x}N$ alloy depend on the Aluminum concentration x, as shown by equations (3.3) and (3.4) [2]:

$$E_g^{AlGaN}(x) = xE_g^{AlN} + (1-x)E_g^{GaN} - x(1-x) \tag{3.3}$$

$$a^{AlGaN}(x) = \mathrm{x}a^{AlN} + (1-x)a^{GaN} \tag{3.4}$$

In the addition of the spontaneous polarization in the GaN, the piezoelectric nature of the materials (AlGaN and GaN) allows a strain inducing due to the lattice mismatch at the interface between the AlGaN and GaN. The strain induced generates an additional contribution to the polarization, namely, the piezoelectric polarization P_{PE}. When the AlGaN and GaN layers are in contact, a high sheet electron density appears at the interface due to the presence of the piezoelectric polarization either without using n-doped layers; which reduces the Coulomb scattering and enhances the electron mobility in the 2DEG.

The strength of the piezoelectric polarization P_{PE} is given by the equation (3.5) [3]:

$$P_{PE} = \frac{2(a-a_0)}{a_0}\left(e_{31} - e_{33}\frac{C_{13}}{C_{33}}\right) \tag{3.5}$$

Where a and a_0 are the lattice constants of the layer and the buffer layer, respectively, e_{31} and e_{33} are piezoelectric coefficients, C_{13} and C_{33} are the elastic constants. The term $\left(e_{31} - e_{33}\frac{C_{13}}{C_{33}}\right)$ is always negative, therefore, the piezoelectric polarization is negative for tensile strain ($a > a_0$) and positive for compressive strain ($a < a_0$). In the case of the Ga–face heterostructures, the spontaneous polarization vector of GaN will be negative pointing towards the substrate and in the reverse direction in the case of the N–face. The spontaneous and the piezoelectric polarization directions in the AlGaN/GaN heterostructures in both case of Ga– and N–faces are shown in Figure 3.4. The polarization induced sheet

charge density (σ), is shown also in the same figure. The sheet charge density in the AlGaN/GaN heterostructures is given by:

$$\sigma = [P_{SP} + P_{PE}]^{AlGaN} - [P_{SP} + P_{PE}]^{GaN} \tag{3.6}$$

The sheet charge density (N_s) is deponds on the Al mole fraction x of the AlGaN barrier layer, and it is given by the equation:

$$N_s(x) = \frac{\sigma_{int}}{q} - \left[\frac{\varepsilon_0 \varepsilon_{AlGaN}(x)}{d_{AlGaN} q^2}\right]\left[q\phi_B(x) + E_{F_0}(x) - \Delta E_C(x)\right] \tag{3.7}$$

Where σ_{int} the polarization induced bound sheet charge density at the AlGaN/GaN heterojunction, ϕ_B is the Schottky barrier height, E_{F_0} is the Fermi level at the heterojunction with respect to the GaN conduction band edge, ΔE_C is conduction band offset at the AlGaN/GaN interface, ε_{AlGaN} is the relative dielectric constant, d_{AlGaN} is the AlGaN thickness, q is the elementary charge and ε_0 is the vacuum permittivity.

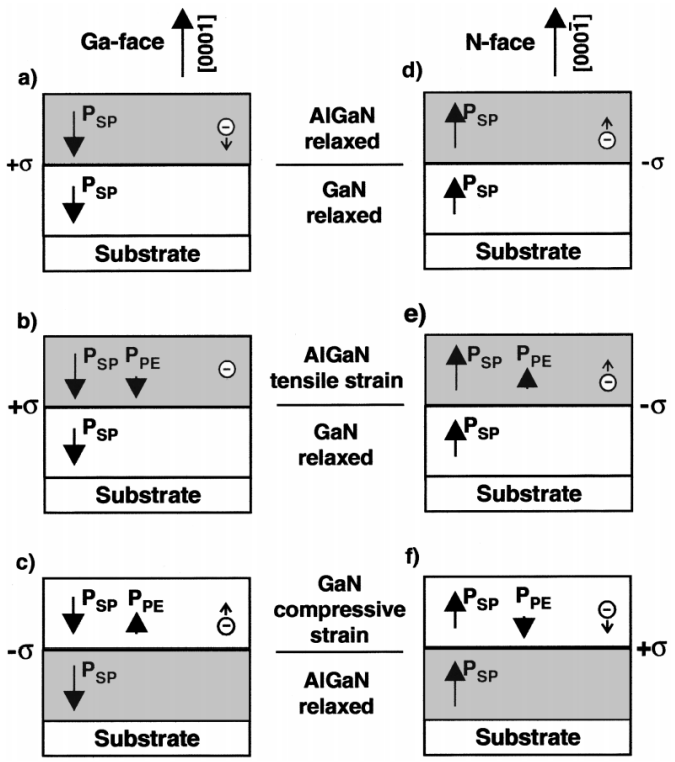

Figure 3.4 Spontaneous and piezoelectric polarizations in Ga– and N–face strained and relaxed AlGaN/GaN heterostructures [4].

$\phi_B(x)$ and $\varepsilon_{AlGaN}(\mathrm{x})$ are given by:

$$\begin{aligned} \varepsilon_{AlGaN}(x) &= -0.5\mathrm{x} + 9.5 \\ q\phi_B(x) &= 1.3x + 0.84\ eV \end{aligned} \tag{3.8}$$

The Fermi level is given by:

$$E_F(x) = E_0(x) + \frac{\pi\hbar^2}{m^*(x)} N_s\,(x) \tag{3.9}$$

m^* is the effective electron mass and $E_0(x)$ represent the ground subband level of the 2DEG:

$$E_0(x) = \left[\frac{9\pi\hbar q^2}{8\varepsilon_0\sqrt{8m^*_{AlGaN}(x)}}\frac{N_s\,(x)}{\varepsilon_{AlGaN}(x)}\right]^{2/3} \tag{3.10}$$

The sheet electron density decreases by decreasing the Al concentration of the AlGaN barrier layer or by decreasing its thickness.

3-3 Quantum Hall effect

Von Klitzing *et al.* discovered the quantum Hall effect in a two–dimensional electron gas system in 1980 [5]. In a two–dimensional electron gas, when electrons are subjected to a perpendicular magnetic field they follow circular cyclotron orbits with the cyclotron frequency $\omega_C = eB/m^*$, as shown in Figure 3.5(a). The kinetic energies allowed are discrete, which results in the formation of Landau levels, as shown in Figure 3.5(b). The energy on the nth level for a subband n is written as:

$$E_n = E_0 + \hbar\omega_C(n + 1/2)\ \ where\ n = 0, 1, 2 \ldots \tag{3.11}$$

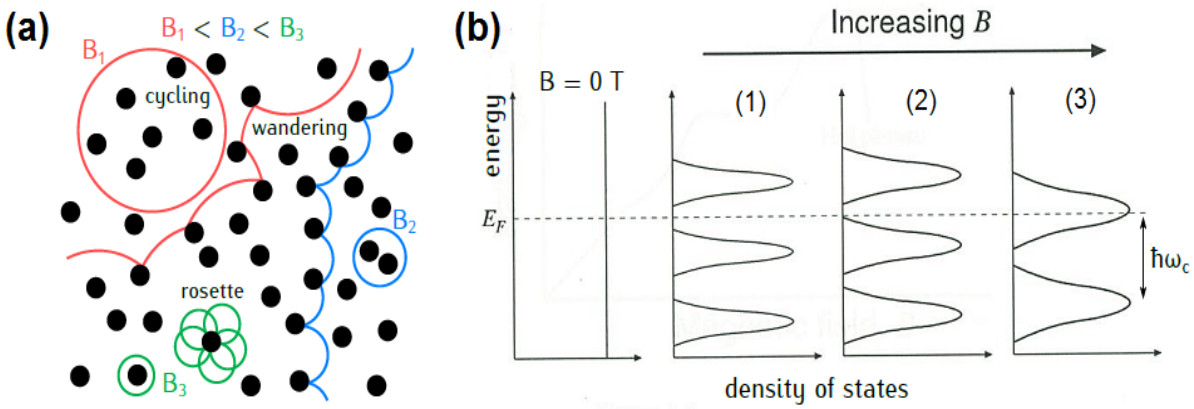

Figure 3.5 (a) Trajectories of carriers at different magnetic fields and (b) schematic Landau levels [6].

The density of states has its peaks at Landau levels and the regions between the Landau levels are no allowed state. When the magnetic field increases the Landau levels move relative to the Fermi energy, as shown in Figure 3.5(b).

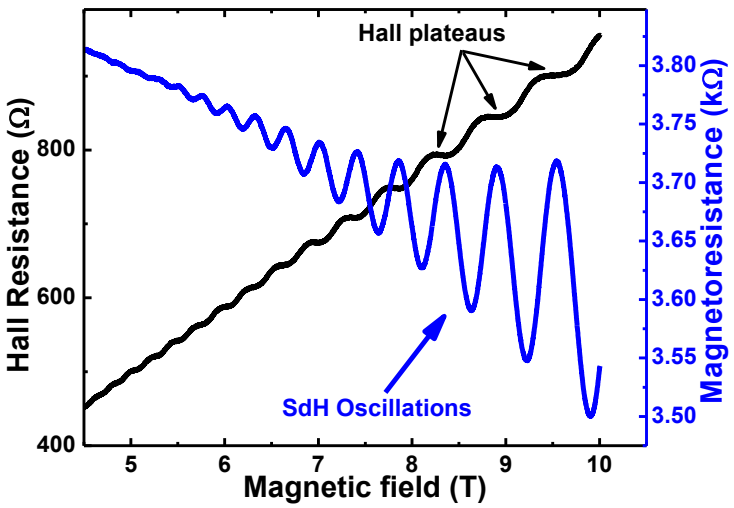

Figure 3.6 The Hall resistance and the magetoresistance at 4K in AlGaN/GaN heterostructures.

Between two successive Landau levels (between the state 1 to state 2 in the Figure 3.5(b)), electrons cannot move to new states, resulting in the absence of scattering, Therefore, the

magnetoresistance (the magnetic field dependence of the longitudinal resistance $R_{xx}(B)$) falls to zero. Simultaneously, the Hall resistance (the magnetic field dependence of the transversal resistance $R_{xy}(B)$) cannot change from the quantized value, resulting in a constant Hall resistance so called Hall plateaus shown in Figure 3.6.

3-4 Conclusion

The advantage of using AlGaN/GaN heterostructures as Hall sensors is the formation of a two-dimensional gas electron at the interface between the AlGaN and the GaN with high electron mobility and high electron density in a thin active region. In addition, the wide band gap of the AlGaN and GaN makes the heterostructures suitable for high temperature application.

3-5 References

[1] Giuseppe Greco; *"AlGaN/GaN heterostructures for enhancement mode transistors"*; International PhD in Nanoscience thesis, Università degli Studi di Catania, 2012.

[2] Z. Dridi, B. Bouhafs, and P. Ruterana; *"First-principles investigation of lattice constants and bowing parameters in wurtzite $Al_xGa_{1-x}N$, $In_xGa_{1-x}N$ and $In_xAl_{1-x}N$ alloys"*; Semicond. Sci. Technol. **18**, 850 (2003).

[3] Hadis Morkoç; *"Handbook of Nitride Semiconductors and Devices, Materials Properties, Physics and Growth"*; (John Wiley & Sons, 2009) p.239.

[4] O. Ambacher, J. Smart, J. R. Shealy, N. G. Weimann, K. Chu, M. Murphy, W. J. Schaff, L. F. Eastman, R. Dimitrov, L. Wittmer, M. Stutzmann, W. Rieger, and J. Hilsenbeck; *"two–dimensional electron gases induced by spontaneous and piezoelectric polarization charges in N– and Ga–face AlGaN/GaN heterostructures"*; J. Appl. Phys. **85** (6), 3222 (1999).

[5] Klaus von Klitzing; *"The quantized Hall effect"*; Nobel lecture, Dec. 9, 1985.

[6] Daniel Broxtermann; *"Towards high electron mobility in GaN (0001) based InGaN and AlGaN heterostructures"*; Doctor rerum naturalium, der Georg-August-Universität Göttingen, 2011.

Chapter 4

Materials in harsh environment

An extreme harsh environment includes extremes of temperature, pressure, shock, radiation, and chemical attack. We focus our study on high temperature and radiation environments. In nature, there are six different radiation environments, but we will discuss the two main environments: the space and the nuclear environments.

4-1 Space environment

4-1-1 Temperature in the space environment

The temperature in the outer space is relative and it depends on the position from the sun. The temperature at the first planet in our solar system surface is about 450°C and –170°C in the morning and night sides of the planet, and the average temperature on the planet Pluto is –230°C. The temperature in the vacuum in the space is relative to an object, and it is around -270°C. Therefore, a magnetic sensor for space application should work in very wide range of temperature

4-1-2 Radiation in the space environment

The main components of a space environment are the particles trapped in the Van Allen belts, the cosmic rays, and the charged particles coming from solar flares. The Van Allen belts surrounding the earth are shown in Figure 4.1. The inner radiation belt was discovered and named by James Van Allen and his team using the satellite *Explorer 1* launched on January 31, 1958 [1]. The Pioneer spacecraft discovered the outer belt. The inner belt contains mostly protons with energy up to several hundred of MeV and the outer belt electrons with energy up

to several hundred of MeV [2].

The diameters of the belts and the distances of some satellites from the earth surface are shown in Figure 4.1 [3].

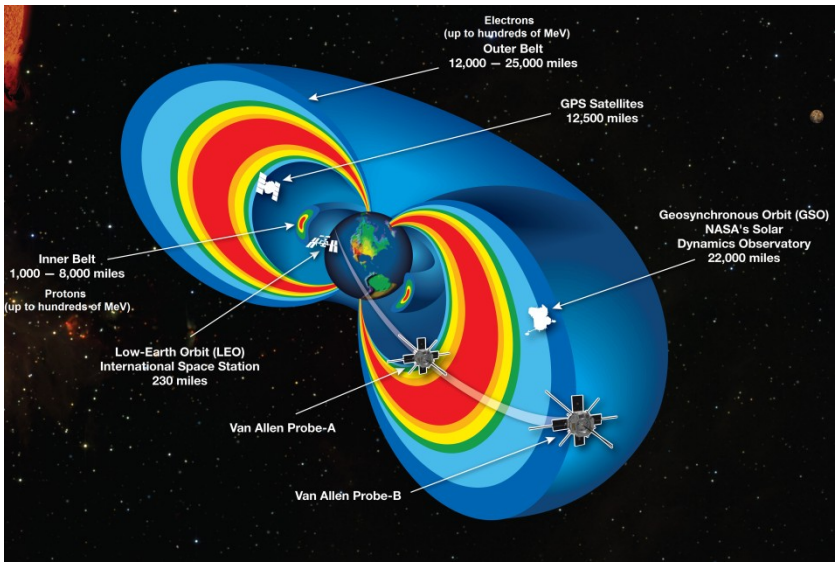

Figure 4.1 The Van Allen belts surrounding the earth.

The Cosmic rays are of three kinds, Galactic, solar, and terrestrial cosmic rays. Galactic (outside solar system) contains elements from atomic number 1 to 92 (1%), alpha particles (14%) and protons (85%) with low flux levels but energetic up to several hundreds of GeV. Solar cosmic rays include both UV and X–rays, and energetic solar materials and terrestrial cosmic rays are generated from collisions of primary cosmic radiation as it diffuses through the earth's atmosphere [2].

Solar flares generally eject heavy ions, and protons with energies higher than 100 MeV. Protons coming from solar flares are likely to be low energetic than those trapped in the Van Allen belts, but the semiconductor based devices in satellites can be exposed to considerable total fluence levels, same as what happened in October 1989 when a major flare caused a significant damage to a number of spacecrafts.

4-2 Nuclear environments

Gamma and neutron are the main constituents of the nuclear environments. Compared to the space environment, much higher doses and fluxes are involved in the nuclear environments. In nuclear reactors, the average values for neutrons and gamma bombardments are around $10^{10} – 10^{14}$ (cm^{-1} s^{-1}) and 10^{10} (rad/h) (Energy> 10 keV), respectively. Nuclear weapons is a nuclear environment, constituent of neutrons with energy extending 14MeV, X-rays, gamma rays with energy up to 12MeV, alpha particles, and other secondary particles. Thermonuclear reactors are the new generation of the energy sources in the world due to their high efficiency compared with others sources of energy. The neutron fluence in a thermonuclear reactor (ITER) varies from 10^{16} to 10^{20} (n/cm^2) [4], two kind of neutrons exist in the thermonuclear (ITER), fast neutrons with energy above 1MeV and thermal neutrons with energy below 0.1MeV [5].

4-3 Fundamental radiation damage mechanisms in semiconductors

Different physical processes are involved by particles–semiconductor interaction. High energy particles and photons when interacting with the semiconductor can lose their kinetic energies in two different ways, ionization and displacement damage [2]. The particles–semiconductor interaction give rise to a degradation of the performance of the devices used in the harsh environment. the incident radiation is characterized by its energy and its particle flux (the flux can be expressed by fluence measured in units of particle/surface area).

4-3-1 Ionization effect

Since electrons occuppy most of the atomic volume, interaction charged particles–electrons is most likely to occur. In this process, a small amount of energy is transferred to an electron by

the incoming particle then absorbed by the electron which jump from the valence to the conduction band. The minimum energy required to create an electron in the conduction band and hole in the valence band is the bandgap energy (E_g). The total dose levels in typical space applications range from less than 5 krad (Si) for the International Space Station to as much as 1-Mrad(Si) for a spacecraft that goes through the intense regions of the earth's radiation belts, or in the radiation belts near Jupiter [6]. The units rad is defined as 100 ergs absorbed in 1 g of a specific material (1 j/kg =1 gray = 100 rads).

4-3-2 Displacement damage

Displacement damage disrupts the regular atomic spacing by moving away the lattice atoms from their initial positions, creating vacancies. The minimum energy (threshold energy) needed to displace an atom from its initial position depends on the crystal binding energy which is correlated with the reciprocal of the lattice spacing. The threshold energy of some bulk semiconductors is shwon in Table 4.1.

Table 4.1 The displacement threshold energy of some bulk semiconductors [6,7].

Semiconductors	**InSb**	**InAs**	**GaAs**	**Si**	**GaN**	**4H-SiC**
Threshold energy (eV)	5.7–6.6	7.4	9.5	12.9	19.5	21.3

As we can see from Table 4.1 the GaN has higher displacement threshold energy than InSb, GaAs and Si, which makes GaN based-devices more suitable for radiation environment.

4-3-3 Transmutation

Neutrons in thermonuclear environment are dived into fast and thermal neutrons. Fast neutrons caused structure damage by creating defects in the crystal lattice contrariwise to the

thermal neutrons, which are responsible of the transmutation of nucleus. As an example, the gallium nitride during irradiation with thermal neutrons transmutes according to the following nuclear reactions:

$$\left[\begin{array}{l} {}^{60}\mathrm{Ga}(\mathrm{n},\gamma)\ {}^{70}\mathrm{Ga}(\mathrm{T}_{\frac{1}{2}} = 21.15\mathrm{min}) \longrightarrow {}^{70}\mathrm{Ge} \\ \quad {}^{71}\mathrm{Ga}(\mathrm{n},\gamma)\ {}^{72}\mathrm{Ga}(1.41\mathrm{h}) \longrightarrow {}^{72}\mathrm{Ge} \\ \qquad {}^{14}\mathrm{N}(\mathrm{n},\gamma)\ {}^{15}\mathrm{N} \\ \quad {}^{15}\mathrm{N}(\mathrm{n},\gamma)\ {}^{16}\mathrm{N}(7.13\mathrm{s}) \longrightarrow {}^{16}\mathrm{O} \end{array}\right. \tag{4.1}$$

4-4 Magnetic sensors for harsh environments

4-4-1 Magnetic sensors for high temperature environment

The magnetic sensors are used in the oil and gas exploration systems [8], in the automotive and aircraft engines [9], in the gas turbines as speed sensors [10], as a part of crack monitoring system [11] and in the diagnostic system of the thermonuclear reactors [4]. In such environments, the magnetic sensors should be tolerance to the high temperature and of a good reliability. Figure 4.2 represents some high temperature applications where magnetic sensors are used.

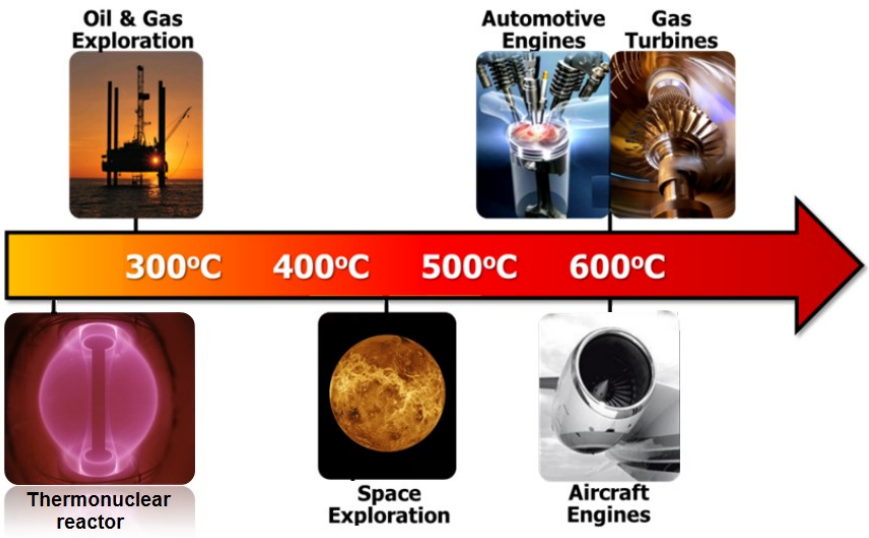

Figure 4.2 High temperature environments require magnetic sensing.

Magnetic sensors are used also in some others harsh environment application, where they should be tolerant not only against the high temperature but also against particles and/or electromagnetic waves such as protons, gamma irradiation for space exploration applications [12,13], against particles in charged particle accelerators as part of monitoring magnetic fields systems [14] and neutrons for thermonuclear power stations diagnostic systems [15,16].

4-4-2 Magnetic sensors for high proton irradiation environment

Monitoring of the magnetic field of planets and rocks in space is one of the various applications of the magnetic sensors. Magnetic sensors for scientific space missions must have detectivity less than 50 $pTHz^{-1/2}$, and for the satellites attitude determination application, they needs to have detectivity of about 100 $nTHz^{-1/2}$ down towards few tens $nTHz^{-1/2}$ [17]. Fluxgate and magnetoresistance based magnetic sensors such as anisotropic magnetoresistors (AMR) and giant magnetoresistors (GMR) are the most used for space application nowadays due to their high magnetic sensitivity. However, fluxgates have high mass and power consumption that limits their use for space application. In addition, the use of AMR and GMR for space application is limited by their inherent low-frequency noise, their relatively poor linearity and pronounced hysteresis [17]. Hall sensors are promising for space applications, due to their low cost, robustness, versatility and the possibility of their integration in the same measurement ship, however, the detectivity is not sufficient, compared to fluxgates. Improvement of the Hall sensors sensitivity and therefore their detectivity can be achieved. Kunets et al. [18] have reported on micro-Hall sensor based InSb based quantum well where the minimum detectable magnetic field is in sub-nano-Tesla (nT) range at room temperature and high frequency. In addition, geometric enhancement [19] and flux concentrator integration into the Hall sensors [20] can improve their sensitivity by 56 and 100 folds, respectively. One of the problems facing the use of these Hall sensors in space

is the high electromagnetic and energetic particles coming from solar flares and/or cosmic rays [2], dominated by proton particles.

As we can see in Figure 4.1, the satellites are positioned at regions where the proton flux is minimum. The AP8 for solar minimum and maximum referred as AP8–MIN and AP8–MAX, respectively, are models developed by NASA used for modulation of the trapped proton population in the inner and the outer Van Allen belts [21]. Proton with energies higher or equal to 100 keV, 1 MeV and 400 MeV are trapped at the inner and the outer Van Allen belts. We estimated the average of the proton fluence during ten years from the proton flux given by protons per second and per unit of surface (cm^2) according to the AP8–MIN model. The total proton fluences during 10 years estimated from the AP8–MIN model of proton with different energies are shown in Figure 4.3.

For space applications, searchcoils are the most used for magnetic field sensing due to their ability to measure weak magnetic fields. Searchcoils magnetometers are dedicated to the space plasma characterization in order to provide a better understanding of problems such as dynamics of the terrestrial magnetosphere and its interaction with the solar wind [22]. Some of the space missions dedicated to plasma studies are CLUSTER that was launched in 2000, and a complementary two satellites mission, called Double Star, launched in 2004, which permit a better understanding of the Earth magnetosphere. Searchcoil was also used in BepiColombo mission, to better understanding of the nearly unknown magnetosphere of Mercury.

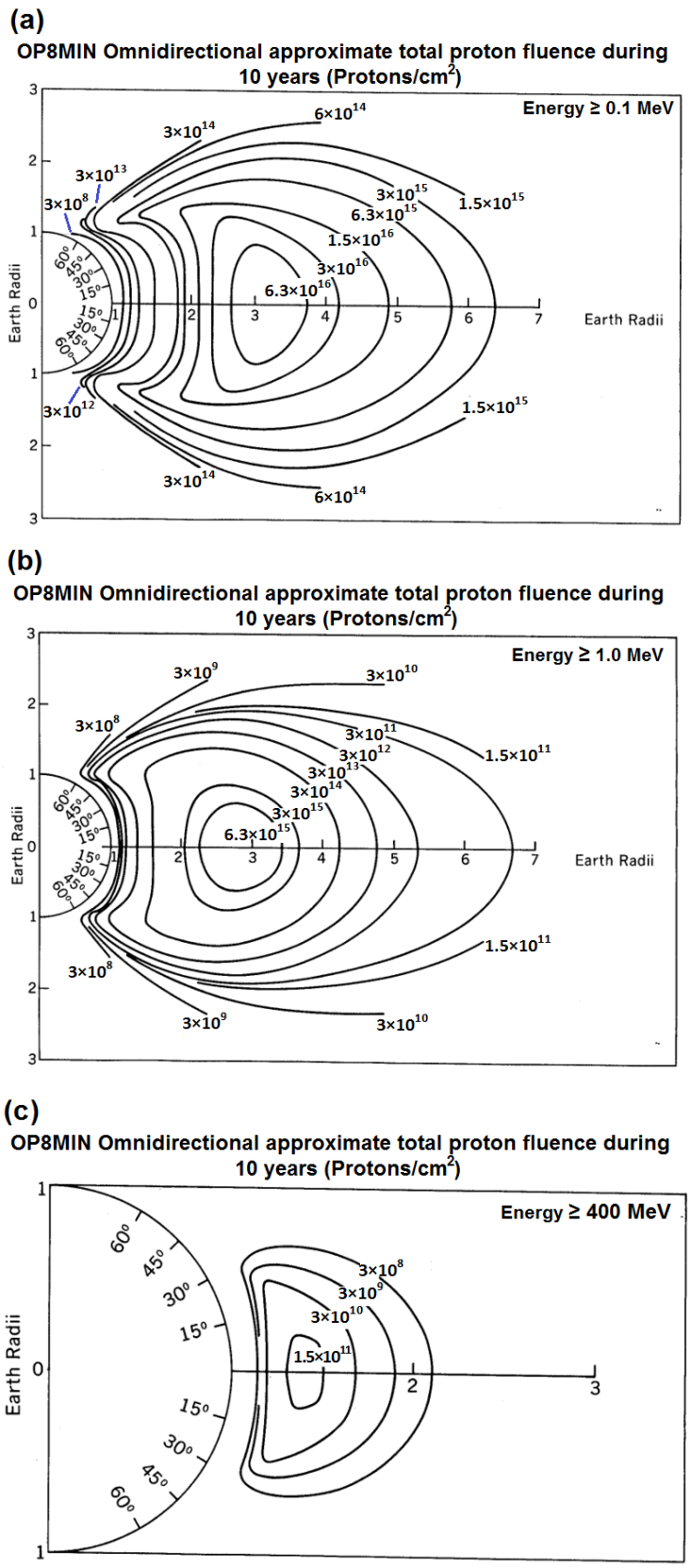

Figure 4.3 The estimated proton fluences during 10 years in function of the earth radii, of proton with energy equal or exceed (a) 100 keV, (b) 1.0 MeV and (c) 400 MeV.

The trajectory of the CLUSTER and Double Star satellites are shown in Figure 4.4.

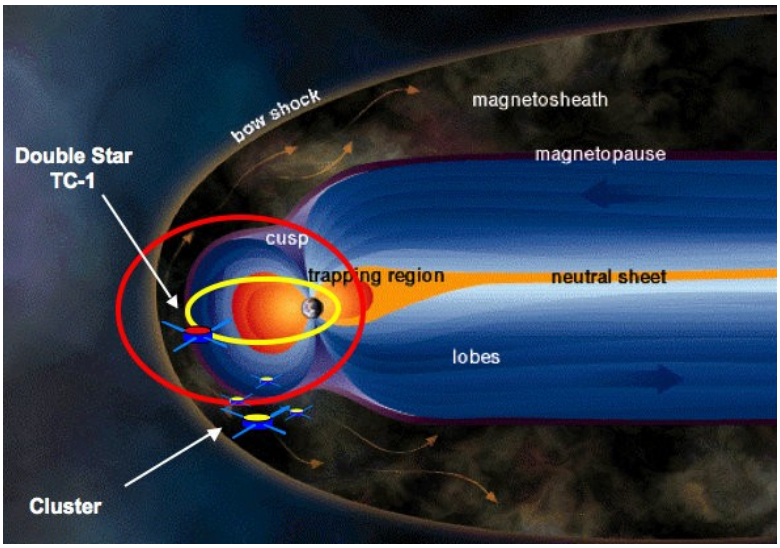

Figure 4.4 CLUSTER and Double Star satellites trajectory around the earth.

The estimation of the total proton fluence that these satellites are exposed to is impossible. However, we can deduce the total proton fluence that satellites with fixed altitudes above the earth surface are exposed to during a fixed period. In our study, we used a proton irradiation fluence, which varies between the 10^{11} and 10^{16} protons/cm^2, a values equivalent to years to thousands of years of application lifetime of a satellite positioned in the low-earth orbit.

4-4-3 Magnetic sensors for high neutron irradiation environment

The ITER thermonuclear reactor is the new version of JET which represents the largest tokomak existing, in the aim to increase its efficiency and reducing its size. The typical neutron flux in ITER varies between 10^9 to 10^{13}(n/cm^{2}s) in relevant locations, a significant fraction is 14MeV. The flux values in ITER represent 10 times higher than the neutron flux in JET thermonuclear reactor; The neutron fluence in ITER varies between 10^{16} to 10^{20} (n/cm^2) over the ITER lifetime which is 1 million higher than the fluence in the JET reactor [4]. The gamma dose rate in ITER varies between 10^{-2} to 10^2 (Gy/s) [4] which is 10 times higher than

gamma irradiation in JET reactor. Figure 4.5 represents the cross section of ITER and corresponding radiation flux at each position.

Two kinds of neutrons are present in ITER, fast neutrons with energy above 1MeV and thermal neutrons with energy below 0.1MeV [5].

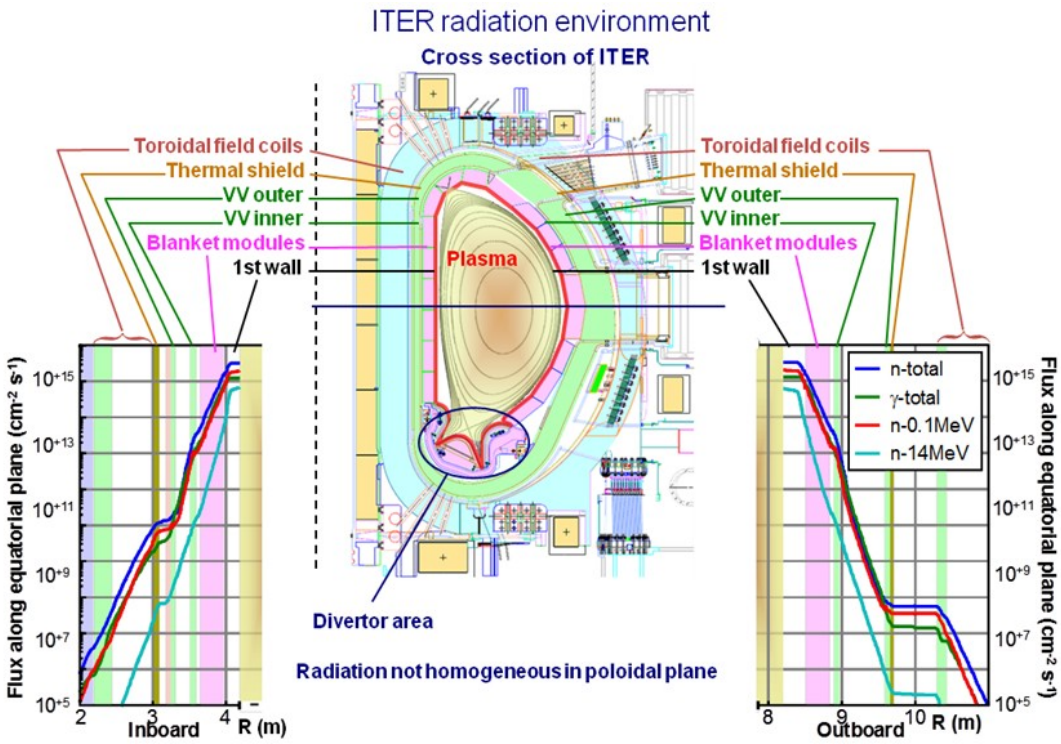

Figure 4.5 ITER radiation environment [23].

Table 4.2 resumes the irradiation fluences at different positions in ITER, the values are extracted from figure 1 and reference [24].

Table 4.2 Radiation environment in the ITER.

Location Typical mag. diag. component		Neutron irradiation			
		Flux (n/cm^2s^{-1})		Fluences (n/cm^2)	
		0.1 MeV	14 MeV	0.1 MeV	14 MeV
First wall		6×10^{14}	6×10^{13}	6×10^{21}	6×10^{20}
Blanket gap on vacuum vessel	[Mag. Coils]	1×10^{14}	3×10^{12}	1×10^{21}	3×10^{19}
Vacuum vessel (behind blanket)	[Mag. Loops]	2×10^{13}	2×10^{11}	2×10^{20}	2×10^{18}
Vacuum vessel (Inboard TFC side)	[Mag. loops]	1×10^{10}	1×10^{8}	1×10^{17}	1×10^{15}

The operating temperature of the components used for diagnostic in the in-vessel environment is 150°C and 240°C during baking, but the components which are not well cooled may get hotter [4].

The lifetime of ITER is 20 years, and the operational time is about 4700 hours [5], some of the components in ITER are unchangeable during all the ITER lifetime. So, the components used for diagnostics must be tolerant to high fluence neutron and gamma irradiations and tolerant to high temperature. The role of the magnetic diagnostics is to measure and control the plasma shape, which is a big challenge, compared with the magnetic diagnostics used in the thermonuclear reactors used in present days. The magnetic diagnostic system must be of high accuracy and high reliability.

Almost the sensors used in ITER are inductive except for those used in the ex-vessel. Integration of these sensors is needed but they are sensitive to drifts, noise, radiation and thermally noise induced voltage. It should be noted that new effects expected to appear in ITER which are not encountered on present days reactors because of the high neutron fluences. Two main effects concerning the inductive magnetic field sensors are [4]:

Radiation induced electrical degradation (RIED) and radiation-induced conductivity (RIC) due to high dose of neutron irradiation particles.

Induced voltage and current in cables driven by thermal gradients and nuclear reaction in mineral insulated cables, such as radiation-induced electromotive force (RIEMF), thermally induced EMF (TIEMF) and radiation induced thermoelectric sensitivity (RITES).

The steady state magnetic diagnostic in fusion reactor is based on the measurement of the magnetic field induced by current flowing through the plasma. In the currently reactors, inductive pick-up coils with analog integration of signal are used but this kind of sensors will be insufficient accurate for future magnetic devices (ITER). Very slow movement of the plasma towards the wall will be partially unrecognizable because the signal obtained will be bellow the drift level of the integrator.

Ďuran *et al.*[15] studied the $InAs_xSb_{1-x}$ doped tin based Hall sensors which are stable under neutron irradiation compared with InSb based Hall sensors doped with others doping agent. Two processes affect the stability of the Hall sensors. First, the thermal neutrons cause the transmutation of indium into tin. Tin created by the transmutation act as donors in InSb increasing the free charge carrier density and therefore decreasing in the sensitivity of the Hall sensor. Second, the fast neutron cause structure damage by creating defects in the crystal lattice causing acceptor doping which has effect to decrease the free charge carrier density and therefore increasing the Hall sensitivity. The temperature dependence of normalized sensitivity of sensors is shown in Figure 4.6. The sensor studied is shown in the inset of the same figure.

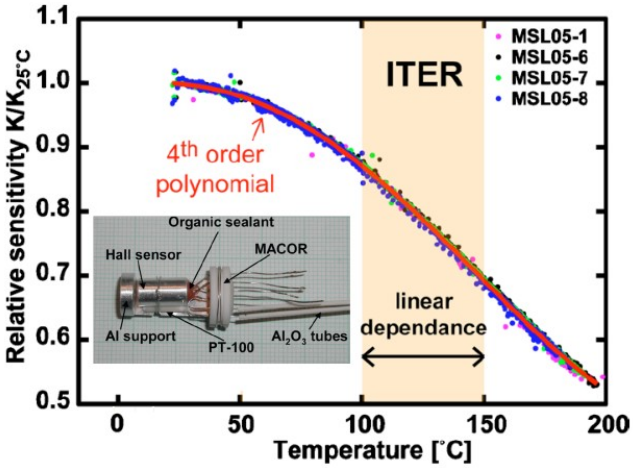

Figure 4.6 Normalized Sensitivity of tested sensors. The inset represents the Hall sensor sample mounted on aluminum support [15].

The sensitivity of sensor studied decreased by factor of 52% at 200°C. These sensors were irradiated during 20 days in LVR fission reactor, the sensitivity, the offset voltage and temperature of sensors were continuously monitored during the irradiation.

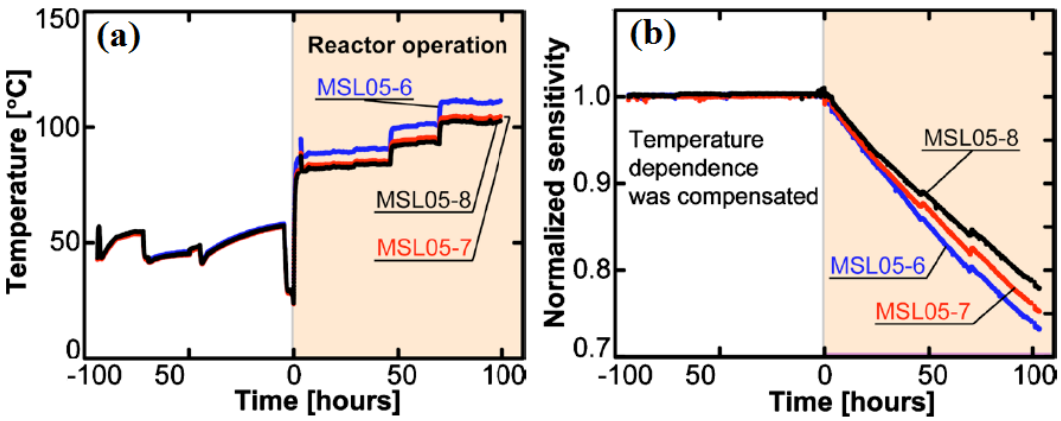

Figure 4.7 Evolution of Hall sensors parameters during irradiation. (a) Temperature of the sensors. (b) Sensitivity of the sensors normalized to their pre-irradiation values and recalculated to room temperature [15].

The reactor operational temperature was not constant and change during operation as shown in Figure 4.7(a). The Figure 4.7(b) shows the variation of the sensors sensitivity recalculated to room temperature and normalized to its pre-irradiation value.

The sensitivity of the samples was down to about 75% after 100 hours irradiation time, the experiment was stopped because of operation error. The total neutron irradiation and remaining sensitivity of the three samples are shown in Table 4.3. The magnetic sensitivities of the sensors irradiated by fast neutron in U-120M remain stable.

Table 4.3 The remaining sensitivity of three Hall sensor samples en function of neutron irradiation fluences [15].

Hall sensor	Total neutron fluence (cm^{-2}) [0 - 20MeV]	Fast neutron fluence (cm^{-2}) [0.1 - 20MeV]	Remaining sensitivity (%)
MSL05-6	7.2×10^{16}	3.6×10^{16}	73.2
MSL05-7	7.2×10^{16}	2.9×10^{16}	75.2
MSL05-8	8.0×10^{16}	2.4×10^{16}	77.9

The total neutron fluence used in Ref.24 was in order of 10^{16} cm^{-2} exceeding the total

expected ITER lifetime's fluence at low field side location used for steady state magnetic sensors which is 6.4×10^{15} cm^{-2}. The sensors showed 30% decay in sensitivity after thermal neutron irradiation but no change after fast neutron irradiation therefore the transmutation is the dominant process affecting the $InAs_xSb_{1-x}$ doped tin based Hall effect sensor sensitivity.

The studies of the effect of neutron irradiation on AlGaN/GaN heterostructures are very few, Zhang *et al.* studied the effect of neutron irradiation on the 2DEG AlGaN/GaN [25]. They remark sharply drop in the mobility after low fluence of 6.13×10^{15} $n\cdot cm^{-2}$ irradiation while the sheet carrier density remains the same and drop slightly for a fluence of 3.66×10^{16} $n\cdot cm^{-2}$. They attributed the degradation of the mobility to the defects induced by neutron irradiation. The irradiation does not cause the distortion of the crystal structure only but also introduce charged defect centers such as displacement defects and point defects. The effect of 1 MeV neutron irradiation at fluence up to 10^{15} $n\cdot cm^{-2}$ on SiN-passivated AlGaN/GaN was reported by Gu *et al.* [26]. There was negligible change in drain source current after current-voltage characteristics either at high fluence. They suggested that the passivation shields most of the irradiation damage. These studies showed that AlGaN/GaN heterostructures could be used as Hall sensors for thermonuclear (ITER) diagnostic system to measure the magnetic field at low field side location.

4-5 Conclusion

Due to high threshold displacement energy of the GaN, the electronic devices based on this material are suitable for harsh environment applications such as space and thermonuclear environments. According to previous study, AlGaN/GaN heterostructures can be used as part of the diagnostic system in the thermonuclear reactors. AlGaN/GaN heterostructures based micro-Hall sensors are suitable also for space environment, as we will see in the next chapter.

4-6 References

[1] Michael J. Carlowicz and Ramon E. Lopez; *"Storms from the Sun: The Emerging Science of Space Weather"*; (Joseph Henry Press 2003).

[2] Thomas B. Elliot, "*Focus on Semiconductor Research*", (Nova Science Publishers, Inc. 2005).

[3] *"Van Allen Probes: Studying Earth's Radiation Belt Region"*; http://www.nasa.gov/mission_pages/rbsp/main/index.html.

[4] Christian Ingesson; *"Designing diagnostics for life in the ITER Vessel"*; Fusion Energy Seminar - Barcelona Tech Summer Sessions, 1 July 2010.

[5] K. Kovařík, I. Ďuran, J. Sentkerestiová, M Oszwaldowski, L. Viererbl, I. Boshakova, R. Holyaka, V. Erashok; *"Status of Development of High Temperature Radiation Hardened Hall Sensors for Energy Producing Fusion Devices"*; WDS'12 Proceedings of Contributed Papers, Part II, 216–221, 2012.

[6] Allan Johnston; *"Reliability and radiation effect in compound semiconductors"*; (World Scientific Publishing Co. Pte. Ltd. 2010).

[7] N. Itoh and A. M. Stoneham; "*Materials modification by electronic excitation*"; (Cambridge University Press 2001).

[8] *"Application area: Oil & Gas Industry"*; http://www.iitechn.com/english-1/products/application-area-oil-gas-industry.

[9] J. Lenz, A. S. Edelstein; *"Magnetic sensors and their applications"*; IEEE Sensors J. **6**, 631 (2006).

[10] Karstensen, Karl W., and Brace C. Smith; *"Speed sensor mounting for a gas turbine"*; U.S. Patent No. 4,075,562. 21 Feb. 1978.

[11] N. H. Ulerich, G. Kidane, C. Spiegelberg, and N. Tevs; *"Condition based monitoring of gas turbine combustion components"*; Final technical report (2013).

[12] Marina Díaz-Michelena; *"Small magnetic sensors for space applications"*; Sensors **9**,

2271 (2009).

[13] P. C. de Jong, F. R. Riedijik, J. van der Meer; *"Smart silicon sensors - examples of Hall–effect sensors"*; Proceedings of IEEE Sensors **2**, 1440 (2002).

[14] I. Bolshakova, R. Holyaka, C. Leroy; *"Novel approaches toward the development of Hall sensor-based magnetometric devices for charged particle accelerators"*; IEEE Trans. Appl. Supercond. **12**, 1655 (2002).

[15] I. Ďuran, I. Bolshakova, L. Viererbl, J. Sentkerestiová, R. Holyaka, Z. Lahodová, and P. Bém; *"Irradiation tests of ITER candidate Hall sensors using two types of neutron spectra"*; Rev. Sci. Instrum. **81**, 10E122 (2010).

[16] I. Bolshakova, I. Vasilevskii, L. Viererbl, I. Ďuran, N. Kovalyova, K. Kovarik, Y. Kost, O. Makido, J. Sentkerestiová, A. Shtabalyuk and F. Shurygin; *"Prospects of using in-containing semiconductor materials in magnetic field sensors for thermonuclear reactor magnetic diagnostics"*; IEEE Trans. Magn. **49**, 50 (2013).

[17] A. Persson, R. S. Bejhed, F.W. Osterberg, K. Gunnarsson, H. Nguyen, G. Rizzi, M. F. Hansen and P. Svedlindh; "*Modeling and design of planar Hall effect bridge sensors for low-frequancy applications*"; Sensors and Actuators A-Physical, **189**, 459, Nov. 2013.

[18] V. P. Kunets, S. Easwaran, W. T. Black, D. Guzun, Y. I. Mazur, N. Goel, T. D. Mishima, M. B. Santos and G. J. Salamo; " *InSb quantum-well-based micro-Hall devices: Potential for pT detectivity*"; IEEE transactions on electron devices, **56** no. 4, 683, Mar. 2009.

[19] A. D. Henriksen, B. T. Dalslet, D. H. Skieller, K. H. Lee, F. Okkels, and M. F. Hansen; "*Planar Hall effect bridge magnetic field sensors*"; Appl. Phys. Lett., **97**, 013507, July. 2010.

[20] X. Sun, L. Jian, P. W. T. Pong, "*Magnetic flux concentration at micrometer scale*"; Microelectronic Engineering. **111**, 77, Nov. 2013.

[21] D. M. Sawyer, J. I. Vette,; *"AP–8 trapped proton environments for solar maximum and solar minimum"*; NSSDC/WDC–A–R&S 76–06, (1976).

[22] P. Leroy, C. Coillot, V. Mosser, A. Roux, G. Chanteur; *"An ac/dc magnetometer for*

space missions: Improvement of a Hall sensor by the magnetic flux concentration of the magnetic core of a searchcoil"; Sensors and Actuators A **142**, 503-510, (2008).

[23] Ph. Moreau, I. Bolshakova, B. Brichard, G. Chitarin, R. Delogu, I. Duran, A. Encheva, Y. Fournier, A. Gallo, A. Le-Luyer, J.B. Lister, Ph. Malard, J.M. Moret, P. Pastor, S. Peruzzo, J. Romero, D. Testa, M. Toussaint, G. Vayakis, R. Vila; "*Development of a Magnetic Diagnostic Suitable for the ITER Radiation Environment*"; Animma, Marseille june 7-10 2009.

[24] K. Ebisawa, A. E. Costley, A. J. H. Donne, G. Janeschitz, S. Kasai, A. Malaquias, G. Vayakis, C. I. Walker, S. Yamamoto and V. Zaveriaev; "*Plasma diagnostics for ITER-FEAT*"; Rev. Sci. Instrum., Vol. 72, No. 1, January 2001.

[25] M. L. Zhang, X. L. Wang, H. L. Xiao, C. M. Wang, J. X. Ran, G. X. Hu; "*Neutron Irradiation Effect in Two-Dimensional Electron Gas of AlGaN/GaN Heterostructures*"; Chin. Phys. Lett. **25**, 1045 (2008).

[26] W. Gu, Y. Hao, L. Yang, C. Duan, H. Duan, J. Zhang and X. Ma; "*The effect of neutron irradiation on the AlGaN/GaN high electron mobility transistors*"; Phys. Status Solidi C **7**, No. **7–8**, 1991 (2010).

Chapter 5

Hall effect sensors for harsh environment

In this Chapter, we report the high temperature and high–energy and high–flux proton irradiation dependences of the electrical and the magnetoelectrical properties of micro–Hall sensors fabricated using AlGaAs/GaAs heterostructures, InAsSb quantum wells and AlGaN/GaN heterostructures. The micro–Hall sensors based on AlGaN/GaN heterostructures are most promising in high temperature and proton fluence up to 10^{14} (protons/cm^2), however the InAsSb quantum wells based micro–Hall sensors can work up to proton fluence 100 folds higher but at temperature lower than 150°C.

5-1 High Temperature Hall sensors

Hall effect sensors are the most widely used magnetic sensors, and are commonly fabricated using narrow band-gap semiconductors such as Si, InAs and InSb. However, these materials based Hall sensors are unstable and inoperable at elevated temperatures due to the onset of intrinsic conduction and physical degradation of the semiconducting materials. Silicon carbide could potentially be used for fabricating Hall sensors operating at high temperature because of its large band gap, high electron saturation velocity, and excellent thermal stability at high temperatures. However, the need for precise control of dopants and the large thickness of the conducting layers of SiC severely limits its sensitivity and stability at high temperatures. The gallium nitride– (GaN) based wide band-gap (3.4eV) semiconductors have high breakdown electric field strength and are robust at elevated temperatures. The high temperature electrical characteristics of AlGaN/GaN heterostructure micro–Hall effect sensors which offer the advantages of wide–band–gap materials that are stable to a least 400°C, as well as an extremely thin 2DEG conduction layer for ultrahigh magnetic sensitivity,

were tested here and compared with AlGaAs/GaAs heterostructure and AlInSb/InAsSb/AlInSb quantum well structure–based Hall devices. The equipment used for the magnetoelectrical characterizations from room temperature to 400°C is shown in Figure 5.1.

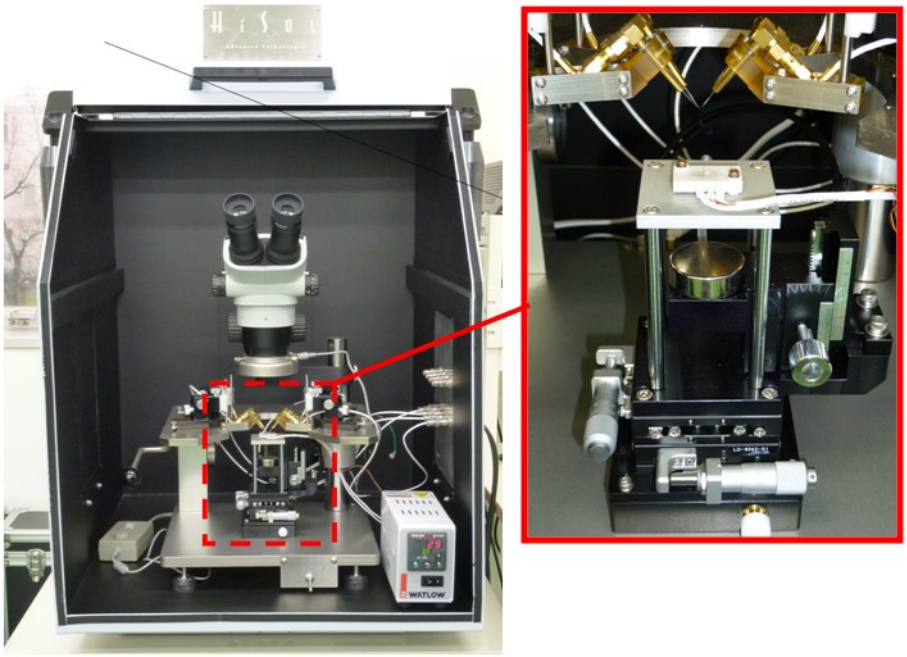

Figure 5.1 Equipment used for the magnetoelectrical characterizations.

5-1-1 AlGaAs/GaAs heterostructures based Hall sensors

a- AlGaAs/GaAs heterostructures

The structure of the AlGaAs/GaAs heterostructure based micro–Hall sensors is shown in Figure 5.2. Two-dimensional electron gas is formed between the InGaAs and the AlGaAs layers. InGaAs was used instead the GaAs. Addition of the undoped AlGaAs between n–AlGaAs and InGaAs reduce the impurity scattering. Electron mobility is about $8\times10^{3}cm^{2}V^{-1}s^{-1}$ at room temperature. The size of the active area of the devices was 5μm ×5μm. The yellow top layer on the active area of the AlGaAs/GaAs heterostructures based micro-Hall sensors shown in Figure 5.2 is deposited for application these sensors for

biosensing application.

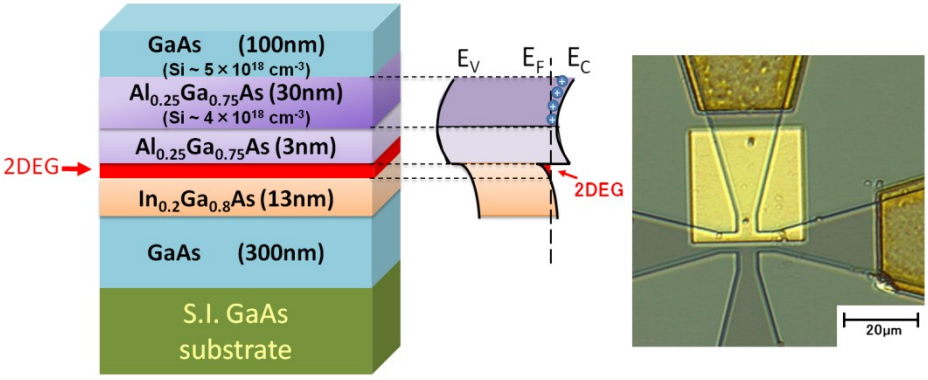

Figure 5.2 Structure of AlGaAs/GaAs heterostructures based micro-Hall sensors.

b- High temperature characterization

The variation of the sheet resistance and the electron mobility are shown in Figure 5.3. The graphs have two behaviors: at temperature low than 150°C the sheet resistance increase and the mobility decreases due to the electron–phonon scattering. When the temperature exceeds the 150°C, the sheet resistance decreases and the electron mobility drops to a value of 65cm^2/Vs at 250°C due to the fast increase of the sheet electron density, as shown in Figure 5.4(a).

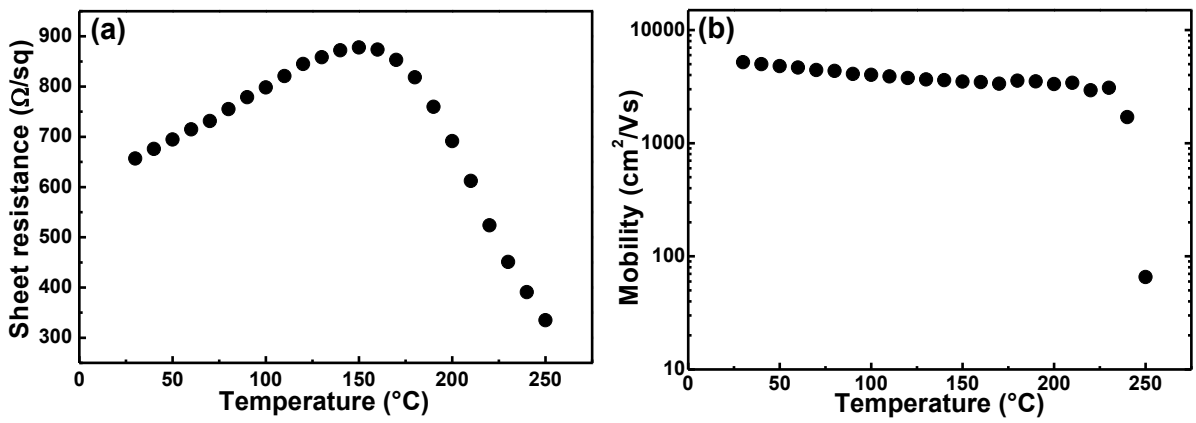

Figure 5.3 Temperature dependence of (a) the sheet resistance and (b) the electron mobility, in AlGaAs/GaAs heterostructures based micro-Hall sensor.

Figure 5.4(a) shows the temperature dependence of the sheet electron density. Fast increase in the sheet electron density, when the temperature exceeds 250°C, caused by thermal activation of electrons to the conduction bands leads to magnetic sensitivity drop at high temperature, as shown in Figure 5.4(b).

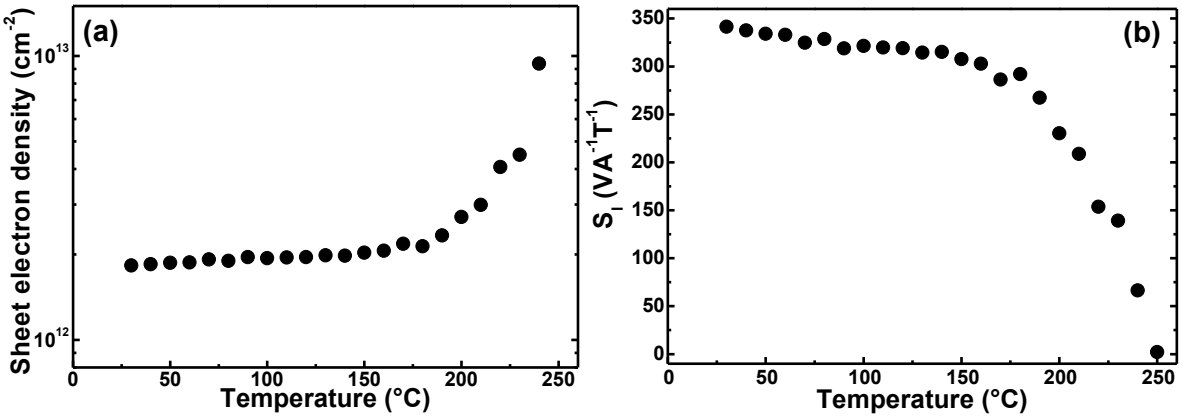

Figure 5.4 Temperature dependence of (a) the sheet electron density and (b) the magnetic sensitivity of AlGaAs/GaAs heterostructures based micro-Hall sensor.

5-1-2 AlInSb/InAsSb/AlInSb quantum well based Hall sensors

a- AlInSb/InAsSb/AlInSb quantum well heterostructures

As shown in Figure 5.5, InAsSb layer of thickness of 100 nm is sandwiched between larger bandgapped AlInSb layers. Layers were grown by molecular beam epitaxy on semiinsulating GaAs (100) substrate. Electrons are confined in the 100 nm InAsSb layer forming a quantum well. Three AlInSb/InAsSb/AlInSb quantum well samples with Sn-doping levels of 5×10^{16}, 7×10^{16} and 10^{17} cm^{-3} referenced by K3875, K3924 and K3960, respectively, were used in this study. The size of the active area of these micro-Hall sensors was 50×50 μm^2.

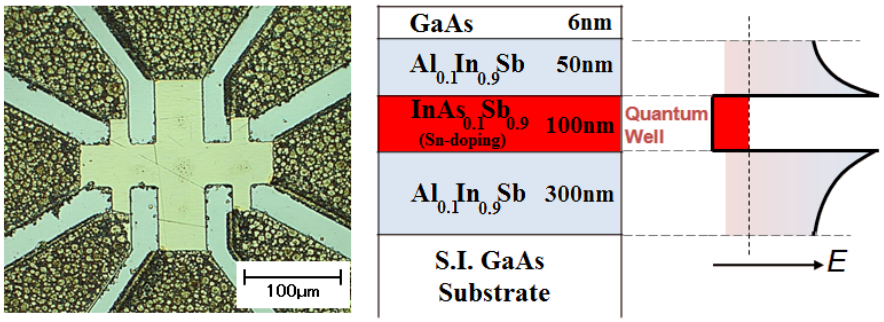

Figure 5.5 Structure of AlInSb/InAsSb/AlInSb quantum well micro-Hall sensors.

b- High temperature characterization

The sheet resistance in the quantum well samples decreases with increasing the temperature, as shown in Figure 5.6(a), due to the sheet carrier increases with increasing temperature, as shown in Figure 5.7(a), caused by the thermal activation of the carriers. Optical phonon scattering is the dominant scattering at high temperature in the InAsSb quantum wells caused the carrier mobility to decrease with increasing the temperature as shown in the Figure 5.6(b). The quantum well with the lower doping exhibits the lower sheet carrier density and the higher carrier mobility in all range of temperature.

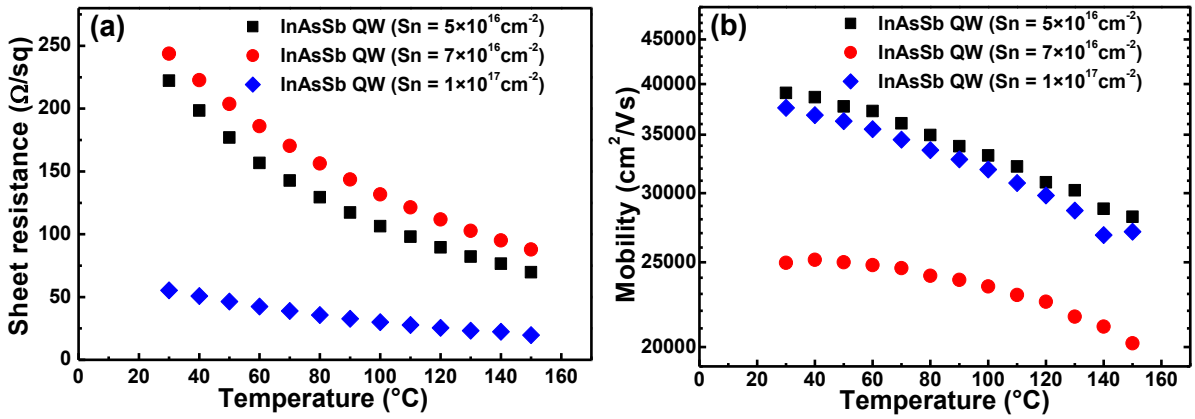

Figure 5.6 Temperature dependence of (a) the sheet resistance and (b) the electron mobility, in InAsSb quantum well based micro-Hall sensor of different doping level.

The magnetic sensitivity, represented in the Figure 5.7(b), and which is inversely proportional

to the sheet carrier density decreases with increasing the temperature in all samples.

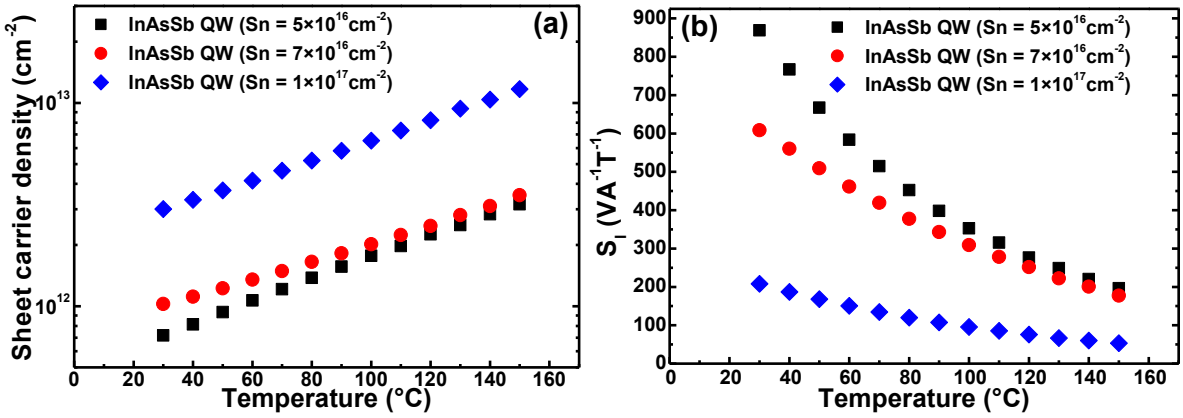

Figure 5.7 Temperature dependence of (a) the sheet electron density and (b) the magnetic sensitivity of InAsSb quantum well based micro-Hall sensor of different doping level.

5-1-3 AlGaN/GaN heterostructures based Hall sensors

a- AlGaN/GaN heterostructures

Figure 5.8 shows the structure of the AlGaN/GaN samples used in this study. The high electron mobility transistor (HEMT) structures were grown by metal organic chemical vapor deposition (MOCVD). Two structures were used: UID–sample where unintentionally doped AlGaN layer was grown on 2 μm GaN layer, as shown in Figure 5.8(a) and Si–doped sample where the structure consists of 2 μm undoped GaN buffer layer and a 25 nm AlGaN barrier layer doped with Si to 4×10^{18} cm^{-3} sandwiched between two undoped AlGaN layers as shown in Figure 5.8(b).

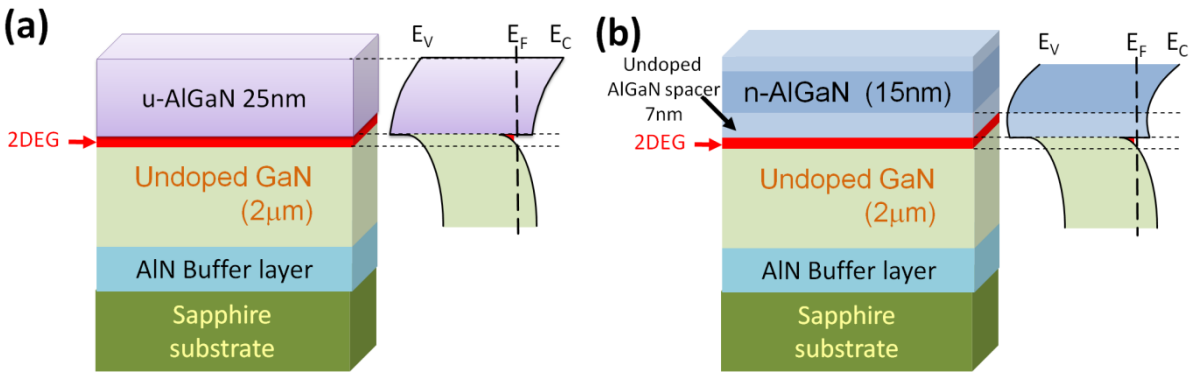

Figure 5.8 Structure of $Al_xGa_{1-x}N$/GaN micro-Hall sensors.

b- High temperature characterization

The variation of the sheet resistances of the UID– and the Si–doped micro-Hall sensors as function of the temperature are shown in Figure 5.9(a). The samples have active area of 5×5 μm^2. The sheet resistance (R_{sh}) increased with increasing temperature according to the power-law equation (5.1) with power indices of –2.45 and –2.44 for UID– and the Si–doped samples, respectively. The values of the power indices are consistent with those reported by Liu *et al*. [1] and imply that the predominant scattering was optical phonon scattering.

$$R_{sh} = R_{sh0}\left(\frac{T_0}{T}\right)^{\gamma} = \frac{1}{qN_s}\left[\mu_0\left(\frac{T}{T_0}\right)^{\gamma}\right]^{-1} \tag{5.1}$$

where R_{sh0} and μ_0 are the value of R_{sh} and μ at T=300°K and γ is the power index.

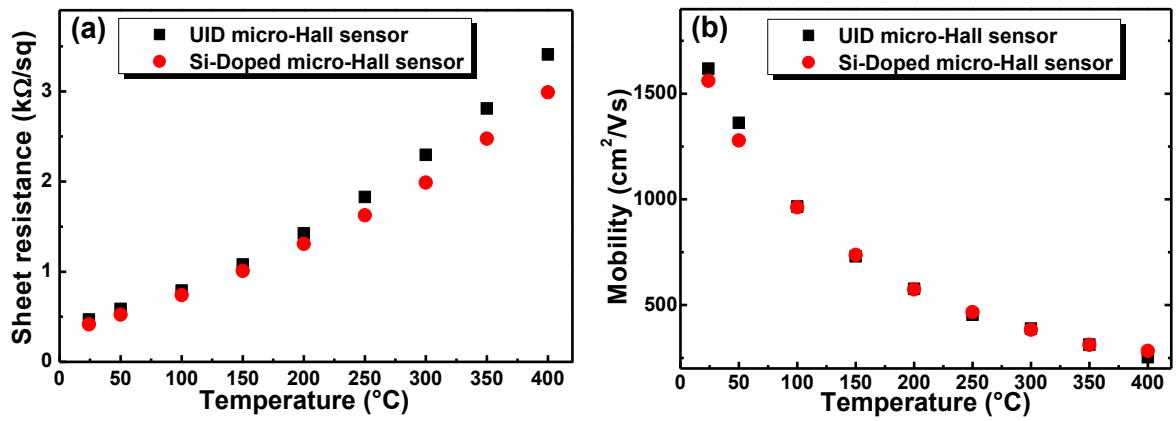

Figure 5.9 Temperature dependence of (a) the sheet resistance and (b) the electron mobility, in AlGaN/GaN heterostructures based micro–Hall sensors.

The electron mobility, shown in Figure 5.9(b), was about 1620 and 1560 ($cm^2V^{-1}s^{-1}$) at room temperature in UID– and the Si–doped samples, respectively. The mobility decreases with increasing temperature in both samples, due to the optical phonon scattering. The Si–doped micro–Hall sensor has lower electron mobility due to higher electron density as shown in Figure 5.10(a). The electron mobility was about 250 and 280 ($cm^2V^{-1}s^{-1}$) at 400°C in UID and the Si-Doped samples, respectively, translating the faster decrease of the electron mobility in the UID– micro–Hall sensor. This behavior was explained by the increase of the residual carriers in the background at high temperature, which affect the electron mobility. The background carriers have a severe effect in the sample of lower electron density [2].

The sheet electron density in both UID– and the Si–doped micro–Hall sensors slightly decrease with increasing temperature probably due to the reduction in the polarization (probably both spontaneous and piezoelectric) charge caused by the lattice expansion with the increase in temperature [3]. Due to slight variation in the sheet electron density, the magnetic sensitivity, shown in Figure 5.10(b), was almost stable between room temperature and 400°C.

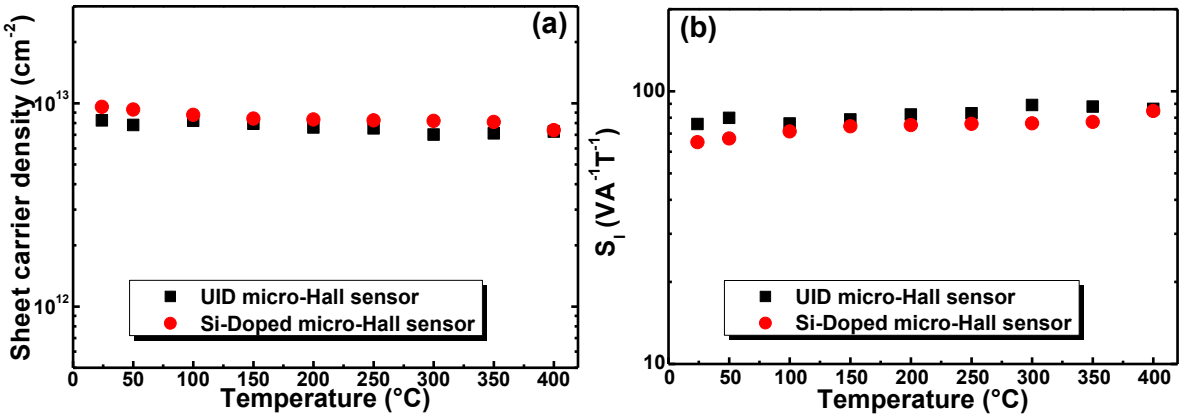

Figure 5.10 Temperature dependence of (a) the sheet electron density and (b) the magnetic sensitivity of AlGaN/GaN heterostructures based micro–Hall sensors.

c- Size dependence magnetoelectrical characterizations

The magnetoelectrical properties of AlGaN/GaN based micro–Hall sensors of structure shown in Figure 5.8(a) and with different mesa size, as shown in Figure 5.11, were studied.

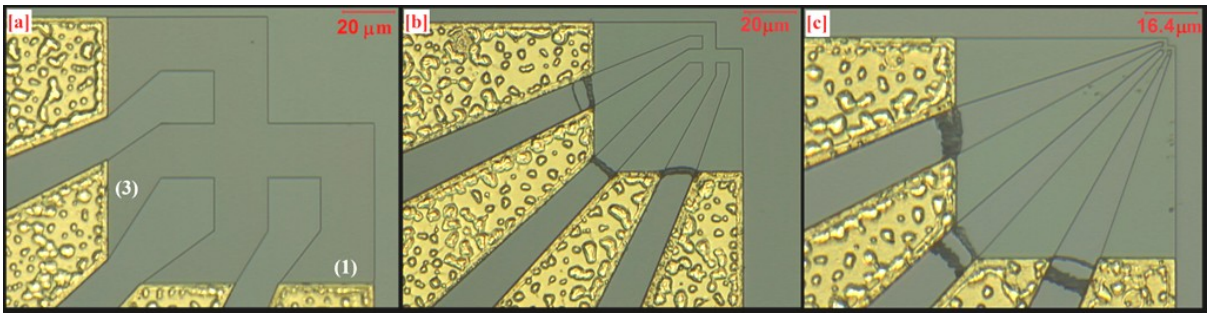

Figure 5.11 AlGaN/GaN micro–Hall sensors with active area of (a) 20×20µm^2, (b) 5×5µm^2 and (c) 1×1µm^2.

Figure 5.12 represents the temperature dependence of the series resistance of the three samples measured using Keitheley 2000 Multimeter between (1) and (3) shown in Figure 5.11(a). The series resistance is found to follow the sheet resistance curve shape multiplied by geometric factor, in the case of the active area 1×1µm^2 this factor was equal to about 26; 15 in the case of mesa of 5×5µm^2 sample and about 6.5 for 20×20µm^2.

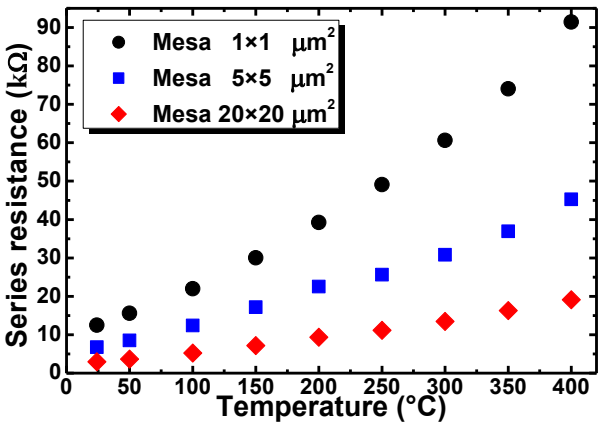

Figure 5.11 Temperature dependence of the series resistance of AlGaN/GaN micro–Hall sensor of different mesa sizes.

The series resistance was fitted according to the Callendar–Van Dusen equation given by:

$$R = R_0(1 + AT + BT^2) \tag{5.2}$$

Where R_0 is the temperature at 0°C, A and B are parameters and T is the temperature in celcius (°C). A and B are deduced from the fitting of the series resistance and resumed in Table 5.1.

RTD is analyzing resistance temperature detectors made of platinum above 0°C. The temperature sensitivity shown in Table 5.1 is measured according to the following equation [4]:

$$dR/R_0 dT = A + 2BT \tag{5.3}$$

The AlGaN/GaN heterostructures temperature sensitivity was higher in the sensor with active area of 20×20μm^2 and exceeds the values reported in the reference [4]. Our sample's temperature sensitivity was three times higher, near room temperature, than the temperature sensitivity of conventional RTD sensors and was seven times higher at temperature of 400°C.

Table 5.1 Fitting parameters for the series resistance of AlGaN/GaN micro–Hall sensors.

Samples	$\mathbf{R = R_0(1 + AT + BT^2)}$			**Sensitivity**	
	$\mathbf{R_0(k\Omega)}$	**A**	**B**	**RT**	**400°C**
AlGaN/GaN [1×1μm^2]	10.94	0.0071	2.74×10^{-5}	0.0084	0.0290
AlGaN/GaN [5×5μm^2]	5.49	0.0110	1.66×10^{-5}	0.0118	0.0243
AlGaN/GaN [20×20μm^2]	2.3	0.0113	1.73×10^{-5}	0.0121	0.0251
RTD	0.1	0.0039	-5.8×10^{-7}	0.0038	0.0034

The absolute magnetic sensitivity was stable in the three samples as shown in Figure 5.13. The sample with higher mesa size showed better linearity of the absolute magnetic sensitivity due to its lowest offset voltage as shown in Figure 5.14.

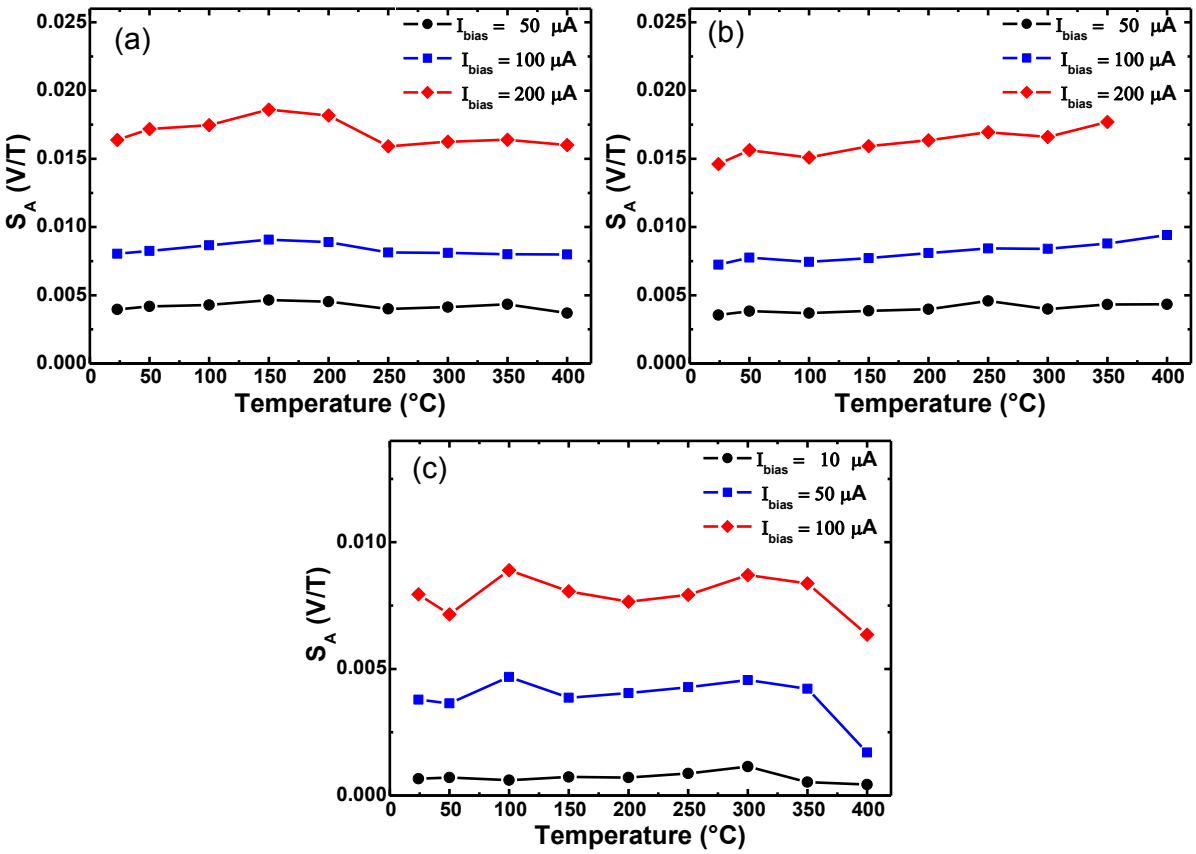

Figure 5.13 Temperature dependence of the magnetic sensibility of AlGaN/GaN micro–Hall sensors with active area of (a) 20×20μm^2, (b) 5×5μm^2 and (c) 1×1μm^2.

The offset voltage increases with increasing the temperature and the bias current. The offset voltage was higher in the sample of active area of 1×1μm^2 due to its high series resistance.

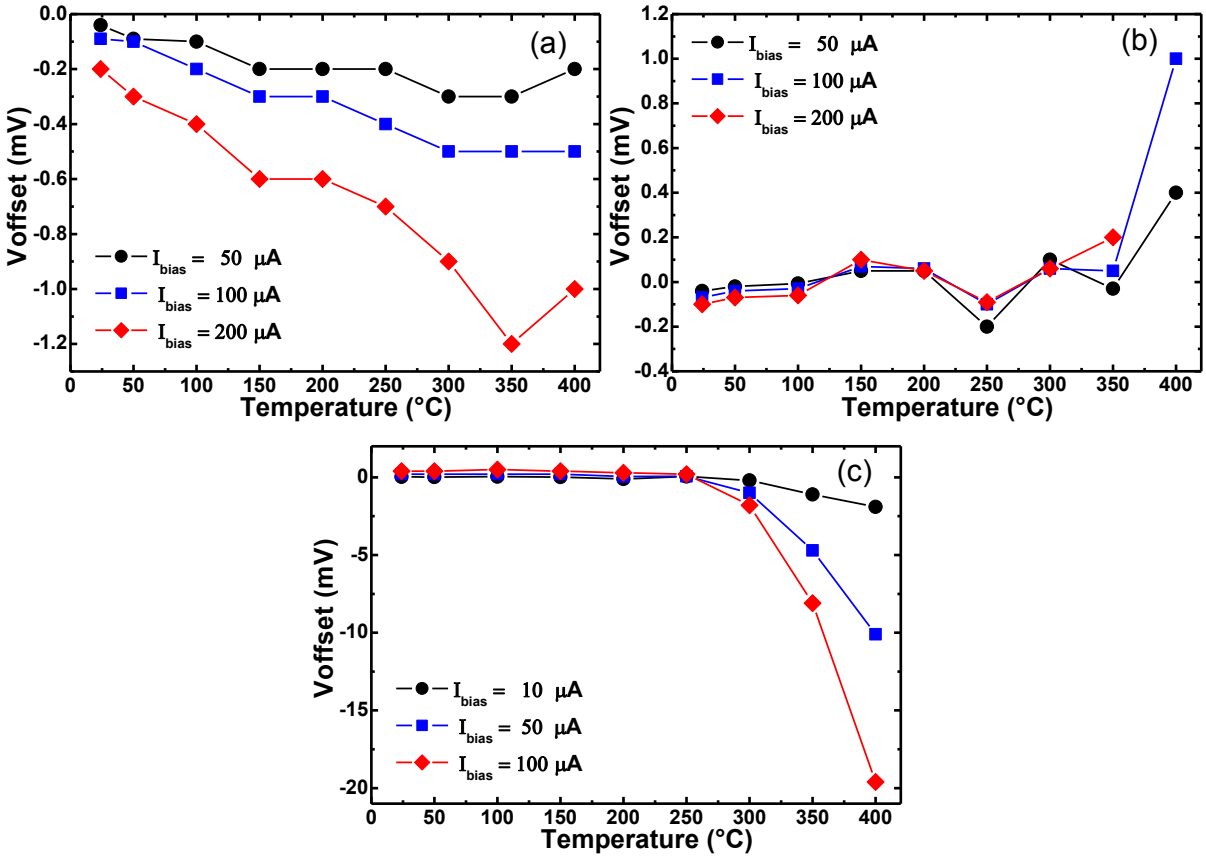

Figure 5.14 Temperature dependence of the offset voltage of AlGaN/GaN micro–Hall sensors with active area of (a) 20×20μm^2, (b) 5×5μm^2 and (c) 1×1μm^2.

To eliminate the offset voltage the spinning current method was used. The bias current is switched in four directions, for each direction, the voltage perpendicular to current is measured. The residual offset voltage after applying this method for each sample is shown in Figures 5.15. The black plots in Figure 5.15 correspond to the spinning current method with taking into account the direction of the magnetic field, positive and negative magnetic field (eight measurements as described in Chapter 2). The residual offset voltage was minimal using the second method.

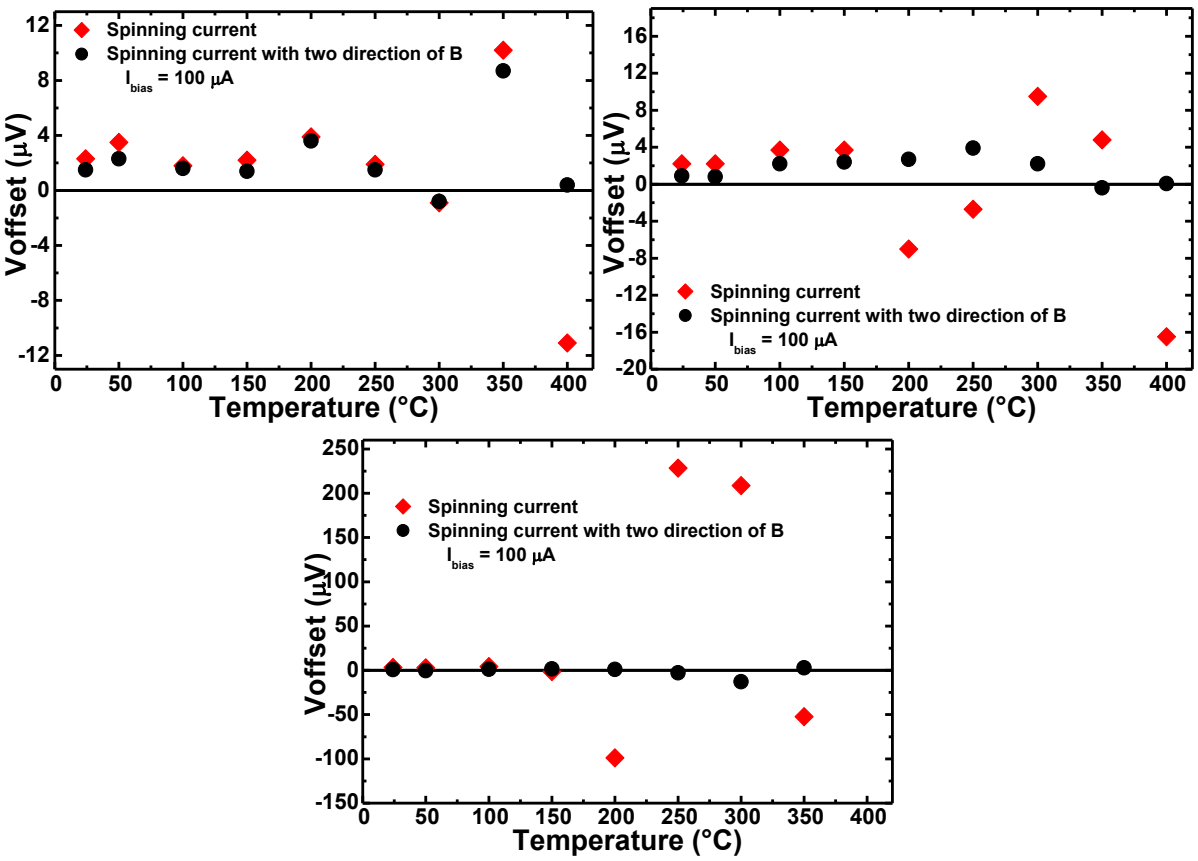

Figure 5.15 Temperature dependence of the residual offset voltage of AlGaN/GaN micro–Hall sensors with active area of (a) 20×20μm^2, (b) 5×5μm^2 and (c) 1×1μm^2.

The current and temperature dependences of the resolution of our micro–Hall sensors are shown in Figure 5.16. The sample with active area of 20×20μm^2 showed the lowest detectable magnetic field B_{min} (i.e., the highest magnetic resolution) and the sample with smallest active area size (1×1μm^2) showed the lowest resolution due to its high series resistance.

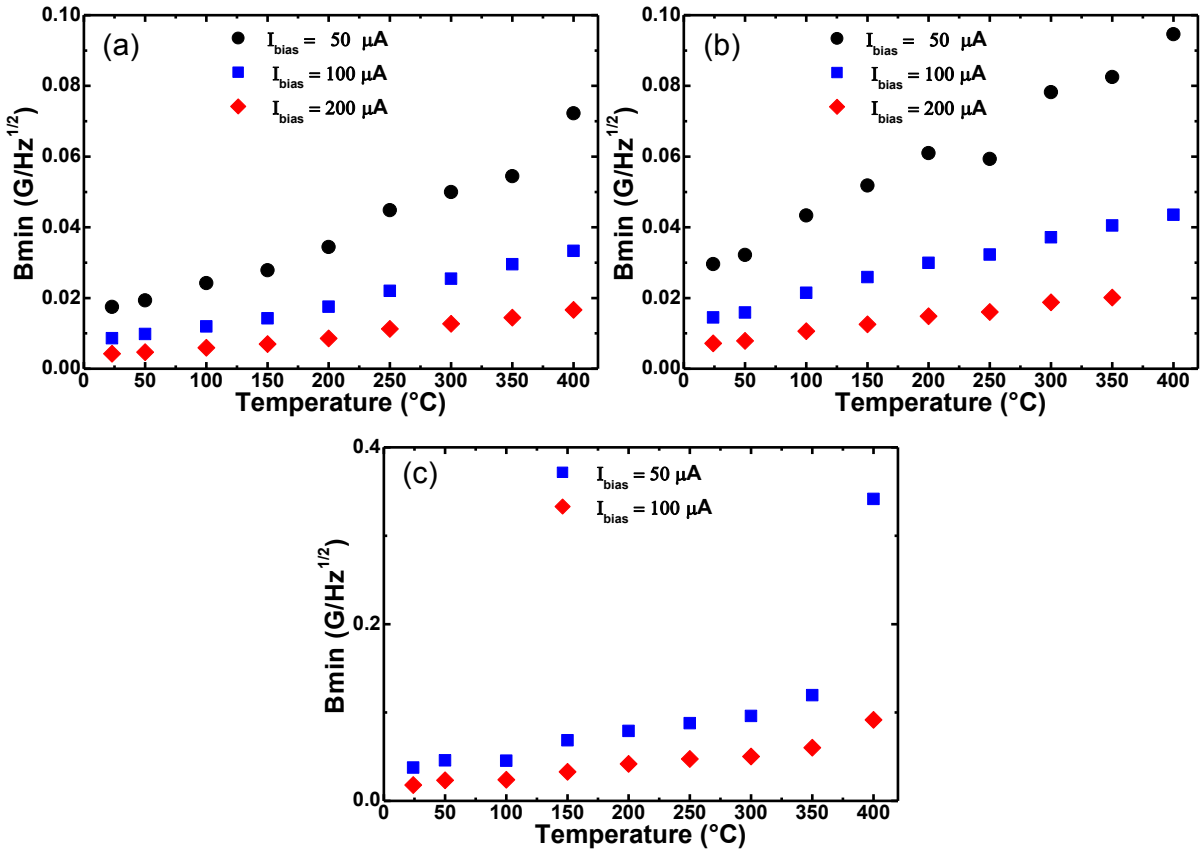

Figure 5.16 Temperature dependence of the minimum magnetic field of AlGaN/GaN micro–Hall sensors with active area of (a) 20×20μm^2, (b) 5×5μm^2 and (c) 1×1μm^2.

5-1-4 AlGaN/GaN versus GaAs and InAsSb based micro–Hall sensors

Figure 5.17 shows a comparison of the sensitivity of AlGaN/GaN, AlGaAs/GaAs and InAsSb QW micro-Hall sensors with respect to temperature. The AlGaN/GaN micro–Hall sensors operate up to 400°C with an SCRS of 67 VA^{-1}T^{-1}, whereas sensors fabricated using the narrower band–gap sensors degrade from ~150°C. The AlGaAs/GaAs Hall sensors showed a relatively high SCRS and were stable up to ~200°C, after which the devices failed. The sensitivity of AlInSb/InAsSb/AlInSb QW Hall sensors at room temperature was high, at 2540 VA^{-1}T^{-1}.

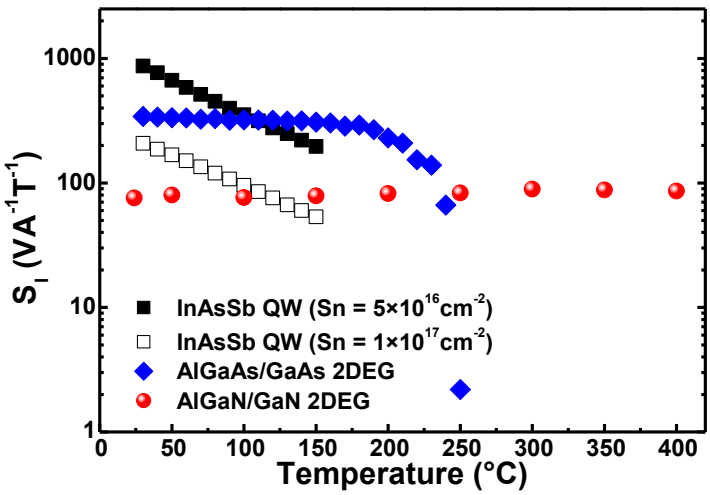

Figure 5.17 Temperature dependence of the magnetic sensitivity.

5-1-5 Two-dimensional materials based Hall sensors

Recently, researchers interest in the two-dimensional (2D) materials because of their potential for a wide range of electronic devices. In general, the higher the mobility of the semiconductor used, and the thinner the active region, the better the Hall device, making the 2D materials good candidates as new generation of Hall sensors.

a- Metal/Molybdenum–dichalcogenide based Hall sensors fabrication

We fabricated four-terminal devices (Ti/ $MoSe_2$, Ti/ MoS_2 and Ti/ Au/ $MoSe_2$), based on molybdenum diselenide ($MoSe_2$) and molybdenum disulphide (MoS_2). For the fabrication process we used 50 nm titanium (Ti) electrodes deposited by electron-beam evaporation at room temperature, for the fabrication of Ti/ $MoSe_2$ and Ti/ MoS_2 devices, and 30 nm titanium (Ti) followed by deposition of 100 nm gold (Au) electrodes, for the fabrication of Ti/ Au/ $MoSe_2$ devices.

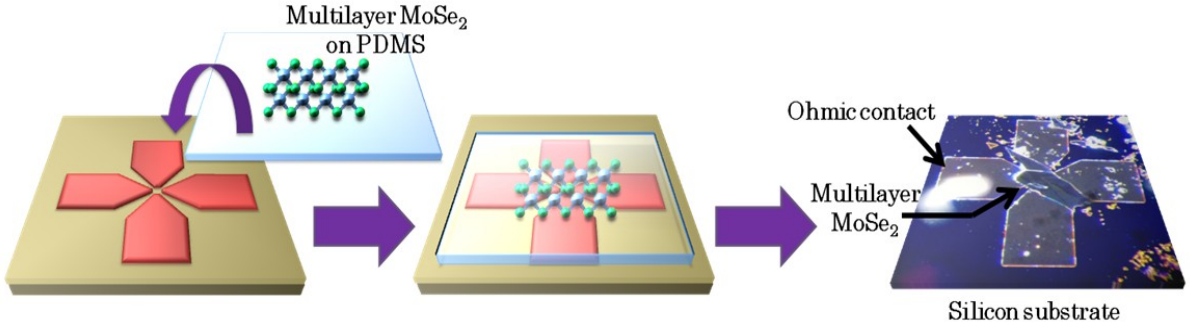

Figure 5.18 Schema of the $MoSe_2$ Multilayer transfer on the Hall sensor electrodes.

The electrodes were deposited on silicon substrates (doped p^+, conductivity: 0.003–0.007 Ωcm) covered with 300 nm of thermally oxidized silicon dioxide (SiO_2). We transferred few-layered flakes of natural $MoSe_2$ (HQgraphene, Netherlands) and MoS_2 onto Ti electrodes using PDMS (Dow Corning, Toray Co., Ltd) by mechanical exfoliation, as shown in Figure 5.18. Finally, the Ti/ $MoSe_2$ and the Ti/ MoS_2 devices were annealed at 400°C under H_2+Ar gas atmosphere for two hours.

b- Magnetoelectrical characterizations of the $MoSe_2$ based Hall sensors

The current–voltage characteristics of the Hall sensors based on $MoSe_2$ and MoS_2 are shown in Figure 5.19. The Ti/$MoSe_2$ and Ti/Au/$MoSe_2$ structures showed higher saturation current, and best linearity and symmetry in the current voltage characteristics, as shown in Figure 5.19(a) and Figure 5.19(a), compared with the Ti/MoS_2 structure that showed Schottky contact behavior as shown in the inset of Figure 5.19(c). The Schottky contact is due to the pinning of the Fermi level at the conduction band in the MoS_2, according to the literature. Improvement by three orders in the saturation current was observed in both devices Ti/$MoSe_2$ and Ti/Au/$MoSe_2$ due to contact/flake contact enhancement by annealing.

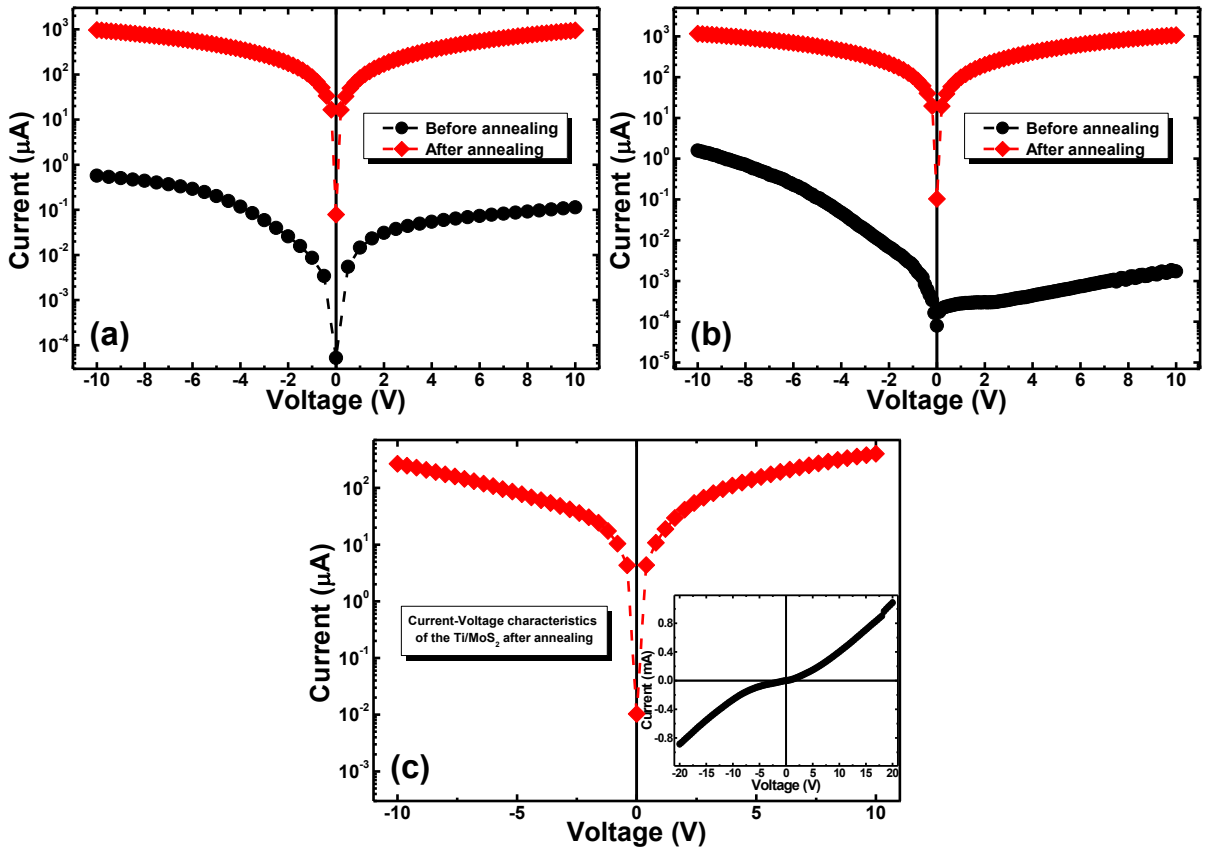

Figure 5.19 Current voltage characteristics of the (a) Ti/$MoSe_2$ and (b) Ti/Au/$MoSe_2$ before and after annealing; and (c) Ti/$MoSe_2$ before annealing, the inset shows the Schottky behavior of the current.

The electrical properties of the devices such as sheet resistance, mobility, and sheet carrier density were calculated using Hall effect measurement, the results are shown in Table 5.2.

Table 5.2 The electrical properties of the multilayer $MoSe_2$ based Hall sensor.

	Ti/$MoSe_2$	**Ti/Au/$MoSe_2$**
Sheet resistance (kΩ/□)	3.93	9.01
Series resistance (kΩ)	9.98	18.05
Sheet carrier density (cm^{-2})	4.24×10^{13}	2.02×10^{13}
Mobility (cm^2/Vs)	37.7	34.3

Figure 5.20 (a) and (b) show the current and the magnetic field dependence of the Hall voltage in the Ti/$MoSe_2$ and Ti/Au/$MoSe_2$, showed high magnetic sensitivity, as shown in the inset of Figure 5.20(b), due to its lower sheet carrier density but bad linearity of the Hall voltage due to its high offset voltage as represented in the inset of Figure 5.21(b). The magnetic sensitivity were about 10 and 60 $VA^{-1}T^{-1}$ in Ti/$MoSe_2$ and Ti/Au/$MoSe_2$ Hall sensors, respectively. The minimum detectable magnetic field of both Hall sensors Ti/$MoSe_2$ and Ti/Au/$MoSe_2$ is shown in Figure 5.21(a) and Figure 5.21(b), respectively.

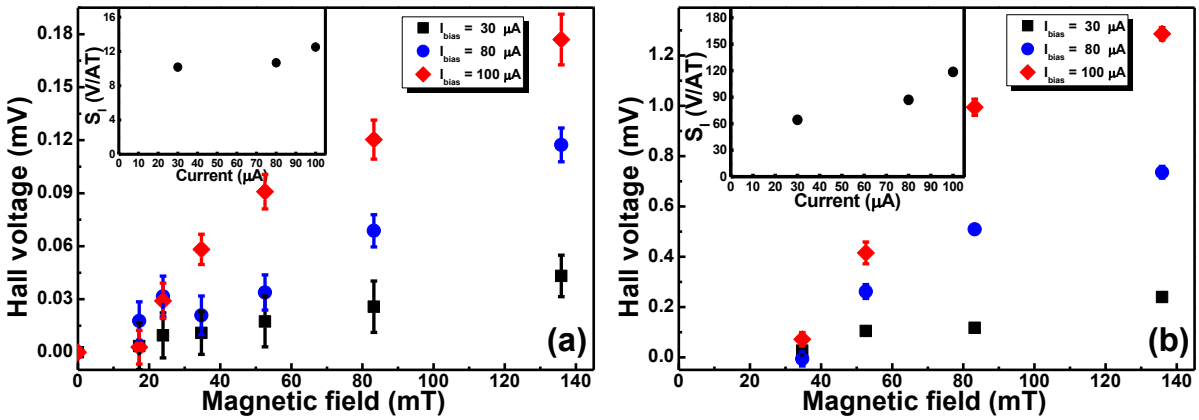

Figure 5.20 Hall voltage versus the magnetic field measured at different values of the current in the (a) Ti/$MoSe_2$ and (b) Ti/Au/$MoSe_2$. Insets: show the related magnetic sensitivity.

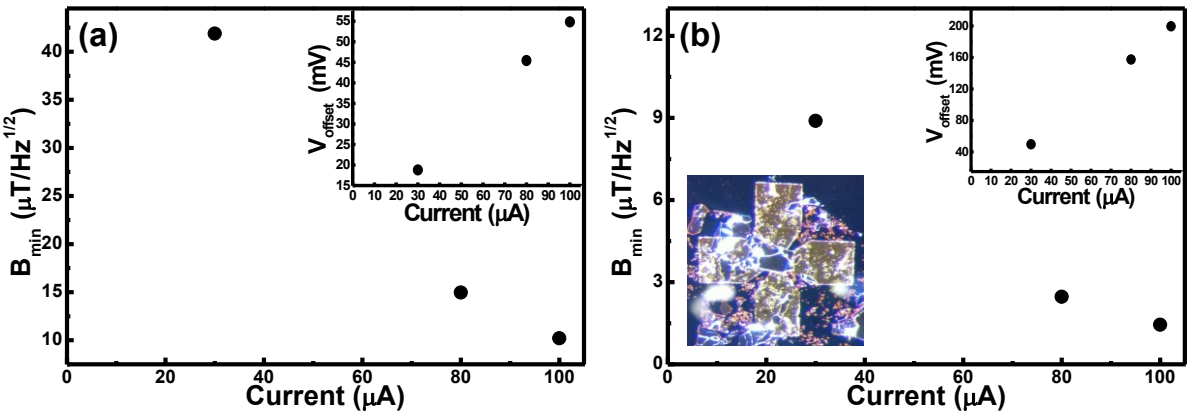

Figure 5.21 The minimum detectable magnetic field versus the current in the (a) Ti/$MoSe_2$ and (b) Ti/Au/$MoSe_2$. Insets: show the related magnetic sensitivity. Insets: show the current dependence of the offset voltages.

5-2 High proton energy irradiation effect on Hall sensors

Hall sensors based on materials of high displacement energy are suitable for harsh environment. As shown in Table 4.1, GaN and SiC materials are more suitable for high-energy irradiation environment. The high electron density in GaN based 2DEG heterostructures, in addition to the GaN high displacement energy, enhances their resistance against irradiation, as we will see later. Zinc oxide (ZnO) has higher displacement threshold energy (50eV for Zn atoms and 55eV for O atoms) [5] and therefore high resistance against the irradiation. In addition, MgZnO/ZnO 2DEG heterostructures may have better resistance to its higher electron density compared with bulk ZnO, however, their low mobility, compared with AlGaN/GaN heterostructures as example, may limits their employment for harsh environment applications.

In this part, we discuss our magnetoelectrical properties results of the AlGaN/GaN heterostructures and InAsSb quantum well based micro-Hall sensors against the proton irradiation.

5-2-1 Proton implantation system

Ion-implantation facility at Takasaki Ion Accelerators for Advanced Radiation Application (TIARA), JAEA was used for proton irradiation. The samples were placed in a vacuum chamber and irradiated with a range of proton doses. Using Stopping and Range of Ions in Matter (SRIM) simulations for calculation of the proton projection range, 98% of the implanted protons at 380 keV penetrated to a distance of 2.99 μm through the InAsSb quantum well heterostructures and to a distance of 3.96 μm through the heterostructures AlGaN/GaN.

5-2-2 Proton implantation in AlGaN/GaN heterostructures based micro-Hall sensors

a- Magnetoelectric characterizations

The AlGaN/GaN heterostructures based micro–Hall sensors, the UID– and Si–doped micro–Hall sensors, were irradiated with proton energy of 380keV and with proton fluence which varies between 10^{11} and 10^{16} (protons/cm^2).

As shown in Figure 5.22 (a) the absolute sensitivity (S_A) of the sample irradiated by 10^{14} protons/cm^2 at different drive current values was almost stable. The sheet electron density (N_s) decreased slightly after irradiation, as shown in Figure 5.24, which explains the stability of the absolute sensitivity since it is related to the sheet electron density according to the equation $S_A = I/qN_S$.

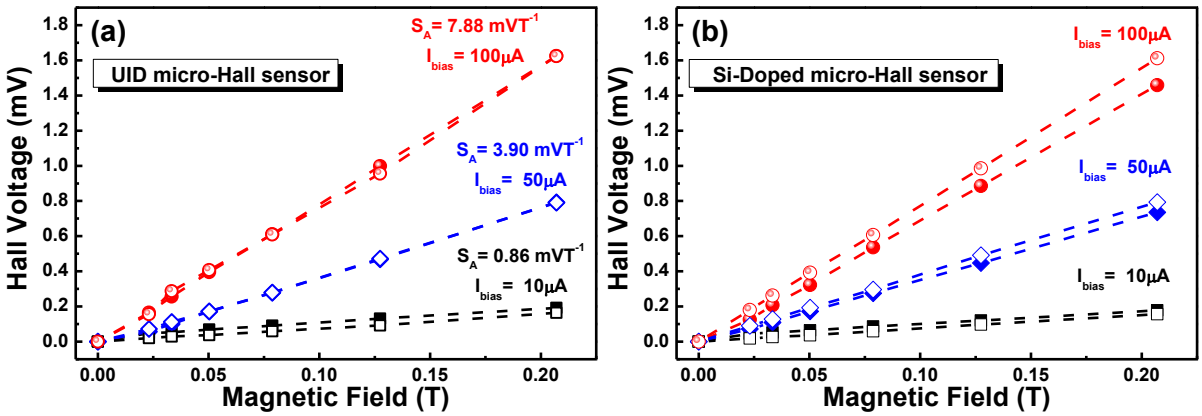

Figure 5.22 Variation of Hall voltage versus magnetic field, and magnetic sensitivity of the micro-Hall sensor versus drive current, the filled shapes belong to sample before irradiation and hollow shapes to sample irradiation with 10^{14} (protons/cm^2) proton fluence.

The variation of the sheet resistances of the UID– and the Si–Doped micro–Hall sensors as function of proton fluence are shown in Figure 5.23(a). The sheet resistance was found to increase with increasing the proton fluences, which suggests the generation of crystalline damage into the AlGaN/GaN heterostructure.

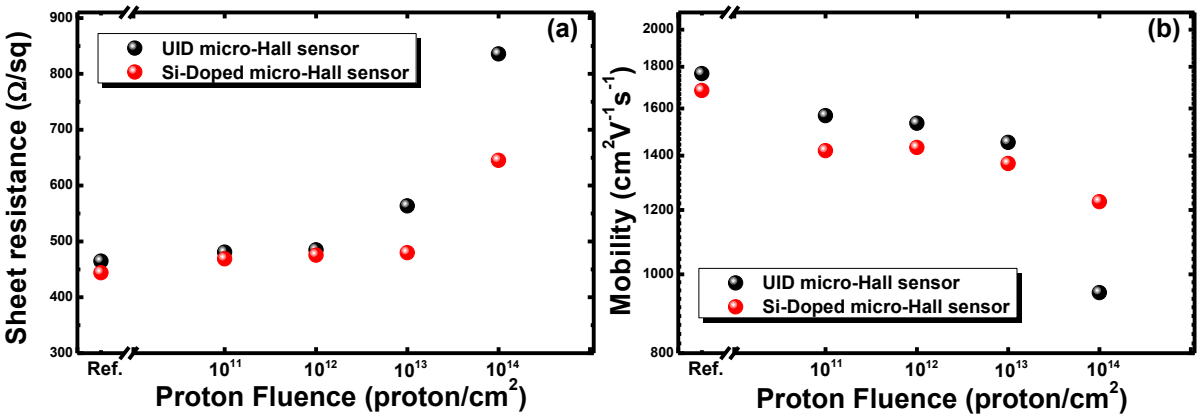

Figure 5.23 Proton fluence dependence of (a) the sheet resistance and (b) the electron mobility, in AlGaN/GaN heterostructures based micro-Hall sensors.

A marked increase of sheet resistance was found above fluence of 10^{14} cm^{-2}. It was not possible to measure the electrical characteristics of samples irradiated with 10^{15} and 10^{16} cm^{-2} because they exhibited extremely high resistance. The sheet resistance increased more in the UID– sample than in the Si–doped sample because of its slight low sheet electron density compared with the Si–doped sample. Figure 5.23(b) shows the variation of the 2DEG electron mobility with proton dose. The electron mobility gradually decreased with increasing proton dose.

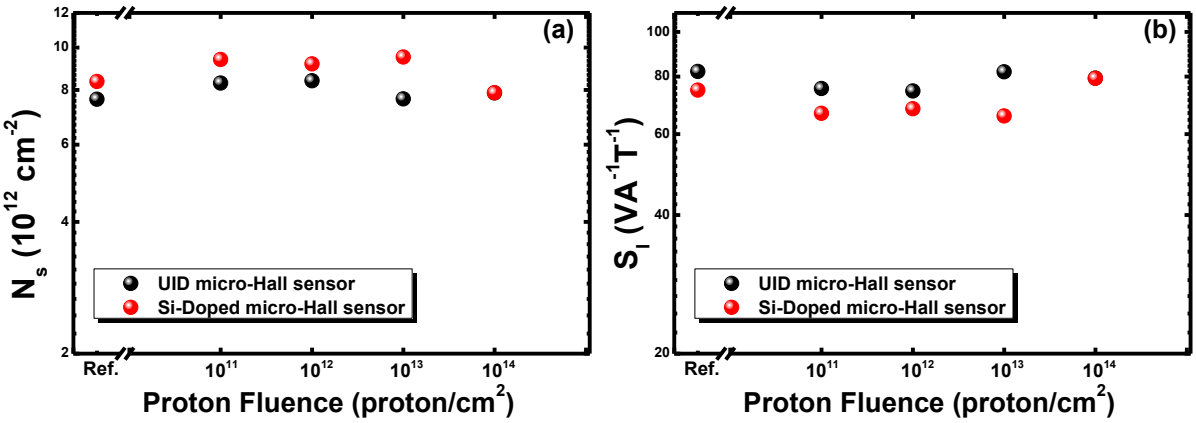

Figure 5. 24 Proton fluence dependence of (a) the sheet electron density and (b) the magnetic sensitivity, in AlGaN/GaN heterostructures based micro-Hall sensors.

Slight increase in the sheet electron density was observed when the proton fluence varies between 10^{11} and 10^{13} (protons/cm^2) and a decreased close to the initial value at 10^{14} (proton/cm^2), as shown in Figure 5.24(a). This behavior depends on the nature of defects created near the 2DEG (nitrogen or gallium defects). Creation of nitrogen vacancies doped the GaN n–type and it can enhance the 2DEG electron density. Polyakov et al. [6] report the same behavior in the neutron irradiated AlGaN/GaN heterostructures, the increases in the 2DEG electron density at low dose was explained by the introduction of shallow centers in the AlGaN layer and which act as modulation doping. The magnetic sensitivity was almost unchanged as shown in Figure 5.24(b) due to the slight variation of the sheet electron density after proton irradiation.

b- X-ray diffraction characterization

The effects of proton irradiation on the crystallinity of AlGaN/GaN heterostructures were examined by X–ray diffraction (XRD) measurements as shown in the in 2θ–ω scan in Figure 5.25. The results show the XRD peaks of the reference and the 10^{14} cm^{-2} dose proton samples, which are, assigned as XRD peaks from the GaN layer based on the diffraction angles. These results showed that the XRD peaks remained after irradiation with a dose of 10^{14} cm^{-2}. It should be noted that an additional shoulder in lower angle side of irradiated sample was observed. A similar shoulder was reported after 2 MeV irradiation by Sonia et al [7], and attributed to the generation of interstitial defects in the heterostructure. Although our XRD results suggest the generation of proton irradiation effects in our AlGaN/GaN structures, it is difficult to directly connect the XRD results with the electrical characteristics because the electrical characteristics are sensitive to the 2DEG region, whereas the XRD signal is from whole of the sample.

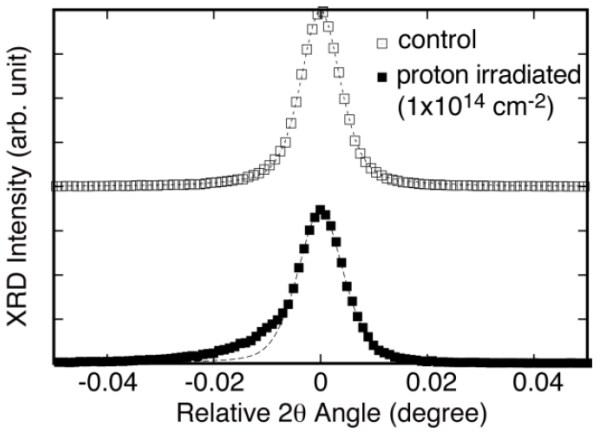

Figure 5. 25 X-ray diffraction spectrum in 2θ-ω scan of reference and proton irradiated samples. Dashed lines are based-on pseudo Voigt functions.

c- Low temperature characterization

The magnetoresistance measurements were performed in a cryogenic liquid helium cryostat from 1.6 to 300K with magnetic fields of up to 10 T produced by a superconductor magnet, the equipment is shown in Figure 5.26. The electrical characterizations were performed using a B1500A semiconductor device analyzer.

Figure 5. 26 Cryogenic liquid helium cryostat from 1.6 to 300K.

Figure 5.27 shows the Hall resistance and the magetoresistance at 4K and using current drive of 20μA of the unirradiated AlGaN/GaN heterostructures based micro-Hall sensors.

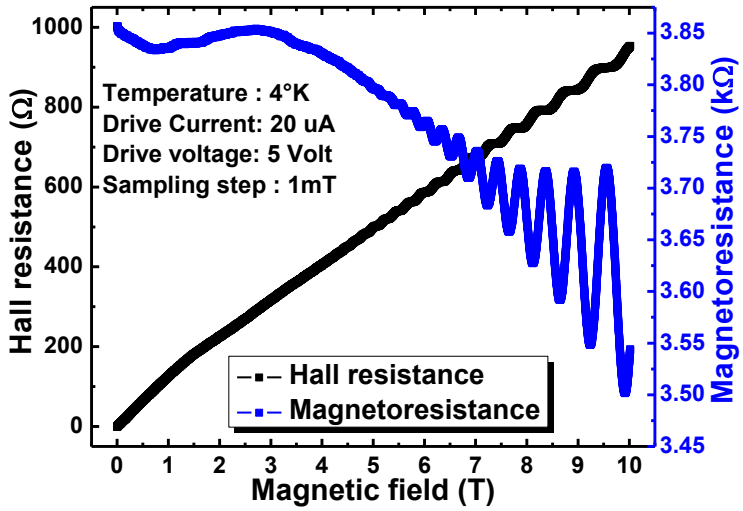

Figure 5. 27 The Hall resistance and the magetoresistance at 4K and using current drive of 20μA of the unirradiated AlGaN/GaN heterostructures based micro-Hall sensors.

The magnetoresistance showed three behaviors: Weak localization at very low magnetic field, electron–electron interaction, and Shubnikov de Haas oscillations begin at around 4T.

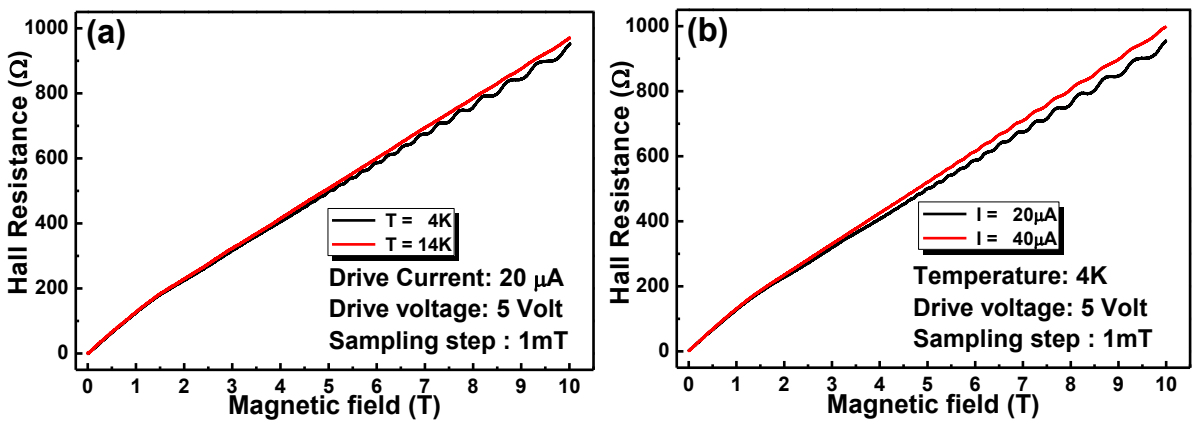

Figure 5.28 Quantum Hall resistances as a function of magnetic field at (a) two values of temperature and current fixed to 20μA and (b) two values of current and temperature fixed to 4K, in AlGaN/GaN micro–Hall sensors.

The decrease of the minima in the oscillations indicates the absence of parallel conduction. The sample showed clear landau levels started at 5T, and which started to disappear at 14K, as shown in Figure 5.28(a).

The temperature and the current dependences of the quantum Hall resistance in the unirradiated AlGaN/GaN heterostructures based micro-Hall sensors are shown in Figure 5.28. The disappearance of the Landau plateaus corresponds to electron heating phenomenon [8].

A linear dependence of the magnetoresistance as function of square of the magnetic field, as shown in Figure 5.29, was observed in the unirradiated AlGaN/GaN heterostructures based micro–Hall sensor, which corresponds to electron–electron interaction according to the equation (5.4):

$$\rho_{xx} \approx \rho_0 - \rho_0^2(1 - \mu^2 B^2)\, \delta\sigma_{xx}^{ee}(T) \tag{5.4}$$

where ρ_{xx} represent the magnetoresistivity, ρ_0 is the resistivity at zero magnetic field, μ is the mobility and $\delta\sigma^{ee}(T)$ is the correction term due to electron–electron interaction at different temperatures.

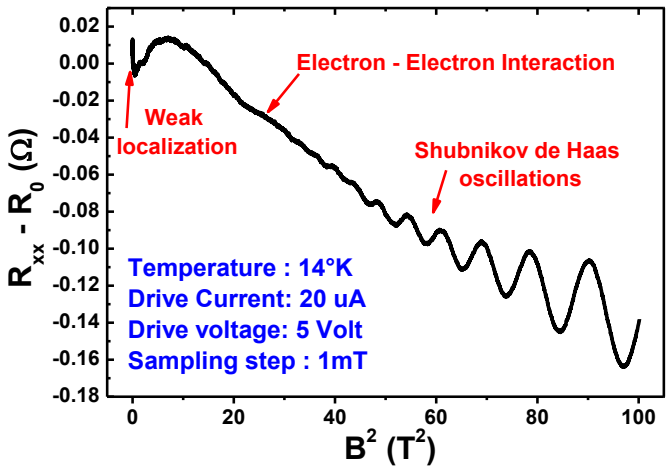

Figure 5.29 The magnetoresistance versus square of the magnetic field in the unirradiated sample.

Temperature–dependent SdH oscillations are shown in the Figure 5.30 for the non–irradiated

sample. The oscillations became more pronounced at higher magnetic fields and tended to damp with increasing the temperature. The oscillating portion of the magnetoresistance can be expressed as:

$$\frac{1}{2}\frac{\Delta R_{xx}}{R_0} = 2\frac{\chi}{\sinh(\chi)}\exp\left(\frac{-\pi}{\omega_c\tau_q}\right)\cos\left(\frac{2\pi\Delta E}{\hbar\omega_c} - \pi\right) \tag{5.5}$$

where $\omega_c = eB/m^*$ is the cyclotron frequency, m^* the effective mass at the Fermi level, τ_q the quantum scattering time, $\chi = 2\pi^2 k_B T/\hbar\omega_c$.

We determined the effective mass from the temperature dependence of the oscillating component amplitude, shown in the inset of Figure 5.30 at a fixed magnetic field. The amplitude A of the SdH can be given by:

$$ln\left(\frac{A}{T}\right) = C - \frac{2\pi^2 k_B m^*}{e\hbar B}T \tag{5.6}$$

where C is a temperature independent term, by plotting ln(A/T) versus T we deduce directly the effective mass from the slope which is equal to $2\pi^2 k_B m^*/e\hbar B$. In order to obtain the quantum scattering we plot the equation:

$$\ln\left(\frac{1}{4}\frac{\Delta R\sinh(\chi)}{R_0\chi}\right) = C - \frac{\pi m^*}{e\tau_q}\frac{1}{B} \tag{5.7}$$

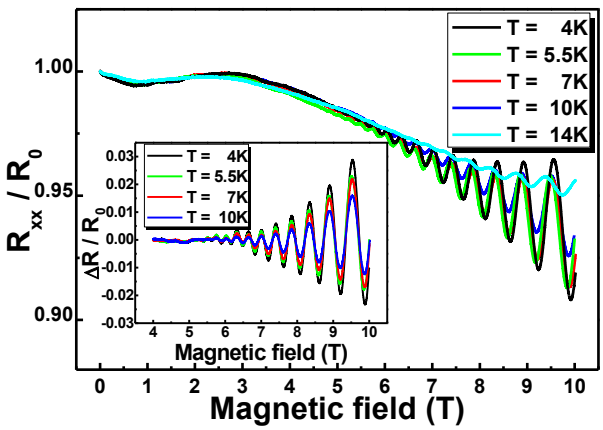

Figure 5.28 Shubnikov de Haas oscillations at different temperature values. The inset shows oscillating component of the magnetoresistance.

The effective mass of the sample before irradiation is approximately 0.20 m_e at 6.3 Tesla.

And the quantum scattering time equal to 63.8fs a value close to those reported before [9,10]. The classical scattering time τ_c is experimentally determined from the mobility using the equation $\mu = e\tau_c/m^*$ and it is approximately equal to 1,38ps. The ratio τ_c/τ_q provides information about the dominant elastic scattering process.

The Van der Pauw measurements were carried out from 5K to room temperature, with a 100μA drive current for non-irradiated samples and 30μA for irradiated ones. As shown in Figure 5.31(a), the sheet electron density before and after irradiation was stable over all the temperatures studied with a slight increase near room temperature (RT). The increase in the sheet electron density at RT maybe due to the thermal activation of bulk carriers.

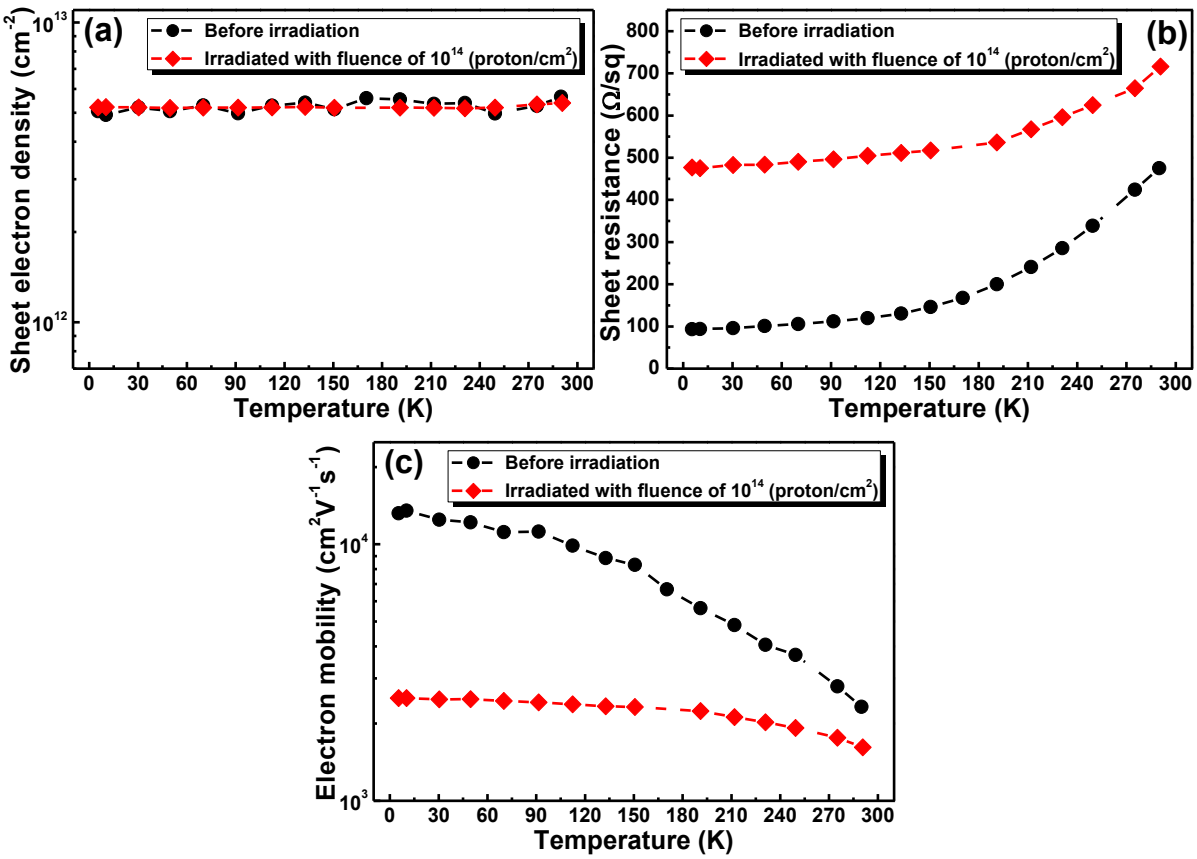

Figure 5. 31 Temperature dependence of (a) the sheet electron density, (b) the sheet resistance and (c) the electron mobility, of the AlGaN/GaN heterostructure before and after irradiation.

Since the sheet electron density is inversely proportional to the absolute sensitivity, we

conclude that the absolute sensitivity is stable over this range of temperature after irradiation. The sheet resistance shown in Figure 5.31(b), increased with increasing temperature for both samples, which is related to the decrease of the mobility as shown in Figure 5.31(c).

Rate of change of mobility can be divided in three regions: (1) lower than 90K the mobility is almost constant in this region, with the three probable scattering mechanisms being interface roughness, alloy disorder, and impurities scatterings. Ling *et al.* report on the observation of a change in the surface roughness of a GaN layer after proton irradiation due to impurities or point defects [11]. Increases in interface roughness and/or impurities near the AlGaN/GaN interface can lead to a dramatic decrease in the mobility after irradiation. (2) An intermediate region where the aforementioned scatterings are less pronounced and acoustic phonon scattering begins to dominate. (3) At room temperature, where interface roughness and impurity scatterings can be neglected and optical phonon scattering dominates, which explains the decrease of the rate of change of the mobility near room temperature.

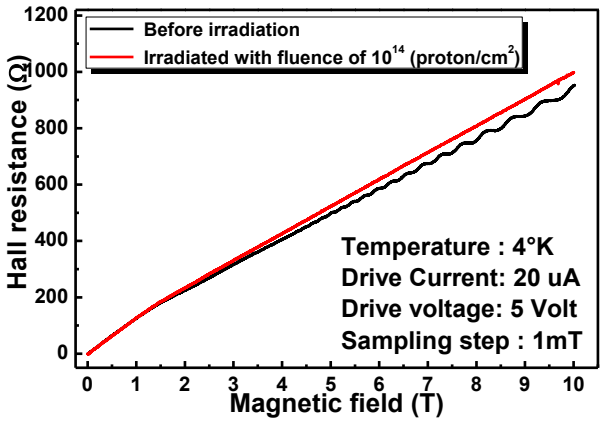

Figure 5.32 Quantum Hall resistances as a function of magnetic field for AlGaN/GaN micro–Hall sensors before and after irradiation.

Figure 5. 32 shows the quantum Hall resistance of the micro–Hall sensor before and after irradiation by proton fluence of 10^{14} (protons/cm^2). The sample before irradiation showed clear Landau plateaus, which started to disappear at 14K. After irradiation, the Landau

plateaus disappear and the Hall resistance becomes linear but this result does not necessarily mean the absence of the 2DEG.

The origin of the Landau levels is due to the 2DEG edge transport at low temperature, electrons can move freely along the interface without scattering which give constant Hall resistance and the magnetoresistance tends to zero. However, increases in electron scattering at the interface can deflect electrons to the bulk and this effect explains the disappearance of the Landau levels. This is the reason why the magnetoresistance increased after irradiation as shown Figure 5.33.

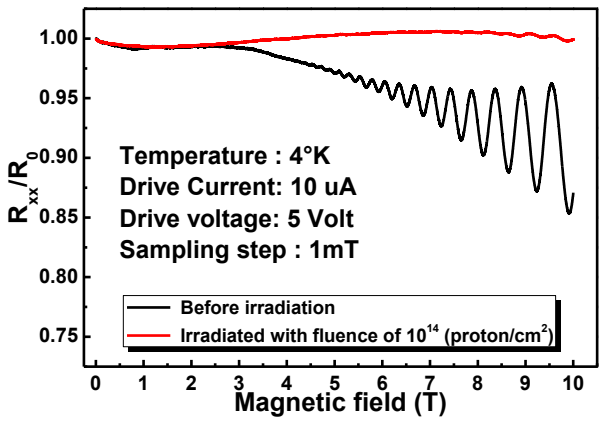

Figure 5.33 The normalized magnetoresistances as a function of magnetic field for AlGaN/GaN micro–Hall sensors before and after irradiation.

The decrease of the minima in the oscillations indicates the absence of parallel conduction. The oscillations are clear from magnetic fields of about 4.5 T before irradiation and from about 8T after irradiation, and we can conclude that the 2DEG remains after irradiation at proton fluence of 10^{14} (protons/cm^2). This increase in the threshold magnetic field is due to the reduction of the mobility after irradiation.

The magnetoelectrical characterization after annealing was carried out for the UID–AlGaN/GaN micro–Hall sensor at cryogenic temperature. The conductivities are measured using the equation:

$$\sigma_{xx} = \frac{\rho_{xx}}{\rho_{xx}^2+\rho_{xy}^2} \quad \text{and} \quad \sigma_{xy} = \frac{\rho_{xy}}{\rho_{xx}^2+\rho_{xy}^2}, \tag{5.8}$$

where ρ_{xx} *and* ρ_{xy} are the longitudinal and the Hall resistivities, respectively, measured according to the equations,

$$\rho_{xx} = \frac{V_{xx}}{I}\frac{W}{L} \quad \text{and} \quad \rho_{xy} = \frac{V_{xy}}{I}, \tag{5.9}$$

I is the applied drive current, V_{xx} the longitudinal voltage measured between the same current probes, V_{xy} is the transversal voltage and W/L is a geometric coefficient equal to $1/26$ in the case of these micro-Hall sensors.

The magnetoconductivities are shown in Figure 5.34. The longitudinal magnetoconductivity (σ_{xx}) showed three behaviors corresponding to weak localization suppression at very low temperature, electron-electron interaction at higher magnetic fields, and Shubnikov de Hass oscillations at very high magnetic fields. The magnetoconductivities decreased after proton irradiation but longitudinal magnetoconductivity was higher in the irradiated sensor when the magnetic field exceeded 1.7T.

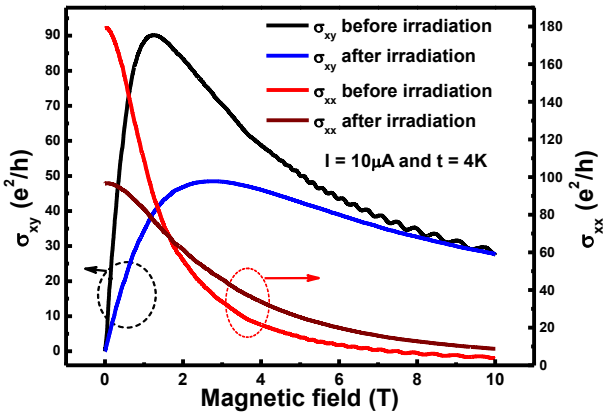

Figure 5.34 Longitudinal and transversal magnetoconductivity of a AlGaN/GaN micro-Hall sensors before and after proton irradiation.

The longitudinal magnetoconductivity can be written in terms of a function of the electron mobility (μ) as $\sigma_{xx} = Ne\mu/(1+\mu^2B^2)$,[12] where N is the electron density, e electron

elementary charge, and B the magnetic field. At very high magnetic fields the value of σ_{xx} converges to the value $Ne/\mu B^2$ which explain the increase in σ_{xx} in the irradiated sample compared with the σ_{xx} in non-irradiated sample. Longitudinal magnetoconductivity increased after applying a very small magnetic field, which corresponds to weak localization suppression explained by the interference distortion of electron waves scattered along closed paths in opposite directions. The weak localization was observed in both samples and it was lower in the irradiated sample as shown in Figure 5.35.

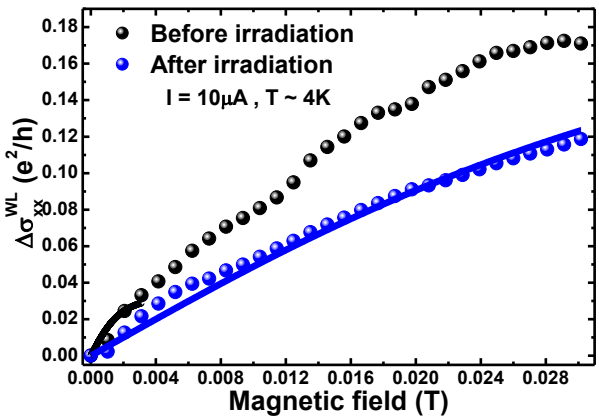

Figure 5.35 Low magnetic field dependence of the longitudinal conductivities of AlGaN/GaN micro-Hall sensors before and after irradiation.

The correction of the magnetoconductivity $\Delta\sigma_{xx}^{WL}(B) = \sigma_{xx}^{WL}(B) - \sigma_{xx}^{WL}(0)$ is given by [13],

$$\Delta\sigma_{xx}^{WL}(B) = \frac{e^2}{\pi h}\left[\Psi\left(\frac{1}{2}+\frac{B_\varphi}{B}\right) - \Psi\left(\frac{1}{2}+\frac{B_e}{B}\right)\right], \tag{5.10}$$

where $\Psi(x)$ is the digamma function, B_φ and B_e correspond to the phase relaxation and the transport scattering rates, respectively. B_φ and B_e are given by the equations $B_\varphi = \hbar/4eD\tau_\varphi$ and $B_e = \hbar/4eD\tau_e$, τ_φ and τ_e are the phase and the momentum relaxation times, respectively, $\hbar$ is the reduced Plank constant and D represents the electronic diffusion constant given by $D = V_F^2\tau_e/2 = l^2/(2\tau_e)$, V_F is the Fermi velocity.

The elastic mean free path (l) is deduced from the 2D Drude conductivity (σ_D), given by,

$$\sigma_D = \frac{e^2}{h} k_F l \quad , \tag{5.11}$$

where k_F is Fermi wave vector given by $k_F = \sqrt{2\pi N}$. σ_D can be written in function of the electron mobility (μ) as $\sigma_D = Ne\mu$ and therefore the elastic mean free path is reduced to,

$$l = \hbar\mu\sqrt{2\pi N}/e \tag{5.12}$$

The momentum relaxation time (τ_e) is given by $\tau_e = m^*\mu/e$, where m^* is the electron effective mass calculated from the electron mass (m_e) as $0.2m_e$ [14]. The main parameter affecting the momentum relaxation time is the electron mobility which decreased from 13200 cm^2/Vs before irradiation to 2510 cm^2/Vs after irradiation near 4K, therefore, the effective mass of electron after irradiation, which could not be measured due to unclear Shubnikov de Haas oscillations [14] was estimated to be unchanged. The weak localization described by equation (5.10) corresponds to the diffusion theory when the magnetic field is lower than the transport magnetic field (B_e or B_{tr}) [15], which were about 1.37 mT and 36.75 mT for the non-irradiated and irradiated samples, respectively, as shown in Table 5.3. The weak localization effect is strongest for magnetic field lower than the transport magnetic field (B_{tr}) [16], therefore, the longitudinal magnetoconductivity in the non-irradiated sample was fitted using only the four measurement data, as shown by the black line in the Figure 5.35. The blue line in Figure 5.35 corresponds to the fitting results of the longitudinal magnetoresistance after irradiation, the phase-relaxation times deduced in both samples. Parameters obtained for both samples before and after irradiation at 4K and current of $10\mu A$ are shown in Table 5.3.

Table 5.3. Magnetoelectrical properties of AlGaN/GaN micro-Hall sensors at 4K.

	μ(cm^2/Vs)	N_s(cm^{-2})	l(μm)	D(m^2/s)	B_e(mT)	τ_e(ps)	τ_ϕ(ps)
Before Irradiation	13200	5.1×10^{12}	0.489	0.079	1.37	1.502	1.614
After Irradiation	2510	5.2×10^{12}	0.095	0.0157	36.75	0.286	0.451

The momentum relaxation time (τ_e) decreased after irradiation due to elastic scattering enhancement by proton irradiation. The dominant mechanism for elastic scattering is impurity scattering [17], therefore, the decrease in the momentum relaxation time can be correspond to impurity scattering enhancement.

The phase-relaxation time (τ_φ) corresponds to the dephasing or the decoherence between two electron waves traversing along the same path but in opposite directions due to inelastic scattering [18]. Therefore, the decrease in τ_φ observed after proton irradiation was due to inelastic scattering enhancement after irradiation. The electron-electron interaction is the dominant inelastic scattering at low temperature [17].

The absolute magnetic sensitivity (S_A) and the supply-current-related sensitivity (SCRS or S_I) are given by $S_A = V_H/B_\perp$ *and* $S_I = S_A/I$, respectively, where $V_H = V_{xy}$ represents the output Hall voltage, $B_\perp$ is the normal component of the magnetic field and I the drive current. The magnetic sensitivity at low temperature was almost unchanged after proton irradiation as shown in Figure 5.36 due to conservation of the electron density [14].

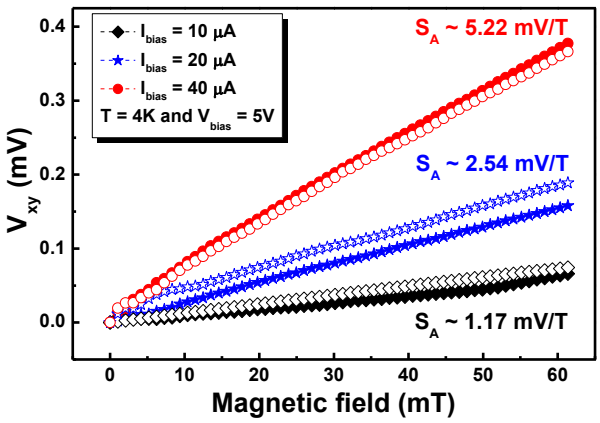

Figure 5.36 Magnetic field dependence of the Hall voltage of AlGaN/GaN micro-Hall sensors, the filled shapes belong to sample before irradiation and hollow shapes to sample irradiated.

The absolute value of the magnetovoltage of the samples at very low magnetic field and temperature of 4K was estimated to vary linearly. The slopes S, which represents the

magnetoresistance sensitivity, were extracted at different drive currents as shown in Figure 5.37, where the biased voltage was fixed to 5V for all measurements.

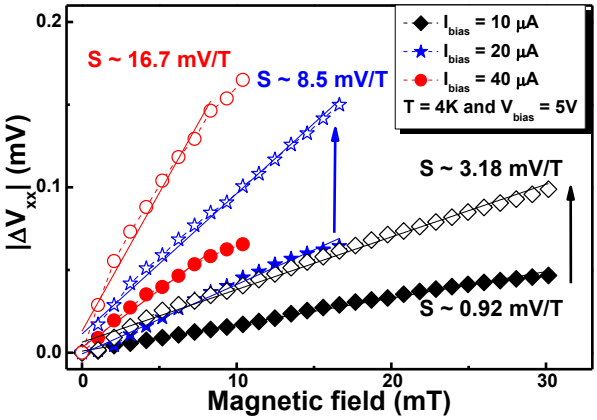

Figure 5.37 Magnetic field dependence of the magnetovoltage of AlGaN/GaN micro-Hall sensors, the filled shapes belong to sample before irradiation and hollow shapes to sample irradiated.

The absolute magnetoresistance sensitivity S, given by $S = |\Delta V_{xx}|/B_{\perp}$ where ΔV_{xx} is given by $\Delta V_{xx} = V_{xx}(B) - \Delta V_{xx}(0)$, was three times higher in the irradiated sample compared with the magnetic sensitivity (S_I) measured from the Hall voltage at the same measurement conditions.

The magnetic sensitivity (S_I) was measured from 5K to room temperature and the magnetic sensitivity was stable and unchanged after irradiation. The absolute magnetoresistance sensitivity (S) was higher in both samples compared with the magnetic sensitivity (S_I), as shown in Figure 5.38, and it was enhanced from 160 $VA^{-1}T^{-1}$ in non-irradiated sensor to 417 $VA^{-1}T^{-1}$ at 5K after proton irradiation (blue filled shapes in Figure 5.38). The value of the magnetoresistance sensitivity is the highest in the AlGaN/GaN heterostructures based Hall sensors; however this value is still lower than in the conventional Hall sensors used for cryogenic temperature magnetic field sensing (MagCam CHS-6 microscopic high sensitivity cryogenic Hall sensors).

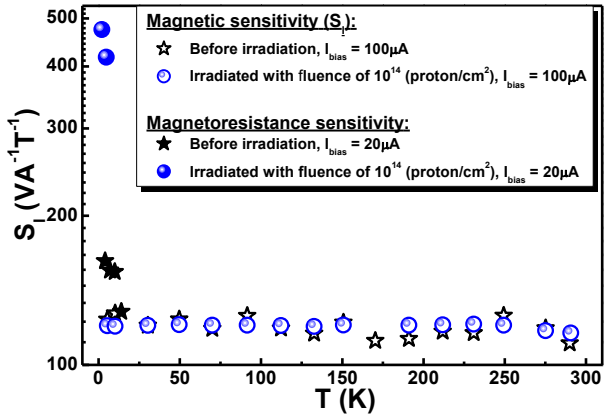

Figure 5.38 Temperature dependence of the magnetic sensitivity of AlGaN/GaN micro-Hall sensor before and after irradiation, the hollow shapes belong to the magnetic sensitivity (S_I) and the filled shapes belong to the absolute magnetoresistance sensitivity (S).

The minimum detectable magnetic field is deduced when the ratio $V_{measured}/V_{noise} = 1$, $V_{measured}$ is the Hall voltage (V_H) given by the equation $V_H = S_I IB$ and the magnetovoltage (V_{xx}) given by the equation $V_{xx} = SIB$ in the transversal and the longitudinal directions, respectively, Johnson noise given by $V_{noise} = [4k_B T R_S \Delta f]^{1/2}$ is the main noise component, therefore, B_{min} is reduced to $B_{min} = \left([4k_B T R_S \Delta f]^{1/2}/SI\right)$, where k_B is Boltzmann constant, T is the temperature, R_S is the series resistance and Δf is the measurement bandwidth. The minimum detectable magnetic field was measured from 5K to room temperature for samples in which the series resistance increased after irradiation as shown in the inset of Figure 5.39. The B_{min} showed lower variation rate after irradiation room temperature due to the dominant electron-phonon scattering that slightly affects the transport properties [14]. The minimum detectable magnetic field measured from the magneto–voltage at 5K in the irradiated sensor was similar to the minimum magnetic field in the non-irradiated sample.

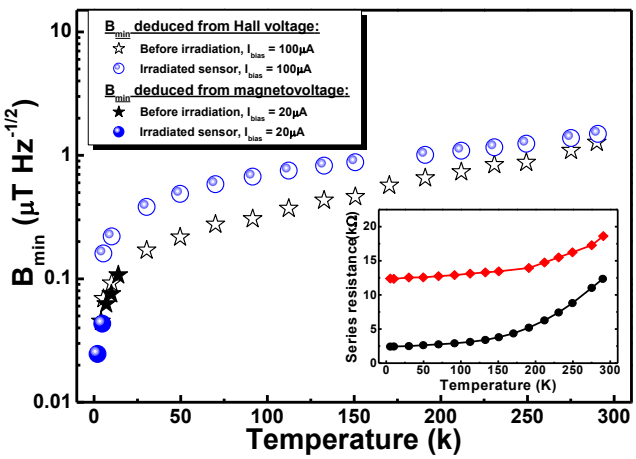

Figure 5.39 Temperature dependence of the minimum detectable magnetic field of AlGaN/GaN micro-Hall sensor before and after irradiation, the hollow shapes belong to the magnetic sensitivity measured from Hall voltage and filled shapes belong to the magnetosensitivity measured from the magnetovoltage.

5-2-3 Proton implantation in InAsSb quantum well based micro-Hall sensors

The InAsSb heterostructures quantum wells (QWs) showed electrical mobility (μ) degradation in all samples when proton fluence increases, due defects creation after irradiation. Table 5.4 shows the irradiation doses and the electrical properties details before and after irradiation. The sheet carrier density (N_S) increases with increasing proton fluence. Generally, an increase in the sheet carrier density leads to a decrease in the sheet resistance, however, due to the mobility drops, the sheet resistance (R_{sh}) increases with increasing the proton fluence.

The magnetic field dependence of the Hall voltage (V_H) before and after irradiation at two values of drive currents is shown in Figure 5.40(a), (b) and (c) for the samples K3875, K3924, and K3960, respectively.

Table 5.4 Electrical characteristics of the InAsSb QWs based micro–Hall sensors at room temperature before and after irradiation.

Sample	Proton fluences	R_{sh} (Ω/□)	N_s (cm^{-2})	μ (cm^2/Vs)
InAsSb QW	Before Irradiation	222	6.69×10^{11}	42027
(Sn-doped 5×10^{16} cm^{-3})	1st Irradiation (f=10^{11} p·cm^{-2})	266	6.87×10^{11}	34160
[K3875]	2nd Irradiation (f=10^{14} p·cm^{-2})	274	$1{,}10\times10^{12}$	20710
InAsSb QW	Before Irradiation	243	9.75×10^{11}	26350
(Sn-doped 7×10^{16} cm^{-3})	1st Irradiation (f=10^{12} p·cm^{-2})	240	9.96×10^{11}	26110
[K3924]	2nd Irradiation (f=10^{15} p·cm^{-2})	497	$2{,}17\times10^{12}$	5790
InAsSb QW	Before Irradiation	55	$3{,}03\times10^{12}$	37450
(Sn-doped 10^{17} cm^{-3})	1st Irradiation (f=10^{13} p·cm^{-2})	72	3.01×10^{12}	28800
[K3960]	2nd Irradiation (f=10^{16} p·cm^{-2})	1341	$1{,}22\times10^{13}$	382

The Hall voltage showed a clear linear dependence on the magnetic field in all samples either after irradiation by proton fluence of 10^{16} protons/cm^2 as shown in Figure 5.40(c). The absolute magnetic sensitivity calculated from the slope Hall voltage on the magnetic field start to change from the irradiation fluence of 10^{14} protons/cm^2 as shown in Figure 5.40(a) by the hollow diamond shape. The magnetic sensitivity decreases by 39%, 55% and 75% after proton irradiation fluence of 10^{14}, 10^{15} and 10^{16} protons/cm^2, respectively.

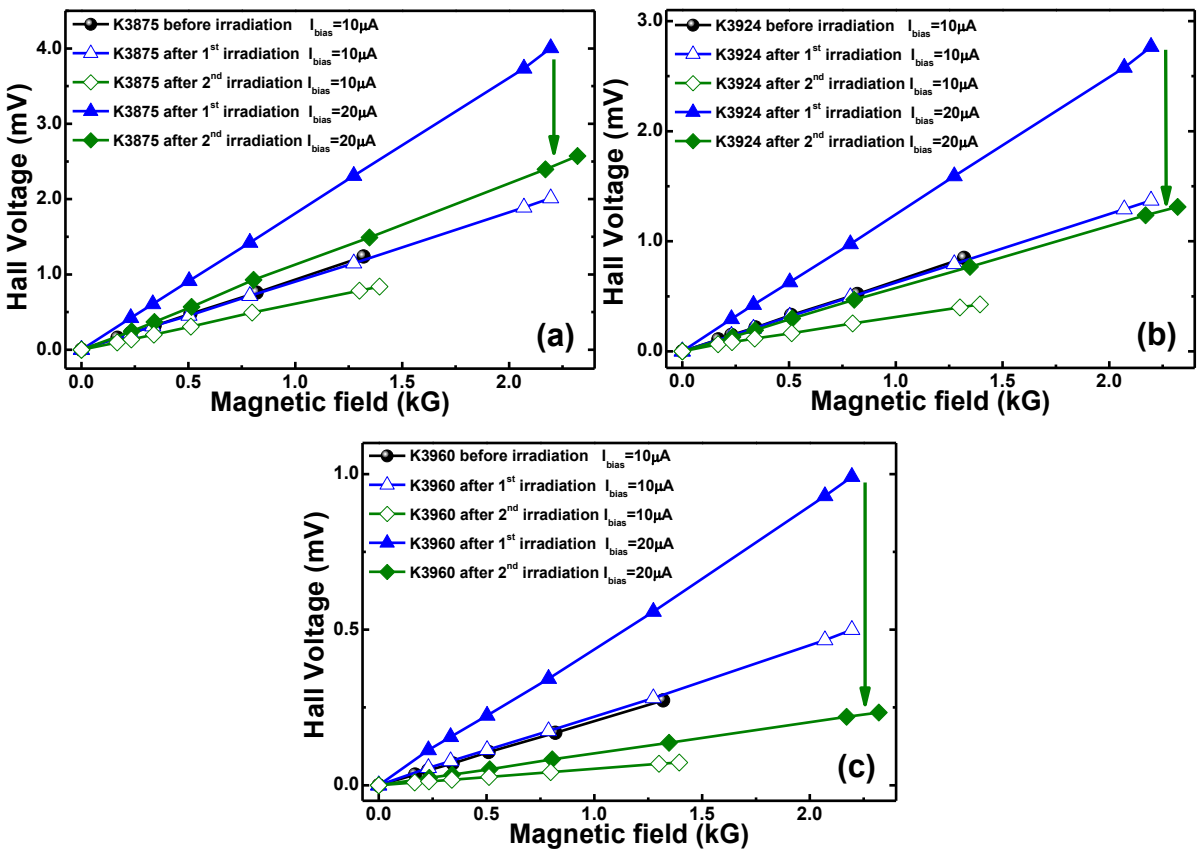

Figure 5.40 Variation of Hall voltage versus the magnetic field of the sample (a) K3875 (b) K3924 and (c) K3960, before and after irradiation at different values of proton fluence (the round filled shapes correspond to the reference samples before irradiation).

The decrease in the magnetic sensitivity, as shown in Figure 5.41, was due to the increase of the sheet carrier density given by $N_S \approx 1/(q \times S_I)$ where q is the electron's elementary charge. Generally, III-V compound semiconductors irradiated with high-energy protons, generally, show degradation of the initial carrier density due to the defects and traps creation with energy levels in the middle of the band gap. However, Brudnyĩ et al. [19] reported some exceptions in InAs, InP, and InN where shifting and pinning of the Fermi level near or in the conduction band occurred and leads to sheet carrier density increasing. Steenbergen et al. reported the increase in the sheet carrier density in the InAs/$InAs_{0.6}Sb_{0.4}$ superlattices after proton irradiation [20]. Proton irradiation effect on the InSb and AlSb doped these materials p-type [19]. There are no reports concerning the proton irradiation effect of the $Al_{0.1}In_{0.9}Sb$

and $InAs_{0.1}Sb_{0.9}$ compounds, however, shifting of the Fermi level to the valence band in the AlInSb layers and/or to the conduction band in the InAsSb layer can explained the increasing in the sheet carrier density observed.

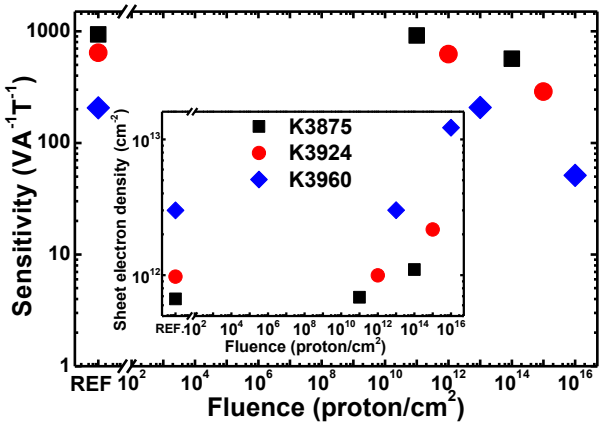

Figure 5.41 Dependence of the magnetic sensitivity of InAsSb based quantum well on 380 keV proton fluence.

The minimum detectable magnetic field after proton irradiation was almost stable up to proton fluence of 10^{14} protons/cm^2, as shown in Figure 5.42. The increase of the minimum detectable magnetic field at higher proton fluence was due to the increase in the sheet resistance and the decrease of the magnetic sensitivity. B_{min} was about 10 μTHz$^{-1/2}$ after proton irradiation with fluence of 10^{16} protons/cm^2, which represent an increase about eight folds of its initial value. B_{min} decreased to a value of 2.6 μTHz$^{-1/2}$ at biased current of 40 μA in the micro-Hall sensor irradiated with proton fluence of 10^{16} protons/cm^2 and it is expected to decrease with increasing the biasing current.

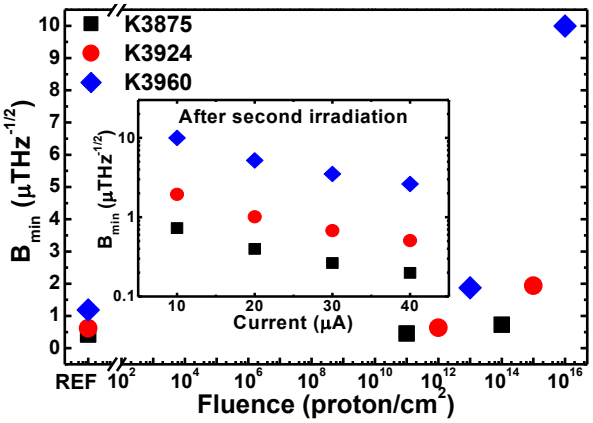

Figure 5.41 Dependence of the minimum detectable magnetic field of InAsSb based quantum well on 380keV proton fluence. Inset: Current dependence of the minimum detectable magnetic field of the micro-Hall sensors after the second irradiation.

5-3 Conclusion

Conventional Hall sensors based on narrow band gap materials such as InSb and GaAs showed application limitation at high temperature. The magnetic sensitivity drops when the temperature rises. The magnetic sensitivity of the micro–Hall sensors based on InAsSb and AlGaAs/GaAs heterostructures drops when the temperature exceeds 150 and 250°C, respectively. The micro–Hall sensors based on AlGaN/GaN heterostructures showed stable magnetic sensitivity from cryogenic temperature to 400°C. The study of proton irradiation on the AlGaN/GaN heterostructures showed degradation in the electrical properties, however, the magnetic sensitivity was stable up to proton fluence of 10^{14} (proton/cm^2). The micro-Hall sensors based on the AlGaN/GaN heterostructures are suitable for high temperature and harsh environment applications.

5-4 References

[1] Z. H. Liu, S. Arulkumaran, and G. I. Ng; *"Temperature dependence of Ohmic contact characteristics in AlGaN/GaN high electron mobility transistors from −50 to 200 °C"*; Appl. Phys. Lett. **94**, 142105 (2009).

[2] Z. ZhongFen, Z. JinCheng, X. ZhiHao, D. HuanTao and H. Yue; *"High temperature electron transport properties of AlGaN/GaN heterostructures with different Al-contents"*; Sci China Ser. G. **52(12)**, 1879 (2009).

[3] H. Tokuda, J. Yamazaki, and M. Kuzuhara; *"High temperature electron transport properties in AlGaN/GaN heterostructures"*; J. Appl. Phys. **108**, 104509 (2010).

[4] A. H. Zahmani, A. Nishijima, Y. Morimoto, H. Wang, J. F. Li, and A. Sandhu; *"Temperature Dependence of the Resistance of AlGaN/GaN Heterostructures and Their Applications as Temperature Sensors"*; Jpn. J. Appl. Phys. **49**, 04DF14 (2010).

[5] K. E. Sickafus, E. A. Kotomin, B. P. Uberuaga; *"Radiation Effects in Solids: Proceedings of the NATO Advanced Study Institute on Radiation Effects in Solids"*; (Spring 2004).

[6] A. Y. Polyakov, N. B. Smirnov, A. V. Govorkov, and A. V. Markov; "*Neutron irradiation effects on electrical properties and deep-level spectra in undoped n-AlGaN/GaN heterostructures*"; J. Appl. Phys. **98**, 033529 (2005).

[7] G. Sonia, E. Richter, F. Brunner, A. Denker, R. Lossy, M. Mai, F. Lenk, J. Bundesmann, G. Pensl, J. Schmidt, U. Zeimer, L. Wang, K. Baskar, M. Weyers, J. Wuerfl, G. Traenkle; "*2 MeV ion irradiation effects on AlGaN/GaN HFET devices*"; Solid-State Electronics. **52**, 1011 (2008).

[8] L. L. Hung, C. .K. Ming, H. S. Shian, C. T. Liang, H. W. Chang, K. Y. Chen, S. Z. Hao, P. H. Chang, N. C. Chen, C. C. An; "*Electron heating in $Al_{0.15}Ga_{0.85}N$/GaN heterostructures grown on p-type Si*"; Physica E, **40**, 343 (2007).

[9] S. Elhamri, W. C. Mitchel, W. D. Mitchell, R. Berney, M. Ahoujja, J. C. Roberts, P. Rajagopal, T. Gehrke, E. L. Piner, K. J. Linthicum; "*A magnetotransport study of*

AlGaN/GaN heterostructures on silicon"; Journal of Electronic Materials **34**, 444 (2005).

[10] S.V. Danylyuk, S.A. Vitusevich, B. Podor, A.E. Belyaev, A.Yu. Avksentyev, V. Tilak; J. Smart, A. Vertiatchikh, L.F. Eastman; "*The investigation of properties of electron transport in AlGaN/GaN heterostructures*"; Microelectronics Journal **34**, 575 (2003).

[11] Ling Lü, Yue Hao, XueFeng Zheng, JinCheng Zhang, ShengRui Xu, ZhiYu Lin, Shan Ai and FanNa Meng; "*Proton irradiation effects on HVPE GaN*"; Science China Technological Sciences **55**, 2432 (2012).

[12] S. T. Lo, Y. T. Wang, S. D. Lin, G. Strasser, J. P. Bird, Y. F. Chen and C. T. Liang; "*Tunable insulator-quantum Hall transition in a weakly interacting two-dimensional electron system*"; Nano. Res. Lett. **8**, 307 (2013).

[13] S. V. Kravchenko, M. P. Sarachik; "*Metal–insulator transition in two-dimensional electron systems*"; Rep. Prog. Phys. **67**, 1 (2004).

[14] A. Abderrahmane, S. Koide, T. Tahara, S. Sato, T. Ohshima , H. Okada and A. Sandhu; "*Effect of Proton Irradiation on 2DEG in AlGaN/GaN Heterostructures*"; J. Phys.: Conf. Series **433**, 012011 (2013).

[15] S. Pedersen, C. B. Sorensen, A. Kristensen, P. E. Lindelof, L. E. Golub and N. S. Averkiev; "*Weak localisation in AlGaAs/GaAs p-type quantum wells*"; arXiv preprint cond-mat/9905057 (1999).

[16] S. T. Lo, F. H. Liu, C. S. Hsu, C. Chang, L. I. Huang, Y. Fukuyama, Y. Yang, R. E. Elmquist, and C.T. Liang; "*Localization and electron-electron interactions in few-layer epitaxial graphene";* Nanotechnology **25**, 245201 (2014).

[17] Eckehard Schöll; "*Theory of Transport Properties of Semiconductor Nanostructures*"; (Chapman & Hall 1998) p.12.

[18] G. M. Minkov, A. V. Germanenko and I. V. Gornyi; "*Magnetoresistance and dephasing in a two-dimensional electron gas at intermediate conductances*"; Phys. Rev. B **70**, 245423 (2004).

[19] V. N. Brudnyĩ, N. G. Kolin and L. S. Smirnov; "*The model of self-compensation and pinning of the Fermi level in irradiated semiconductors*"; Semiconductors, **41** No. 9, 1011 (2007).

[20] E. H. Steenbergen, J. A. Massengale, V. M. Cowan, Z. Lin, Y. H. Zhang, C. P. Morath; "*Proton radiation effects on the photoluminescence of infrared InAs/InAsSb superlattices*"; Nanophotonics and Macrophotonics for Space Environments VII, **8876**, 887609 (2013).

Chapter 6

Effect of annealing on proton irradiated Hall sensors

With the aim of recovering the initial electrical properties of proton-irradiated AlGaN/GaN heterostructures, the effect of annealing on thick has been studied. Recovering in the electrical and structural properties was observed.

6-1 Electrical characterizations

To follow the annealing process the series resistance (R_S) was measured for all samples as they were heated from RT to 400°C over the course of approximately 3 min. The series resistance of the samples before irradiation are represented by the black curves in Figure 6.1(a) and Figure 6.1(b) and the series resistance of the micro-Hall sensors irradiated by a proton fluence of 10^{14} (protons/cm^2) during heating is represented by the red curves.

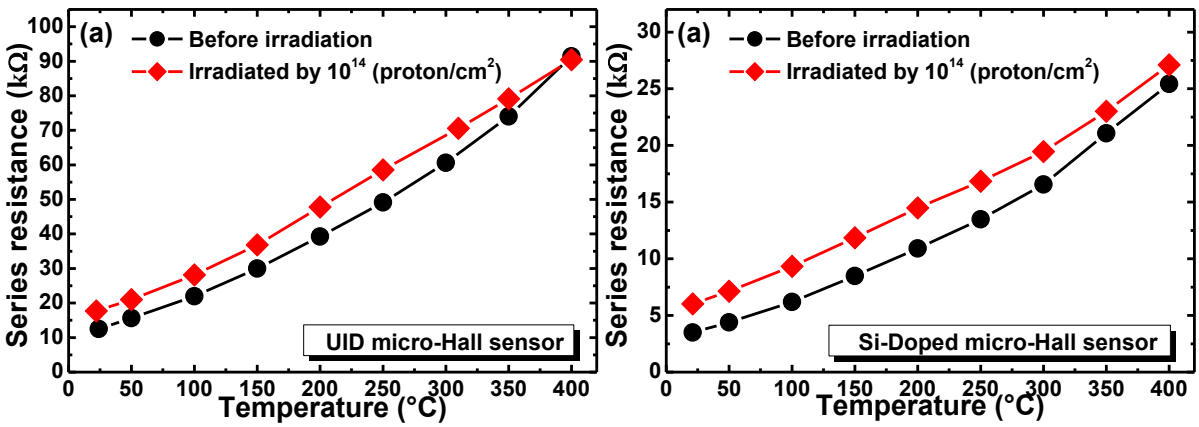

Figure 6.1 Temperature dependence of series resistance of (a) the UID– and (b) the Si–doped, micro-Hall sensors before and after irradiation by proton fluence of 10^{14} (p/cm^2).

The series resistance showed increases after irradiation due to electron mobility decreases. At a temperature of around 200°C there is a small drop in the series resistance, which indicates

the beginning of the annealing process, and corresponds to a value of the threshold annealing temperature that is close to those previously reported for thick GaN [1,2].

The series resistance of the micro–Hall sensors irradiated with a fluence of 10^{15} (protons/cm^2) during annealing is represented by the red curve in Figure 6.2(a) and Figure 6.2(b) and showed an exponential decrease with increasing temperature.

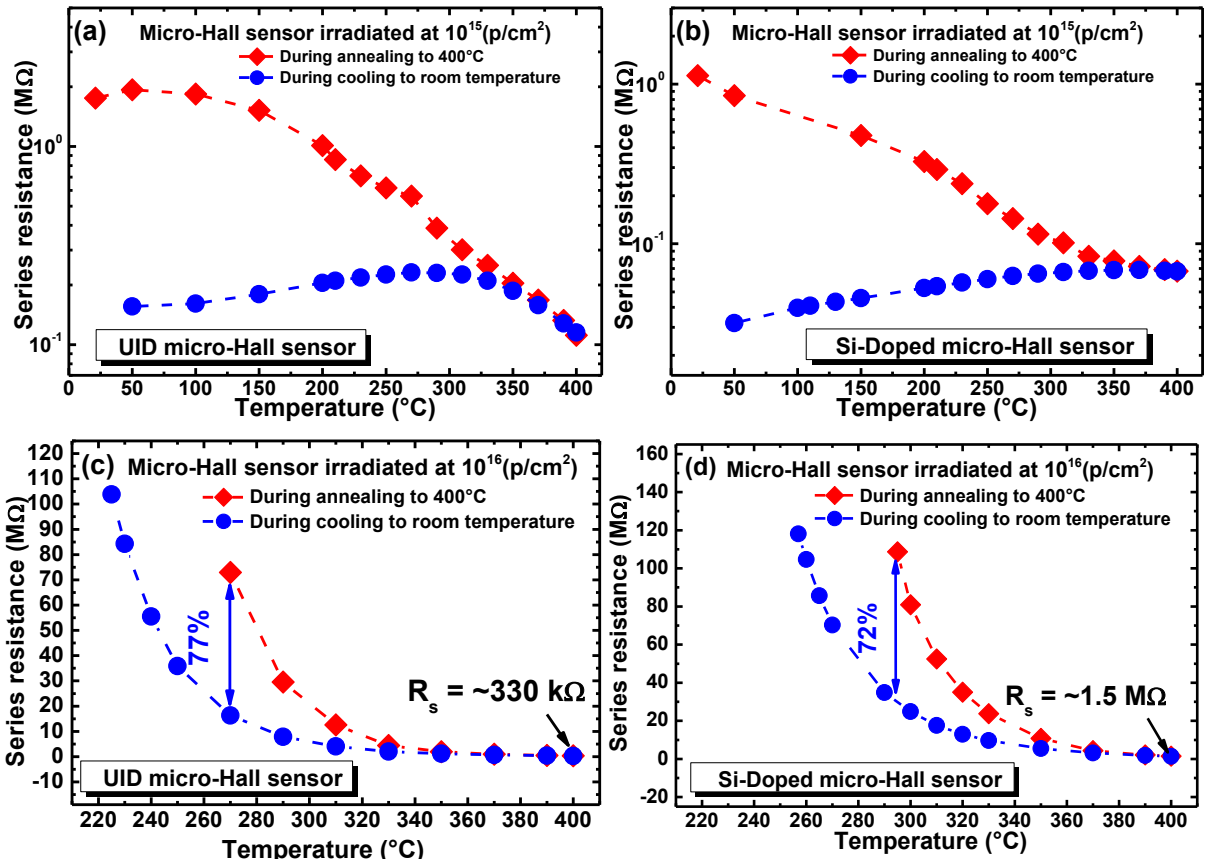

Figure 6.2 Temperature dependence of series resistance of (a) UID– and (b) the Si–doped, micro–Hall sensors irradiated with a fluence of 10^{15} (protons/cm^2), (c) UID– and (d) the Si–doped, micro–Hall sensors irradiated with a fluence of 10^{16} (protons/cm^2).

The series resistance in the UID– micro–Hall sensor, shown in Figure 6.2(a), was almost stable between room temperature (RT) and 150°C. At low temperatures, rearrangement of atoms and defects removal is impossible. Therefore, stable series resistance was observed in the UID– sample and the decrease of the series resistance observed between 50 °C and

200 °C in the Si–doped sample, shown in Figure 6.2(b), was probably due to thermal activation of electrons from trap levels to the conduction band in either the AlGaN or the GaN layer. After annealing, the series resistance significantly decreased by about 91.1% and 97.2% near RT of the UID– and Si–doped micro–Hall sensors, respectively. For the micro–Hall sensors irradiated by a proton fluence of 10^{16} (protons/cm^2), the series resistance decreased with increasing temperature. The resistance was too high to measure until the temperature reached 300°C, and from here the resistance dropped further on increasing the temperature to 400°C to a value of 0.33MΩ as shown in the Figure 6.2(c) in the UID–micro–Hall sensor and to a value of 1.5MΩ as shown in the Figure 6.2(d) in the Si–doped micro–Hall sensor.

The series resistance during cooling of the samples irradiated by fluence of 10^{15} (protons/cm^2) represented by the blue curves in Figure 6.2(a) and Figure 6.2(b), showed exponential decrease corresponding to the variation in resistance of a 2DEG. In contrast, the last samples (irradiated by fluence of 10^{16} (protons/cm^2)) showed an increase in the series resistance with decreasing temperature. The annealing temperature used here was too small to remove all the defects caused by proton irradiation and hence electrons could be trapped again during cooling by the remaining defects, causing the series resistance to increase. Polyakov *et al.* report that even at temperatures as high as 550°C, the annealing is not completed in proton-irradiated thick GaN [2].

The current–voltage characteristics after irradiation were found to have degraded as shown in Figure 6.3 in the case of the UID– AlGaN/GaN micro–Hall sensor, which was caused by increased scattering at the AlGaN/GaN interface due to the creation of traps and defects by damage after irradiation. The current–voltage curves showed a decrease of current by 57% and 99.5% at 30 V and strong deterioration in saturation current by 83% and 99.8% for samples irradiated at 10^{14} and 10^{15} (protons/cm^2) proton fluencies, respectively. The sample irradiated with 10^{16} protons/cm^2 was completely damaged and high resistance. The

Si–doped AlGaN/GaN micro–Hall sensor showed the same degradation behavior.

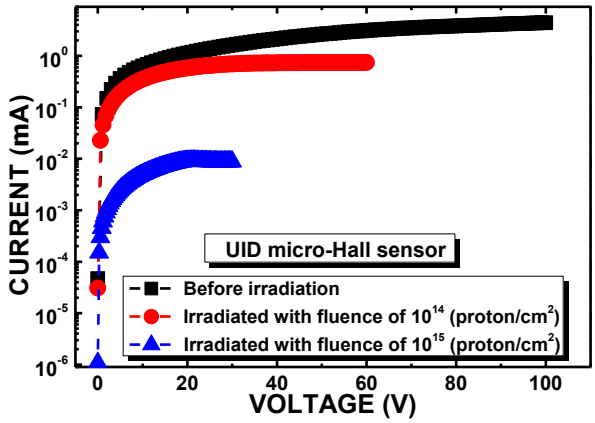

Figure 6.3Current–Voltage characteristics of the UID– AlGaN/GaN micro–Hall sensor before and after irradiation.

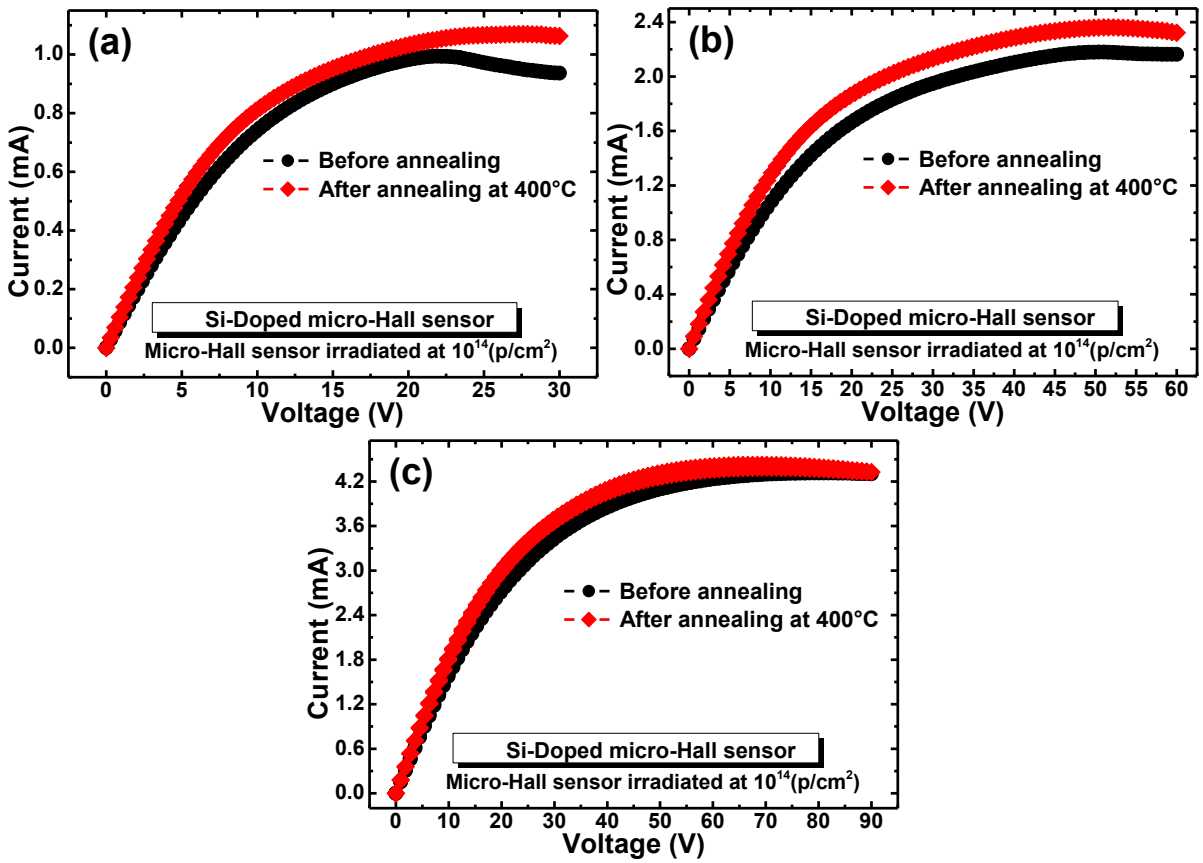

Figure 6.4 Effect of annealing at 400°C on the current–Voltage characteristics of Si–doped AlGaN/GaN micro–Hall sensors irradiated with proton fluence of 10^{14} (p/cm^2) with active area of (a) 1×1μm^2, (b) 2×2μm^2 and (c) 5×5μm^2.

The effect of annealing of the micro–Hall sensors at temperature of 400°C on the current–voltage characteristics is discussed. Figure 6.4 and Figure 6.5 show the effect of annealing on the Si–doped micro–Hall sensors irradiated by proton fluence of 10^{14} (protons/cm^2) and 10^{15} (protons/cm^2), respectively.

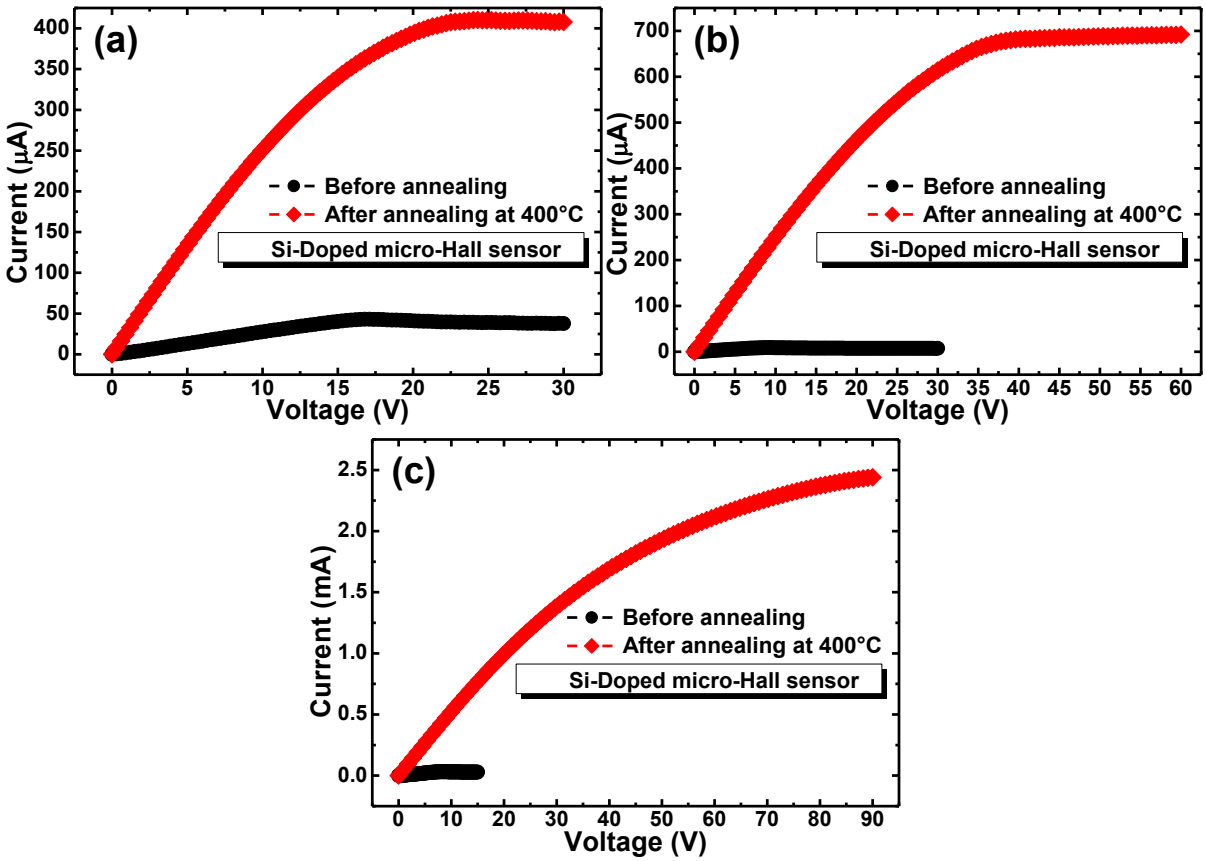

Figure 6.5 Effect of annealing at 400°C on the current–Voltage characteristics of Si–doped AlGaN/GaN micro–Hall sensors irradiated with proton fluence of 10^{14} (p/cm^2) with active area of (a) 1×1μm^2, (b) 2×2μm^2 and (c) 5×5μm^2.

The degradation in the current–voltage characteristics, as shown in Figure 6.6, was due to the trapping effect. The effect of annealing on the current–voltage characteristics for the irradiated sample at 10^{14} protons/cm^2 is drawn in logarithmic scale as shown by the green curve in the inset of Figure 6.6(b). It showed improvement in the current–voltage characteristics after annealing. The pink curves shown in Figure 6.6 correspond to the

micro–Hall sensor irradiated at a fluence of 10^{15} protons/cm^2 before annealing, and the blue curves corresponds to the same sample after annealing. A high improvement in the current–voltage characteristics, in particular we observed an improvement of the saturation current by factor of 16.5 and 77 in the UID– and the Si–doped micro–Hall sensors, respectively, which indicates the excellent advantages of annealing.

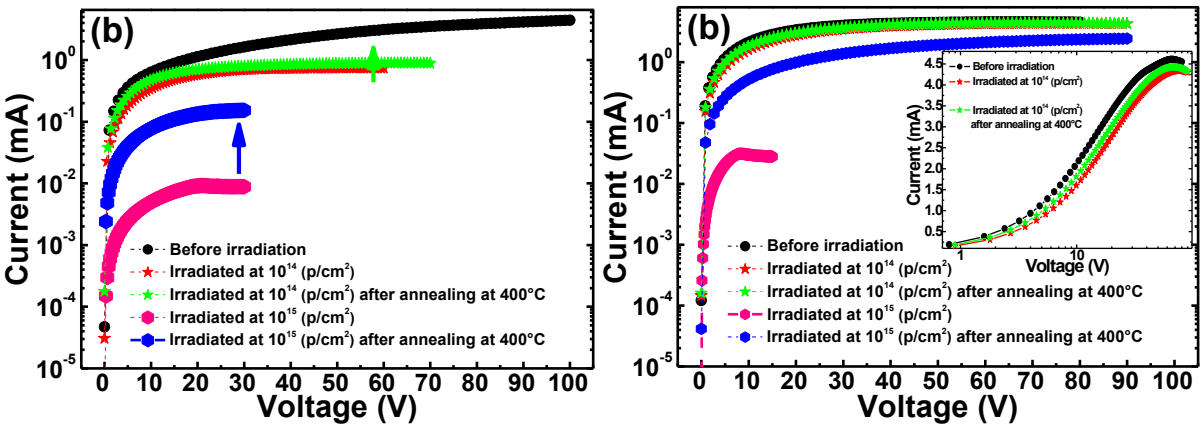

Figure 6.6 Current–voltage characteristics of (a) 1×1μm^2 active area UID– and (b) 5×5μm^2 active area Si–doped AlGaN/GaN micro-Hall sensors before and after irradiation and after annealing.

6-2 Magnetoelcrtrical characterizations

The variation of the sheet electron density as function of temperature of the UID micro–Hall sensor is represented in Figure 6.7. The sheet electron density was stable after irradiation and showed fluctuation at high temperatures, which was also reported by Sonia *et al*. after 2 MeV proton irradiation at 10^{13} proton/cm^2 [3]. Polyakov *et al*. reported stability of the sheet electron density in AlGaN/GaN heterostructures after neutron irradiation and a slight decrease when the neutron fluence exceeded 10^{17} (neutrons/cm^2) and they suggest that the reason is the predominantly piezoelectric origin of the charge carriers in the two–dimensional electron gas (2DEG) rather than charge carriers in AlGaN and GaN layers [4]. In our

experiment, the sheet electron density was almost unaffected by creation of traps in AlGaN and GaN layers due its high concentration compared with concentration of traps [5]. The fluctuation of the sheet electron density near 400°C was caused by increasing voltage measurement errors due to Johnson noise which is proportional to the square root of the sheet resistance variation.

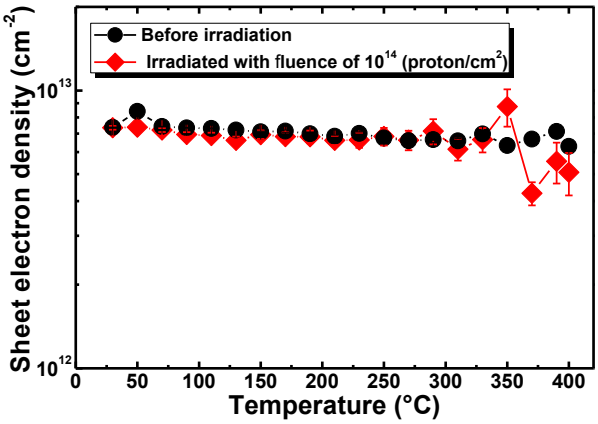

Figure 6.7 Temperature dependence of the sheet density of AlGaN/GaN micro–Hall sensor before and after irradiation.

Before irradiation, the sheet resistance (R_{sh}) is represented by the black curve in Figure 6.8. After irradiation with proton fluence of 10^{14} (protons/cm^2), the sheet resistance represented by the red curve in the Figure 6.8, increased by a factor of about 25% at 90°C which can be explained as being due to scattering of electrons in the 2DEG due to defects created by proton irradiation. Ling *et al.* [6] suggest that gallium vacancies V_{Ga} are more favorable to form with proton irradiation, which leads to an increase in the density of acceptor–like traps. With increasing temperature, the 2DEG electrons in the first subband tend to move into the second and higher subbands [7], electrons in the second and higher subbands extend deeper into the GaN layer and they are less confined in the interface compared with electrons in the first subband [8], thus simulating bulk conditions [9]. Electrons in these subbands experience higher scattering with defects created by proton irradiation in the GaN layer, which explains

the dramatic increase of the sheet resistance at high temperatures.

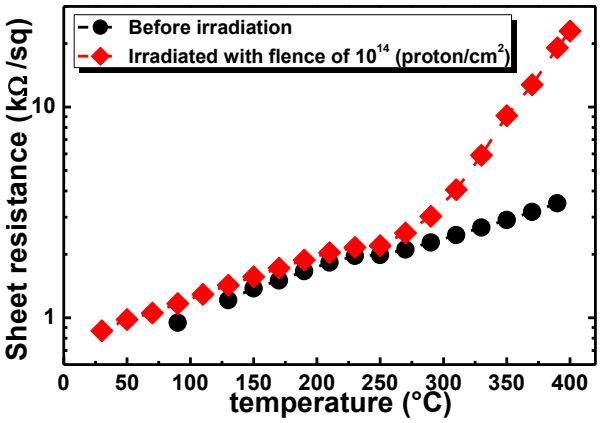

Figure 6.8 Temperature dependence of the sheet resistance in AlGaN/GaN before and after irradiation.

The electron mobility (μ) was calculated directly from the sheet resistance and electron sheet density using the relationship $\mu = 1/(qR_{sh}N_s)$. The electron mobility before irradiation is represented by the black curve in Figure 6.9. The mobility of the irradiated sample by proton fluence of 10^{14} (protons/cm^2) is represented by the red curve in the same figure and showed large decrease at high temperature.

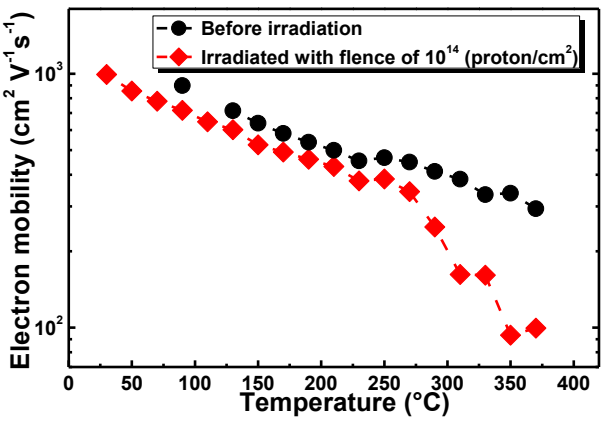

Figure 6.9 Temperature dependence of the electron mobility in AlGaN/GaN before and after irradiation.

The magnetoelectric properties were carried out from room temperature to 400°C in both

samples irradiated by 10^{14} and 10^{15} (protons/cm^2) in the Si–doped micro–Hall sensor; the active area of the sensor is 5×5μm^2. The rate of the increase in the sheet resistance was higher at 400°C for both the samples irradiated at 10^{14} and at 10^{15} protons/cm^2 as shown in Figure 6.10(a), due to electrons moving from the first to higher subbands at high temperatures and entering the GaN layer. The electrons that enter the GaN can be trapped at the defect centers created after irradiation, which has the effect of reducing the 2DEG electron density and enhancing the sheet resistance. The electron mobility is represented in Figure 6.10(b). The annealed sample irradiated at a fluence of 10^{14} protons/cm^2 showed high improvement in the electron mobility whereas the sample irradiated at 10^{15} protons/cm^2 showed very low mobility.

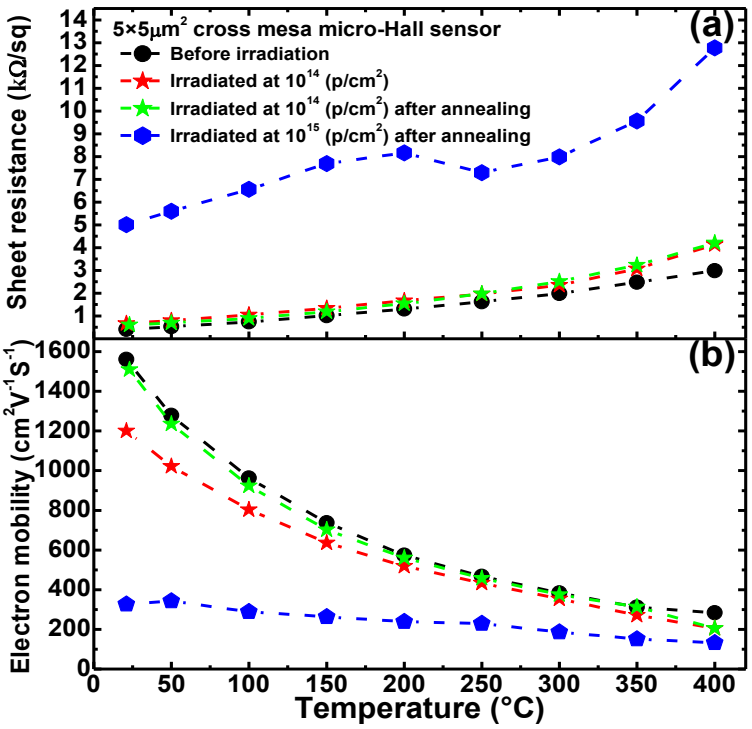

Figure 6.10 The temperature dependence of (a) the sheet resistance and (b) the electron mobility, of the AlGaN/GaN before irradiation and before and after annealing.

The absolute magnetic sensitivity (S_A) after irradiation with a proton fluence of 10^{14}

protons/cm^2 followed by annealing showed a slight increase, as shown in Figure 6.11(a), due to the 2DEG sheet electron density decreasing caused by the trapping effect after irradiation [5]. The minimum detectable magnetic field (B_{min}) showed a slight decrease, as shown in Figure 6.11(b), due to the increase in absolute sensitivity.

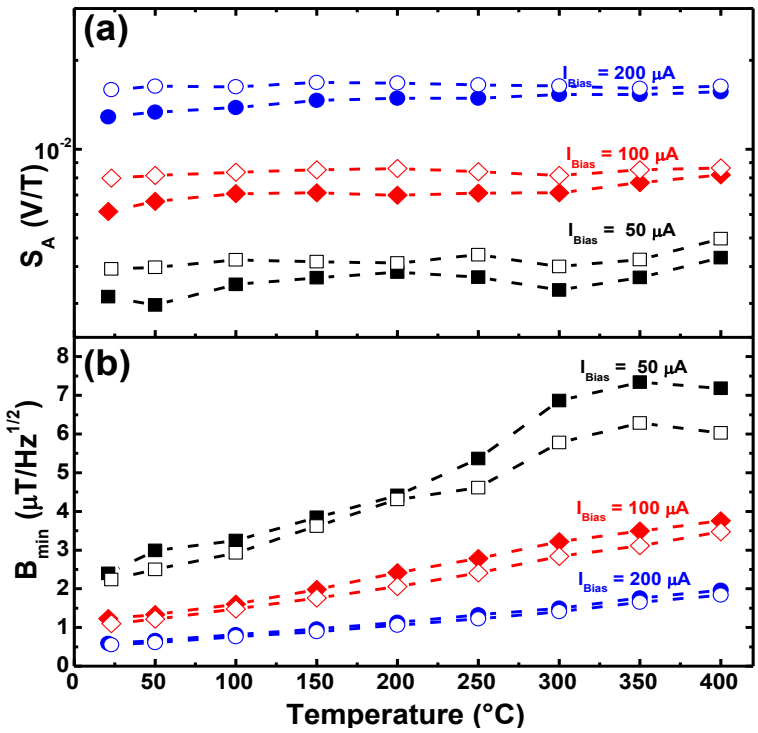

Figure 6.11 Temperature dependence of (a) the absolute magnetic sensitivity, and (b) the minimum detectable magnetic field of the micro–Hall sensors irradiated at a fluence of 10^{14} protons/cm^2 at different values of biasing current. The filled shapes correspond to the irradiated sample before annealing and the hollow shapes represent measurements of the same sample after annealing.

The supply–current–related sensitivity (SCRS) of the micro–Hall sensor irradiated by a fluence of 10^{15} (protons/cm^2) was improved by a factor of 2.73 after irradiation and annealing. The temperature dependence of the absolute magnetic sensitivity is shown in Figure 6.12(a) for two values of biasing current. The increase in the absolute magnetic sensitivity was due to

the decrease in the sheet electron density shown in the inset of Figure 6.12(a).

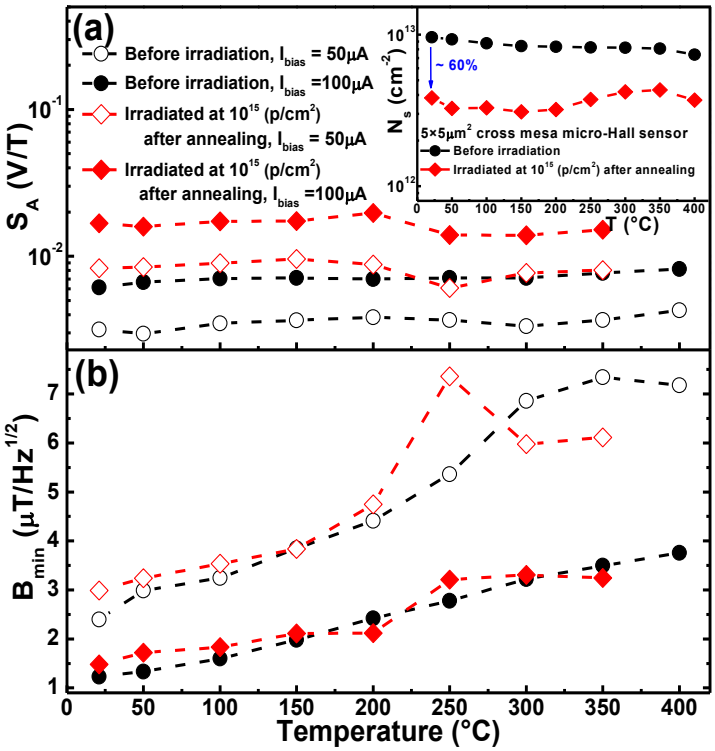

Figure 6.12 Temperature dependence of the (a) absolute magnetic sensitivity, and (b) minimum detectable magnetic field of the micro-Hall sensors before irradiation and after irradiation at a fluence of 10^{15} protons/cm^2 followed by annealing. The inset represents the temperature dependence of the sheet electron density before irradiation and after irradiation and annealing.

The temperature dependence of the minimum detectable magnetic field after annealing is shown in Figure 6.12(b) at two values of biasing current. Only a slight increase in the minimum detectable magnetic field is observed near room temperature due to the simultaneous increase of the square root of the series resistance and the Hall coefficient R_H by a factor of 3.46 and 2.73 respectively, giving an increase in B_{min} by factor 1.27 at RT.

The UID– micro–Hall sensor, with active area of 1×1μm^2, irradiated by 10^{15} (protons/cm^2) fluence and annealed became operational when temperature was lower than around 120°C as

shown in Figure 6.13. The increase of the offset voltage at higher temperature as shown in the inset of Figure 6.13 increased the measurement error in the magnetic sensitivity. The supply–current–related sensitivity at room temperature increased from 85 $VA^{-1}T^{-1}$ in the non–irradiated sample to about 110 $VA^{-1}T^{-1}$ after irradiation and annealing due to decrease in the sheet electron density.

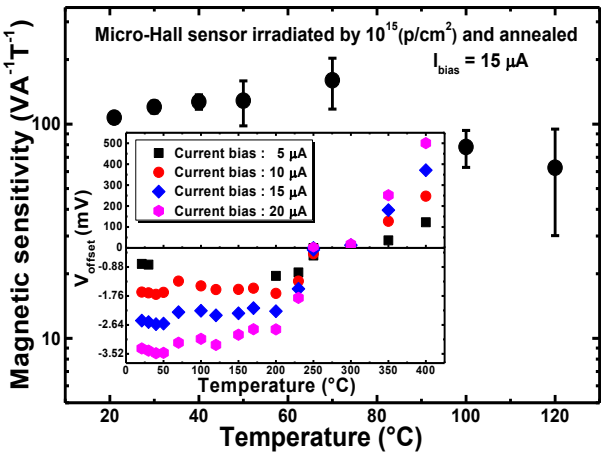

Figure 6.13 Temperature dependence of the supply-current-related sensitivity. Inset of the figure represents the temperature dependence of the absolute value of voltage offset.

6-3 Optical characterization

6-3-1 Raman spectroscopy

NRS-7100 laser Raman spectrometer, shown in Figure 6.14, is used for Raman spectroscopy. Figure 6.15 shows the Raman spectroscopy of the UID– AlGaN/GaN micro–Hall sensors before and after proton irradiation for different fluencies. The peak wave numbers of E_2^{high} and A_1(LO) phonon modes were 569 cm^{-1} and 736 cm^{-1}, and the peak at 416 cm^{-1} $A_{1g}^{sapphire}$ corresponds to the sapphire substrate. From A_1(LO) peak we can deduced that the energy of longitudinal–optical (LO) phonon in GaN was equal to 91.2 meV.

Figure 6.14 NRS-7100 laser Raman spectrometer.

The crystal quality can be examined by analysis of the full width at half maximum (FWHM) and the line-widths (Γ) of E_2^{high} [10]. The FWHM of E_2^{high} after irradiation with 10^{15} (p/cm^2) proton fluence increased from 2.65 to 2.72 cm^{-1} and to 3.5 cm^{-1} after irradiation with 10^{16} (p/cm^2) proton fluence.

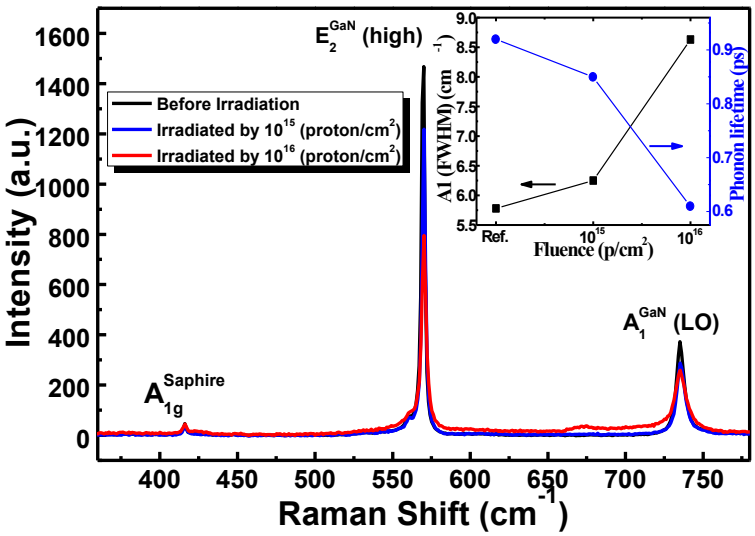

Figure 6.15 Room temperature Raman spectra of the UID AlGaN/GaN heterostructures before and after irradiation. Inset in the figure represent fluence dependence of the A_1(LO) linewidths and the correspond phonon lifetimes, Ref. correspond to the unirradiated sample.

These results imply degradation of the crystalline quality of the GaN due to defects created after irradiation with further degradation with increasing proton fluence. A shift in the E_2^{high} peak frequency was not observed, which implies no changes in the strain state in the GaN layer after irradiation.

In addition, there was no shift in the A_1(LO) indicating, according to the theory of coupled plasmon LO phonon modes [11], that there was no change in the electron density in the GaN layer. The A_1(LO) peak broadened after irradiation, the FWHMs corresponding to the A_1(LO) peak as a function of proton fluence, and the phonon lifetimes deduced from the FWHMs directly using the energy–time uncertainly relation [12], are shown in the inset in Figure 6.15. Short phonon lifetime can be caused by scattering of phonons at impurities or defect centers in the crystal [13], increasing the fluence causes decreases in the phonon lifetime and broadening A_1(LO) linewidths correspond to introducing more defects in the crystal, and therefore decreases in the electron mobility at room temperature was related to the creation of defects and traps in GaN and was not caused by the enhancement of the optical phonon scattering.

Raman spectroscopy of the UID– and Si–doped micro–Hall sensors before irradiation and samples irradiated at 10^{14}, 10^{15} and 10^{16} (protons/cm^2) after annealing at 400°C were carried out. The fluence dependences of the peaks at E_2^{high} and A_1(LO) in both micro–Hall sensor structures are shown in Figure 6.16. A broadening of the A_1(LO) and E_2^{high} peaks corresponds to an increase in the defects concentration and crystal quality degradation, respectively. The narrowing of these two peaks after annealing, as shown in Figure 6.16(a) and Figure 6.16(b), corresponds to defect removal and crystal quality improvement due to the rearrangement of atoms in the GaN that had been moved from their initial positions during irradiation.

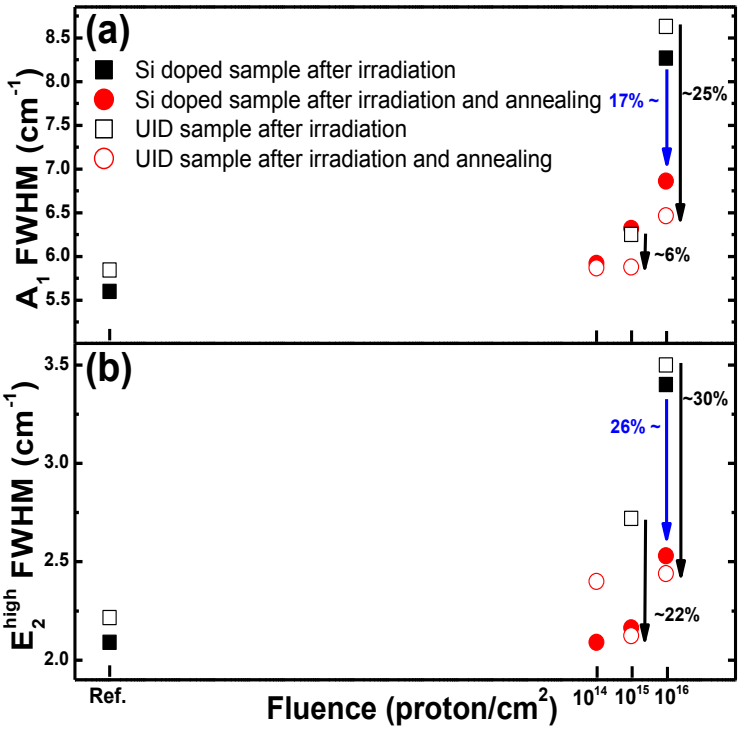

Figure 6.16 The fluence dependence of (a) the A_1(LO) linewidths of the irradiated and the annealed samples and (b) the E_2^{high} linewidths of the irradiated and the annealed samples; Ref. corresponds to the unirradiated samples.

6-3-2 Cathodoluminescence characterizations

Cathodoluminescence measurements were performed using JOEL JSM-5600 SEM equipped with GATAN MonoCL2 system before and after irradiation, where at an acceleration voltage of 5kV, the filament current was 23μA with a resolution of 2 nm. Figure 6.17 shows the results of cathodoluminescence measurements of the AlGaN/GaN micro–Hall sensors before and after irradiation for different proton fluences. Before irradiation, the spectra showed an intense peak at 3.46 eV (358 nm) corresponds to the band edge (BE) emission peak of GaN and a peak centered at 2.25 eV (550 nm) corresponding to green band luminescence (GL) usually observed in high purity GaN. The GL is due to native defects such as gallium vacancies (V_{Ga}) and O_N and their complexes $[V_{Ga}–O_N]^{2-}$, $[V_{Ga}–(O_N)_2]^{1-}$ and $[V_{Ga}–(O_N)_3]^0$ with positions 1.1, 0.7 and 0.8 eV, respectively [14], which have formation energies even lower

than those of isolated V_{Ga} itself [15]. Therefore, the GL is attributed to the transition from the conduction band or a shallow donor level to the V_{Ga}–O_N complex.

After irradiation, the BE peak decreased significantly and disappeared for irradiation at 10^{15} protons/cm^2 due to the enhancement of the gallium and nitrogen vacancies formation after irradiation, which act as electron traps, therefore less electrons are available for the conduction to valence bands transition. The GL peak shifted by about 200 meV to the yellow luminescence band (YL), and increased in intensity with increasing the proton fluence. The increase in the YL band intensity was due to increases of the Ga vacancies density in the GaN, which have an energy level of 1.1 eV above the valence band [16]. Three traps level ER1, ER2 and ER3 at 0.13, 0.16 and 0.25 eV below the conduction band [17] are attributed as the reason for the GL band shift. In addition, the appearance of a peak centered at 2.86 eV (433 nm) corresponding to the blue luminescence band (BL), which increased with increasing the proton fluence. This peak originates from a transition from a shallow donor levels to a deep acceptor level transition. The V_{Ga}^{2-} level state located at 0.64 eV above the valence band [16] is a good candidate for the source of BL emission and the increase in its density with increasing the proton fluence explains the increases of the BL intensity. After annealing, the BE peak of irradiated samples increased in intensity, as shown in the inset in Figure 6.17, and electrons were no longer trapped in the midgap and were available for the conduction to valence band transitions.

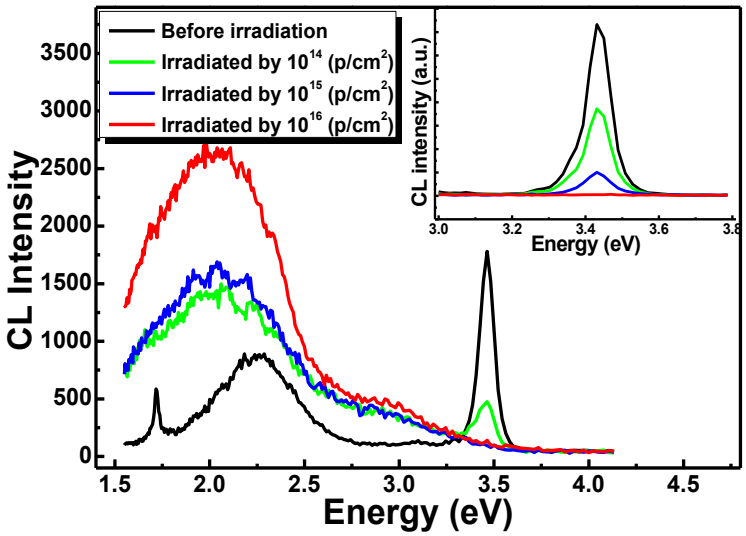

Figure 6.17 Cathodoluminescence measurement of the UID– AlGaN/GaN based micro–Hall sensor before and after irradiation with different proton irradiation fluences. Inset of the figure represents the cathodoluminescence measurement after annealing.

6-4 Conclusion

The effect of annealing on pre-irradiated AlGaN/GaN heterostructures was discussed at temperature annealing of 400°C. The optical characterizations confirm the improvement of the crystal quality of the heterostructures after annealing. The electrical characterizations showed partial recovery of electrical properties corresponds to defects and traps removing as result of annealing. Studying of effect of higher temperature annealing on these devices is needed.

6-5 References

[1] S. O. Kucheyev, H. Boudinov, J. S. Williams, C. Jagadish and G. Li, J. Appl. Phys. **91**, 4117 (2002).

[2] A. Y. Polyakov, A. S. Usikov, B. Theys, N. B. Smirnov, A. V. Govorkov, F. Jomard, N. M. Shmist and W. V. Lundin, Solid-State Electron. **44**, 1971 (2000).

[3] G. Sonia, E. Richter, F. Brunner, A. Denker, R. Lossy, M. Mai, F. Lenk, J. Bundesmann, G. Pensl, J. Schmidt, U. Zeimer, L. Wang, K. Baskar, M. Weyers, J. Würfl, G. Tränkle, Solid-State Electronics **52**, 1011 (2008).

[4] A.Y. Polyakov, N.B. Smirnov, A.V. Govorkov, A.V. Markov, S.J. Pearton, N.G. Kolin, D.I. Merkurisov, V.M. Boiko, M. Skowronski, I.-H. Lee, Physica B **376–377**, 523 (2006).

[5] H. Okada, A. Abderrahmane, S. Koide, H. Takahashi, S. Sato, T. Ohshima and A. Sandhu, Journal of Physics: Conference Series **352**, 012010 (2012).

[6] Ling Lv, J.G. Ma, Y.R. Cao, J.C. Zhang, W. Zhang, L. Li, S.R. Xu, X.H. Ma, X.T. Ren, Y. Hao, Microelectron. Reliab. **51**, 2168 (2011).

[7] N. Maeda, K. Tsubaki, T. Saitoh and N. Kobayashi, Appl. Phys. Lett. **79**, 1634 (2001).

[8] A. Asgari, S. Babanejad and L. Faraone, J. Appl. Phys **110**, 113713 (2011).

[9] B. K. Ridley, B. E. Foutz, and L. F. Eastman, Phys. Rev. B **61**, 16862 (2000).

[10] M. Kuball, J. M. Hayes, T. Suski, J. Jun, M. Leszczynski, J. Domagala, H. H. Tan, J. S. Williams and C. Jagadish, J. Appl. Phys **87**, 2736 (2000).

[11] R. X. Wang, S. J. Xu, S. Fung, C. D. Beling, K. Wang, S. Li, Z. F. Wei, T. J. Zhou, J. D. Zhang and Ying Huang, Appl. Phys. Lett. **87**, 031906 (2006).

[12] X. H. Zhang, C. L. Zhao, J. C. Han, Y. Wang, J. K. Jian, G. Wang, Z. H. Zhang, H. Li, W. J. Wang, Y. T. Song, Y. Liu, H. Q. Bao, X. L. Chen, and B. Song, Appl. Phys. Lett. **102**, 011916 (2013).

[13] S. Tripathy, S. J. Chua, M. S. Hao, E. K. Sia, A. Ramam, J. Zhang, W. H. Sun, and L. S. Wang, J. Appl. Phys **91**, 5840 (2002).

[14] H. Y. Jeong, Ph.D. thesis, University of Illinois at Urbana-Champaign, 2007.

[15] Jörg Neugebauer and Chris G. Van de Walle, Appl. Phys. Lett. **69**, 503 (1996).

[16] M. A. Reshchikov and H. Morkoç, J. Appl. Phys. **97**, 061301(2005).

[17] Z. Zhang, A. R. Arehart, E. Cinkilic, J. Chen, E. X. Zhang, D. M. Fleetwood, R. D. Schrimpf, B. McSkimming, J. S. Speck and S. A. Ringel, Appl. Phys. Lett. **103**, 042102 (2013).

Chapter 7

GENERAL CONCLUSION

1-1Conclusion

In this thesis, we described the fabrication and magnetoelectric properties of robust, high sensitivity Hall effect sensors fabricated using AlGaN/GaN, AlGAAs/GaAs and AlInSb/InAsSb/AlInSb heterostructures with a two-dimensional electron gas at the heterointerfaces. The sensitivity of AlInSb/InAsSb/AlInSb heterostructure degraded above ~150°C. AlGaN/GaN 2DEG Hall sensors were stable between cryogenic temperature to at least 400°C and even after irradiation of 380 keV protons with a fluence of 10^{14} protons/cm^{-2}, but were highly resistive after higher proton fluences. The supply–current–related sensitivity (SCRS) of AlInSb/InAsSb/AlInSb heterostructure was 20% of its initial value after proton irradiation of 10^{16} protons/cm^{-2}. Sensors showed degradation in the current–voltage characteristics and high resistivity due to the creation of defects and traps in the GaN layer.

Annealing removed defects by rearranging atoms in the AlGaN and the GaN layers, thereby partially recovering the electrical properties. We succeeded in recovering about 72% of the series resistance in the micro-Hall sensor irradiated by a fluence of 10^{16} protons/cm^{2} at a temperature of about 300°C, but the resistivity remains high and magnetoelectrical characteristics cannot be measured. The magnetoelectric characterization showed improvements in the magnetic sensitivity. The effect of higher temperature annealing can be discussed in future research.

1-2 Future work

The effect of high temperature, on the physical properties of the irradiated Hall sensors studied in this work, should be studied to recover the initial properties of our sensors. Best

understanding on the effect of annealing on the recovering properties of our sensors may cancel their limitation at very high proton flux and increase their application lifetimes. The sensors could be packaged in order to protect them against higher proton fluences.

The thinner active region, the better the Hall device is, making the 2D materials good candidates as new generation of Hall sensors. We investigate new micro–Hall sensors based on two-dimensional molybdenum diselenide ($MoSe_2$), their magnetic sensitivity was close to AlGaN/GaN heterostructures based Hall sensors, and it depends on the thickness of the layer. The thickness dependence on the physical properties such as the mobility and the magnetic sensitivity, the effect of temperature and particles irradiation is a subject which is interesting for future research.

Research achievements

Papers

1) A. Abderrahmane, P. J. Ko, H. Okada, S. I. Sato, T. Ohshima and A. Sandhu, "Proton Irradiation Enhancement of Low-Field Negative Magnetoresistance Sensitivity of AlGaN/GaN based Magnetic Sensor at Cryogenic Temperature", IEEE Electron Device letters, Paper accepted.

2) A. Abderrahmane, H. Takahashi, T. Tashiro, P. J. Ko, H.Okada, S. Sato, T. Ohshima and A. Sandhu, "Effect of Annealing on Proton Irradiated AlGaN/GaN based micro-Hall sensors", AIP Conference Proceedings **1585**, 123 (2014).

3) A. Abderrahmane, T. Tashiro, H. Takahashi, P. J. Ko, H.Okada, S. Sato, T. Ohshima and A. Sandhu, "Partial recovery of the magnetoelectrical properties of AlGaN/GaN-based micro-Hall sensors irradiated with protons", Applied Physics Letters **104**, 023508 (2014).

4) A. Abderrahmane, S. Koide, H. Okada, H. Takahashi, S. Sato, T. Ohshima, and A. Sandhu; "Effect of proton irradiation on AlGaN/GaN micro-Hall sensors"; Applied Physics Letters **102**, 193510 (2013).

5) A. Abderrahmane, S. Koide, T. Tahara, S. Sato, T. Ohshima, H. Okada and A. Sandhu; "Effect of Proton Irradiation on 2DEG in AlGaN/GaN Heterostructures"; Journal of Physics: Conference Series 433 (2013) 012011.

6) A. Abderrahmane, S. Koide, S. Sato, T. Ohshima, A. Sandhu and H.Okada; "Robust Hall Effect Magnetic Field Sensors for Operation at High Temperatures and in Harsh Radiation Environments"; IEEE Transactions on Magnetics, vol. 48, no. 11, November 2012.

7) H.Okada, A. Abderrahmane, S. Koide, H. Takahashi, S. Sato, T. Ohshima and A. Sandhu; "Effects of Proton Irradiation on the Magnetoelectric Properties of 2DEG AlGaN/GaN Micro-Hall Sensors"; Journal of Physics: Conference Series 352 (2012) 012010

8) S. Koide, H. Takahashi, A. Abderrahmane, I. Shibasaki and A. Sandhu; "High Temperature Hall sensors using AlGaN/GaN HEMT Structures"; Journal of Physics: Conference Series 352 (2012) 012009.

International conferences

1) A. Abderrahmane, H. Takahashi, T. Tashiro, P. J. Ko, H. Okada, S. Sato, T. Ohshima and A. Sandhu; "Effect of Annealing on Proton Irradiated AlGaN/GaN based micro-Hall sensors"; The Asia-Pacific Interdisciplinary Research And Global Outlook 2013 (**IRAGO 2013**); 24-25 Oct. 2013; Tahara-City, Aichi, Japan.

2) A. Abderrahmane and A. Sandhu; "High temperature Scanning Hall Probe Microscopy and Temperature Sensors"; **EIIRIS プロジェクト研究成果報告会**「-機能集積化デバイスの開発研究の現状と展開-」; Toyohashi University of technology.

3) A. Abderrahmane, S. Koide, H. Takahashi, T. Tahara, H. Okada, S. Sato, T. Ohshima, and A. Sandhu; "Effect of Proton Irradiation on Quantum Hall Effect in AlGaN/GaN 2DEG Heterostructures "; The Asia-Pacific Interdisciplinary Research Conference 2012 (**AP-IRC 2012**); 15-16 Nov. 2012; Tahara-City, Aichi, Japan.

4) A. Abderrahmane, H. Okada, S. Koide, S. Sato, T. Ohshima and A. Sandhu; "Robust Hall effect magnetic field sensors for operation at high temperatures and in harsh radiation environments"; IEEE International Magnetics Conference 2011 **(INTERMAG 2012)**; 7-11 May. 2012; Vancouver.

5) A. Abderrahmane, S. Koide, H. Takahashi, H. Okada, S. Sato, T. Ohshima, and A. Sandhu; "Proton Irradiation of 2-DEG AlGaN/GaN Micro-Hall Sensors"; The Asia-Pacific Interdisciplinary Research Conference 2011 (**AP-IRC 2011**); 17-18 Nov. 2011; Toyohashi university of technology.